Flat bands, snake states and superconductivity in graphene monolayers

Laura Ann Cohnitz

aus Neuss

aus dem Institut für Theoretische Physik IV
der Heinrich-Heine-Universität Düsseldorf

Gedruckt mit der Genehmigung der
Mathematisch-Naturwissenschaftlichen Fakultät der
Heinrich-Heine-Universität Düsseldorf

Berichterstatter:

1. Prof. Dr. Reinhold Egger

2. Prof. Dr. Dr. Carsten Müller

Tag der mündlichen Prüfung: 01.12.2017

„I*t's a dangerous business,*
Frodo, going out your door.
You step onto the road,
and if you don't keep your feet,
there's no knowing
where you might be swept off to."

J.R.R. Tolkien

Abstract

A theoretical analysis of the effects caused in graphene monolayers as a result of different external influences is presented. Due to the special dispersion relation around the Dirac points in graphene where the electrons can be described in terms of massless ultrarelativistic particles, this material offers the opportunity to investigate entirely new phenomena that may ultimately lead to the creation of new technologies or a deeper understanding of elementary physical processes for example in quantum electrodynamics.

Recent experimental progress in the fabrication of ultraclean graphene samples allows for the consideration of the ballistic regime where disorder effects can be neglected. Therefore, this is a very active field of research enabling transport experiments, or for example the investigation of proximity effects caused by nearby superconductors.

Within the context of this thesis, three settings are considered. In the first, an inhomogeneous magnetic field profile is used to create a waveguide. Therefore, the electrons either exhibit circular motions, also known as Landau orbitals in regions of constant magnetic field or snake motions in the vicinity of the field sign change. Furthermore, the setup is interesting since it creates a zero-energy flat band caused by the Landau levels and it will be demonstrated that it is possible to evoke a dispersion only by taking into account intraband interactions, and even to transform this insulator to a conductor by considering virtual transitions to higher energy bands. Hence, a method is obtained to probe for the existence of interactions by merely performing a transport experiment. The resulting conductor, which is interaction-driven and whose peculiar dependence on the filling factor only occurs for the zero-mode, is not captured by the conventional description and predicted to also be realizable in other settings.

Whereas in semiconducting materials usually used to create *p-n* junctions, doping and other technical steps are required, the situation for graphene is much simpler. As a consequence of the previously mentioned linear dispersion relation, the application of gates suffices to fabricate a highly tunable uni- or bipolar interface. Herein, snaking behaviour does not originate from a

change in the magnetic field but from the Klein tunnelling paradox allowing an electron to be transmitted as a hole through a potential barrier. In this second part, the two geometries of a straight and a circular symmetric *p-n* junction subject to a magnetic field perpendicular to the graphene layer are regarded. The exact solution of the quantum-mechanical eigenproblem is evinced and various results such as the existence of a chiral interface state, which travels in a combined snaking-skipping motion, are postulated.

For the third setup, the graphene monolayer is contacted with another fascinating material with unusual properties, videlicet a superconductor, which reveals a vanishing resistance below a certain critical temperature. The proximity of this object causes the presence of another parameter, in particular the superconducting gap, raising off-diagonal terms in the Bogoliubov-de Gennes Hamiltonian. In this setting, it is especially intriguing to consider the simultaneous influence of a magnetic field, which was rendered possible in the frame of certain parameters by recent findings in this particular field of research. At the Dirac point, the astonishing result of unaltered relativistic Landau levels is obtained while the observables exhibit a pronounced dependence on the gap since also the eigenstates are subject to this parameter. Furthermore, an edge, as well as a finite and a linear potential are added to the model evoking dispersion, edge and snake states.

Zusammenfassung

Präsentiert wird die theoretische Betrachtung der Effekte, die in Graphenmonolagen als Folge verschiedener äußerer Einflüsse verursacht werden. Wegen der besonderen Dispersionsrelation am Diracpunkt in Graphen, an dem die Eletronen als masselose ultrarelativistische Teilchen beschrieben werden können, bietet dieses Material die Möglichkeit, vollkommen neue Phänomene zu untersuchen, die auf lange Sicht zur Herstellung neuer Technologien oder dem tieferen Verständnis elementarer physikalischer Prozesse beispielsweise in der Quantenelektrodynamik führen kann.

Kürzlich erfolgter experimenteller Fortschritt in der Herstellung besonders reiner Graphenproben macht die Betrachtung des ballistischen Regimes möglich, in dem Defekte vernachlässigt werden können. Daher stellt dies ein äußerst aktives wissenschaftliches Feld dar, das die Möglichkeit für Transportexperimente oder beispielsweise die Untersuchung der Erzeugung von supraleitenden Effekten hervorgerufen durch die Nähe eines Supraleiters bietet.

Im Rahmen dieser Arbeit wurden drei verschiedene Aufbauten betrachtet. Im ersten wird ein inhomogenes Magnetfeld benutzt, um einen Wellenleiter zu erschaffen. Als Konsequenz vollführen die Elektronen entweder Kreisbahnen (sogenannte Landauorbits) in den Bereichen mit konstantem Magnetfeld oder Schlangenbewegungen in der Nähe des Vorzeichenwechsels des Feldes. Weiterhin ist diese Situation interessant, da im Spektrum ein flaches Band bei Energie Null entsteht, das durch die Landauniveaus verursacht wird. Zudem wird demonstriert, dass es möglich ist, eine Dispersion hervorzurufen, indem man Wechselwirkungen innerhalb des Bandes in Betracht zieht, und diesen bisherigen Isolator sogar in einen Leiter zu verwandeln, wenn auch virtuelle Übergänge zu höherenergetischen Bändern berücksichtigt werden. Infolgedessen liefert dies eine Methode, um die Existenz von Wechselwirkungen ausschließlich durch Durchführung eines Transportexperiments zu überprüfen. Der resultierende Leiter, der durch Wechselwirkungen getrieben ist und dessen erstaunliche Abhängigkeit vom Füllfaktor nur für die Nullmode auftritt, kann nicht mithilfe des üblichen Formalismus beschrieben werden. Dennoch ist anzunehmen,

dass man diesen Zustand auch in anderen Aufbauten realisieren kann.

Während bei halbleitenden Materialien, die üblicherweise zur Herstellung von p-n-Übergängen benutzt werden, Dotierungen und andere technische Schritte von Nöten sind, ist die Lage für Graphen deutlich einfacher. Infolge der bereits eingangs genannten linearen Dispersionsrelation, ist es ausreichend, Elektroden anzubringen, um eine im äußersten Maße einstellbare uni- oder bipolare Grenzfläche zu erzeugen. In diesem Fall tritt ebenfalls eine schlangenartige Bewegung auf, die jedoch in diesem Fall nicht von einem Wechsel des Magnetfeldes herrührt, sondern durch das Klein-Tunnel-Paradoxon hervorgerufen wird, das es einem Elektron gestattet, als Loch durch eine Potentialbarriere zu transmittieren. In diesem zweiten Teil werden die beiden Geometrien eines geraden, sowie eines radialsymmetrischen p-n-Übergangs unter dem Einfluss eines senkrecht zur Oberfläche stehenden magnetischen Feldes betrachtet. Die exakte Lösung des quantenmechanischen Eigenproblems wird aufgezeigt und verschiedene Ergebnisse, unter anderem die Existenz eines chiralen Grenzflächenzustandes, der eine kombinierte schlängelnde und springende Bewegung vollführt, werden postuliert.

Für den dritten Aufbau wird die Graphen-Monolage mit einem weiteren faszinierenden Material mit außergewöhnlichen Eigenschaften zusammengebracht, nämlich einem Supraleiter, dessen Widerstand unter einer bestimmten kritischen Temperatur verschwindet. Die Nähe dieses Objekts verursacht die Präsenz eines zusätzlichen Parameters, der supraleitenden Lücke, die zu nicht-diagonalen Termen im Bogoliubov-de Gennes-Hamiltonoperator führt. Hier ist es von besonderem Interesse, die gleichzeitige Einwirkung eines Magnetfeldes im Rahmen bestimmter Parameter zu betrachten, was durch neuerliche Befunde in diesem Forschungsfeld ermöglicht wurde. Am Diracpunkt wird das unintuitive Ergebnis unbeeinflusster relativistischer Landauniveaus erzielt, wohingegen andere Observablen durchaus von der Lücke abhängen, da auch die Eigenzustände von diesem Parameter verändert werden. Außerdem werden nacheinander eine die unendlich ausgedehnte Graphenlage begrenzende Kante, sowie ein konstantes, endliches und ein lineares Potential hinzugefügt, die zu Dispersion, Rand- und Schlangenzuständen führen.

CONTENTS

x

1

INTRODUCTION

$\mathcal{R}$ight from the moment when graphene was discovered in 2004, it presented a rich topic of research both experimentally and theoretically due to its exceptional properties and carried the hopes to render the establishment of new technologies as well as the realization of proofs for basic physical predictions for Dirac fermions possible. Thus, graphene can be considered as a two-dimensional laboratory to verify the predictions of quantum electrodynamics. For example, a direct test of the Klein paradox on the basis of elementary particles succeeded only nearly 80 years after the prediction and could merely be accomplished as a result of the discovery of graphene [1, 2].

When studying the physics of the two-dimensional monolayers of graphene, especially the low-energy regime around the Dirac point where two-dimensional massless Dirac fermions accurately describe the underlying electronic properties, is interesting [3–10]. As a result of recent experimental efforts, the disorder-free ballistic transport regime classified by comparatively long mean free paths has become accessible due to the fabrication of ultraclean samples that can either be setup as suspended [8] or encapsulated graphene layers in boron nitride crystals [11]. These developments can also be considered as a foundation and motivation to investigate most of the settings treated in this work.

In chapter 3, a magnetic waveguide caused by an inhomogeneous magnetic field profile applied to a clean graphene sheet leads to a zero-energy Landau-like flat band in the single-particle dispersion. Other electronic systems exhibiting flat bands have been studied intensively [12–14], which are reported to arise, for example, in succession of interference effects on geometrically frustrated lattices. When the Fermi level, however, lies inside this flat band, insulating behaviour is anticipated for neglected interactions, resulting in a vanishing conductance. Interactions, on the other hand, can provoke highly non-trivial effects in different materials described by different lattice models with flat bands [15–18], for fermions interacting on a short range on lattices with unit cells that are geometrically frustrated [19–24], and in so-called diamond chains [19, 20], as well as for interacting bosonic [25, 26] and cold-atom systems [27]. Albeit, the magnetic

graphene waveguide considered here exhibits an extraordinary feature: Usually, the presence of electron-electron interactions causes the suppression of conductance whereas in this case the existence of Coulomb interactions can transform the primarily insulating system into a conductor with exceptional properties that cannot be captured by the standard description for interacting one-dimensional conductors, namely the Tomonaga-Luttinger liquid theory.

Chapter 4 is concerned with different geometries of *p-n* junctions in graphene, in particular a straight and a circular junction, under the influence of a perpendicular magnetic field. As in the previously discussed system, there are Landau levels in the bulk and also snake states although in contrast to above they are not caused by the sign change of a magnetic field but as a result of the interface between regions with positive and negative potential in combination with the Klein tunnelling phenomenon. Experimentally, *p-n* junctions are easily fabricated in graphene just by attaching suitable electrostatic gates and have attracted plenty of attention [28–46] realizing the theoretical and experimental study of various physical regimes and different geometries.

Chapter 5, contains the study what happens if a proximity-induced superconducting pairing gap is induced in the graphene layer owing to a s-wave superconductor placed in the vicinity, and the simultaneous impacts of this parameter and a magnetic field are explored. The possibility of observing both effects at the same time despite phenomena such as the Meissner effect, has been established due to recent experimental studies on Josephson transport in graphene flakes in the ballistic regime that were contacted with superconductors [47–57] where it was proven that both effects are able to coexist even if the magnetic field is high enough to generate Landau quantization [52–54]. In this setting, the counter-intuitive prediction of standard Landau levels is found at the Dirac point, and the behaviour in the presence of a constant potential as well as the discovery of snake states in the presence of a linear potential evoked by the application of an electric field is described.

To summarize, after illustrating the necessary basics in chapter 2, the theoretical considerations of a graphene sheet exposed to diverse influences, namely an inhomogeneous magnetic field (chapter 3), a homogeneous magnetic field in combination with a step-like potential (chapter 4) and, finally, proximity-induced superconductivity together with a constant magnetic field and different potentials (chapter 5), are presented, before everything will be briefly resumed in chapter 6. Thus, interesting effects such as flat bands, snake states, as well as superconductivity-induced pairing of electrons and holes, and also their consequences on physical observables have been studied.

Whenever appropriate, these results are contrasted with those obtained from the equivalent setting of a two-dimensional electron gas, where another two-dimensional material with different underlying physics is considered, as the electrons here are described as Schrödinger fermions.

The settings were designed and the observables chosen in a manner that allows for experimentalists to test the predictions and thus will hopefully advance research in this area of interest.

2

FUNDAMENTAL PRINCIPLES

This chapter provides the general basis necessary to understand the different calculations and interpretations explained in the chapters 3-5, beginning from the special material graphene which is the underlying substance in all the setups and whose interesting properties are exploited theoretically, as well as the electron gas, which will be utilized to contrast these findings with those for a material with different physics. In the following section the general concept of Landau levels and hence the Quantum Hall Effect are discussed for both these systems. Furthermore, the concept of waveguides, which can be realised in graphene using an inhomogeneous magnetic field profile leading to the so-called snake states (as shown also in chapter 3), is treated. Besides, an overview regarding the state of research on *p-n* junctions will be given, presenting the foundation for the results shown in chapter 4. Although already in the context of the dimensionally reduced electron gas as well as the waveguide one-dimensional systems were discussed, it is insightful to also mention the Luttinger liquid and emphasise the difference with respect to the common Fermi liquid. Moreover, the convenient tool of the mean field theory is presented as well as the special formulations which can be applied to the cases of an electron gas with Coulomb interactions and, secondly, superconductors which prove to be materials with the most interesting properties. The consequences of combining a superconducting material and a graphene flake are discussed in chapter 5. Finally, different approximations to actually evaluate the expressions for the desired physical quantities are portrayed, such as the concepts of perturbation and linear response theory, which can be applied in the situation with only a small time-dependent perturbation causing the system to deviate from its constant state, and the Keldysh Green's function technique enabling to further elaborate the results thus obtained.

2.1 Graphene

Graphene is a peculiar material which has attracted a lot of attention since its discovery in 2004 by Andre Geim and Konstantin Novoselov who received the Nobel prize for their work in 2010.

2.1.1 Structure and general properties

Graphite possesses strong covalent bonds within the plane and only comparatively smaller van der Vaals bonds between the different layers, and therefore allow for the separation of monolayers. Such a monolayer is denoted as graphene, and it has a hexagonal symmetry due to the structure of the sp^2-hybridised carbon atoms. These σ-bonds are formed by the $2s$-, $2p_x$- and $2p_y$-orbitals which are positioned within the plane under an angle of $120°$ leading to the common denomination of this Bravais lattice as honeycomb lattice whereas the out-of-plane p_z-orbitals build the strong covalent π-bonds. Nevertheless, it is usually described using a triangular lattice with two atoms as a basis each forming a trigonal sublattice, labelled as A and B. The lattice vectors connecting the different atoms of one sublattice are given by

$$\mathbf{a}_1 = \frac{a}{2}(3, \sqrt{3})$$
$$\mathbf{a}_2 = \frac{a}{2}(3, -\sqrt{3})$$

$$(2.1)$$

with the bonding length $a \approx 1,42\text{Å}$, and these are also those vectors along which the unit cell (shown in figure 2.1) has to be translated in order to fill the entire space without gaps and overlap.
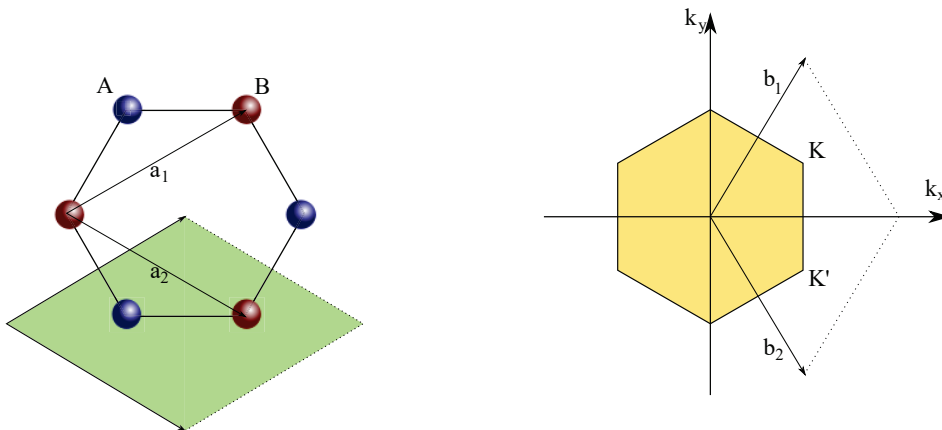
Figure 2.1: Left: Schematic drawing of the lattice structure with the two sublattices A and B, denoted with blue and red, respectively. The unit cell is shown in green. Right: Reciprocal lattice with lattice vectors and first Brillouin zone in yellow. Loosely based on [6].

The energy $t \approx 2.8\,\text{eV}$ required for jumping from one atom to the next, which equals switching the sublattice, is much higher than the one necessary for going from one atom to the next nearest on the same sublattice, which is approximated to be within the range $0.02\,t \le t' \le 0.2\,t$ [6]. When regarding instead the k-space, one finds that the reciprocal lattice has again the structure of a honeycomb lattice – only this time it is rotated by an angle of $90°$ with respect to the original real space lattice and its side lengths are different. The points at the six corners are called Dirac- or K-points and the two inequivalent ones are given by

$$
\begin{aligned}
\mathbf{K} &= \left(\frac{2\pi}{3a}, \frac{2\pi}{3\sqrt{3}a}\right) \\
\mathbf{K}' &= \left(\frac{2\pi}{3a}, -\frac{2\pi}{3\sqrt{3}a}\right).
\end{aligned}
\tag{2.2}
$$

These points are important for most calculations and also have special properties as described later. The fact that an electron can belong to either of these points is denoted as Valley degree of freedom or pseudo-spin. The reciprocal lattice vectors

$$
\begin{aligned}
\mathbf{b}_1 &= \frac{2\pi}{3a}(1, \sqrt{3}) \\
\mathbf{b}_2 &= \frac{2\pi}{3a}(1, -\sqrt{3})
\end{aligned}
\tag{2.3}
$$

span the first Brillouin zone, which is the Wigner-Seitz cell of the reciprocal lattice.

Although graphene forms ripples due to stability reasons, it can be thought of as a two-dimensional material since it only has the thickness of one atom but can be much larger in the other two directions. As such, it offers a variety of special and useful properties such as flexibility and chemical reactivity since it is thin and thus has a large surface, and its value of the tensile strength is extremely high.

2.1.2 DIRAC FERMIONS AND SPECIAL DISPERSION RELATION

Furthermore, a tight-binding Hamiltonian including nearest- as well as next nearest neighbour hopping of the electrons can be written as [6]

$$
\begin{aligned}
H &= -t \sum_{\langle i,j \rangle, \sigma} \left(a_{\sigma,i}^{\dagger} b_{\sigma,j} + h.c.\right) \\
&\quad - t' \sum_{\langle\langle i,j \rangle\rangle, \sigma} \left(a_{\sigma,i}^{\dagger} a_{\sigma,j} + b_{\sigma,i}^{\dagger} b_{\sigma,j} + h.c.\right)
\end{aligned}
\tag{2.4}
$$

where t (t') is the energy required for hopping between neighbouring atoms (next nearest atoms) as shown before, i.e. between different sublattices (within the same sublattice) A and B. This is denoted by the different letters for the second quantized ladder operators $a_{\sigma,i}^{(\dagger)}, b_{\sigma,i}^{(\dagger)}$ which create
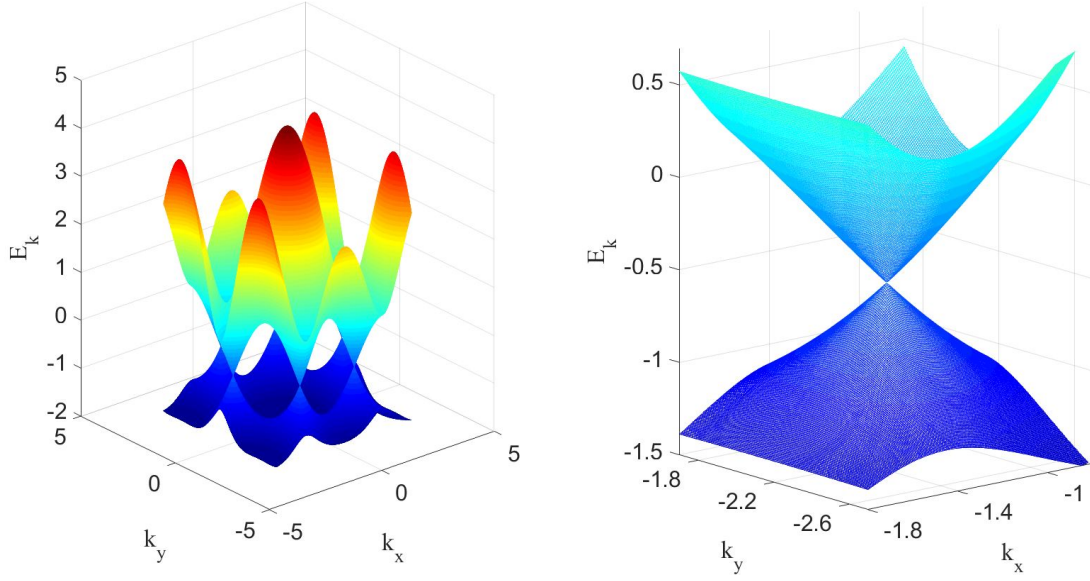
Figure 2.2: Left: Dispersion relation obtained from equation (2.5) showing the sixfold symmetry of the first Brillouin zone. Right: Zoom close to the Dirac point.

or annihilate an electron with spin $\sigma = \uparrow, \downarrow$ on the ith site of the respective sublattice. From this, the dispersion relation can be derived and reads [6]

$$E_\pm(\mathbf{k}) = \pm t\sqrt{3 + f(\mathbf{k})} - t'f(\mathbf{k}) \tag{2.5}$$

with the function

$$f(\mathbf{k}) = 2\cos\left(\sqrt{3}k_y a\right) + 4\cos\left(\frac{\sqrt{3}}{2}k_y a\right)\cos\left(\frac{3}{2}k_x a\right) \tag{2.6}$$

where a is the lattice constant describing the distance between closest atoms. The positive sign refers to the conductance band while the negative sign applies to the valence band. Obviously, for a finite t', the electron-hole symmetry is broken, leading to asymmetric energy bands which are shown in the left panel of figure 2.2. As one can see, the two bands only touch in very distinctive points in the spectrum which form a hexagon in the reciprocal space: These are the so-called Dirac or K and K' points marking the corners of the first Brillouin zone. Expanding the energy dispersion around these points writing the wave vector as $\mathbf{k} = \mathbf{K} + \mathbf{q}$ with $|\mathbf{q}| \ll |\mathbf{K}|$, one obtains an energy which depends linearly on $\mathbf{q}$ up to the first order [58]

$$E_\pm(\mathbf{q}) \approx \pm v_F|\mathbf{q}| + \mathcal{O}\left[\left(\frac{q}{K}\right)^2\right] \tag{2.7}$$

with the Fermi velocity $v_F = 3ta/2 \approx 10^6$ m/s $\approx c/300$. In stark contrast to the standard case of free electrons exhibiting a quadratic dispersion, the Fermi velocity does not depend on the energy or momentum and the linear dispersion, which can also be seen directly when zooming in on the

Dirac points of the spectrum as depicted in the right panel of figure 2.2, is obtained. It resembles the light cone for photons or generally speaking the energy dispersion of ultrarelativistic particles whose motion is described by the Dirac equation instead of the Schrödinger equation. Thus, the electrons in graphene can be described as massless Dirac fermions obeying the 2D Dirac equation [6]

$$-iv_F\sigma \cdot \nabla\psi(\mathbf{r}) = E\psi(\mathbf{r}). \tag{2.8}$$

2.1.3 Klein tunnelling

Originally the Klein paradox was observed by Oskar Klein when he applied the Dirac equation to the problem of an electron impinging on a potential barrier. The nonrelativistic answer in quantum mechanics is that the particle tunnels into the barrier with exponentially strong damping. Klein, on the other hand found for his case that for a high potential barrier the electron is transmitted with probability one and judged that already for a barrier of a height V_0 which is a multiple of the rest energy E of the electron, it should be nearly transparent [1]. This effect is not only highly unintuitive and contradicts the non-relativistic observation that the damping of the transmission increases exponentially with the potential height, but for a long time it was also not possible to put this prediction to a test.

In [2] the situation was adapted for graphene with the result of perfect tunnelling of the electrons hitting a suitably high square shaped potential barrier with perpendicular incidence. In general, a formula for the transmission probability was found depending strongly on the angle of incidence ϕ, which for this limit of a high barrier ($V_0 \gg E = E_F$) reads

$$T(\phi) = \frac{\cos^2(\phi)}{1 - \cos^2(q_x D)\sin^2(\phi)} \tag{2.9}$$

with D being the width of the potential step and $q_x = \sqrt{(E - V_0)^2/\hbar^2 v_F^2 - k_y^2}$. This result can be interpreted considering the linear dispersion at the Dirac points assuming the Fermi energy E_F lies in the conduction band outside of the barrier such that electrons are the charge carriers. In the region of the barrier however, the Dirac cone is lifted due to the finite potential and thus the Fermi energy is found inside the valence band, compare figure 2.3. Electrons with energy E and holes with energy $-E$ propagating in the direction opposite to that of the electrons are related due to symmetry and originate from the same branch in the electronic spectrum with a pseudospin σ pointing in the same direction. Hence, the electron penetrating the barrier is transmitted in the potential step as a hole with opposite momentum and the same pseudospin and hence the opposite chirality since this quantity defines whether the pseudospin and the direction of motion are parallel or anti-parallel. In this context the phenomenon can be explained making use of the conservation of the pseudospin, whose flip would need the presence of a short range potential, meaning that an electron moving in one direction can only be scattered into an electron moving in the same or a hole moving in the opposite direction [2]. The position of the Fermi
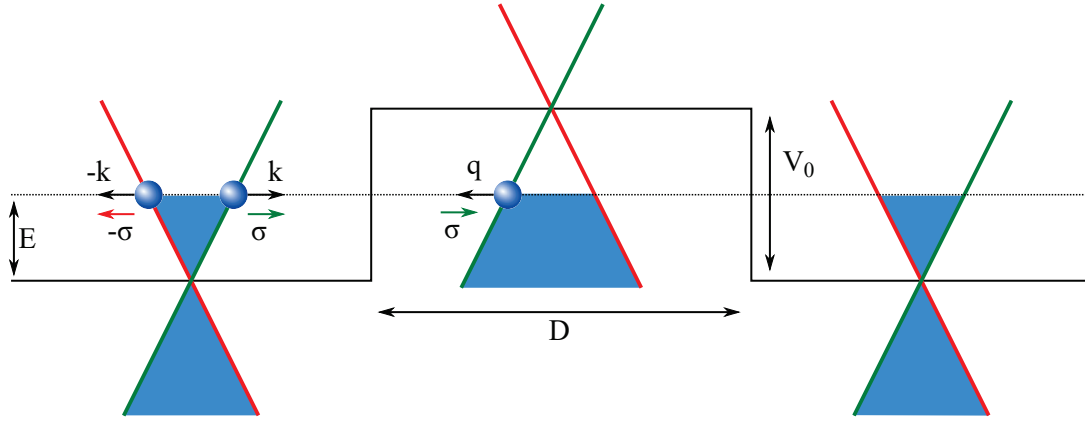
Figure 2.3: Schematic illustration of the Klein tunnelling. Red and green label the different pseudospin branches. The height of the Dirac cone is determined by the potential while the filling is given by the energy E. Freely adapted from [2].

energy furthermore eliminates the first possibility. After the potential step, the hole is again transmitted as an electron.

This behaviour has not only been predicted but also been verified experimentally in the context of *p-n* junctions [59].

A different aspect is that this effect couples electrons and holes, similarly to the Andreev reflection at interfaces with superconductors where electrons can be reflected as holes while a Cooper pair is transmitted to fulfil all conservation rules. In [60] it was shown that Klein tunnelling through *p-n* interfaces and Andreev reflection at a superconductor can indeed be mapped, making predictions, such as pseudosuperconducting behaviour, for other systems with a band structure corresponding to that of graphene.

2.2 ELECTRON GAS

Historically the model of the electron gas was an important means on the route to developing quantum field theory but also nowadays this picture finds ample usage when there is the need to find an easily understandable model of complex solids from insulators to metals.

Considering an atom in a metal, it is advisable for this model to distinguish between three parts: the positively charged nucleus (not caring about its composition), the electrons close to it, which are strongly bound, and the valence electrons furthest away from the ion, which have the possibility to disengage from the respective nucleus and form an electron gas delocalized among the different ions. This picture of a periodic lattice made of ions and the free electron gas which surrounds and also stabilizes it due to the electric force, is the ground state of the system for zero temperature. From this system, several excitations can be obtained such as phonons, plasmons, magnons or simply electron-hole excitations [61].

2.2.1 GENERAL MODEL: NON-INTERACTING ELECTRON GAS

For a lot of applications, it is sufficient to study the simplified model of an electron gas neglecting interactions and there are two models which can be deployed.

LATTICE MODEL

In the phenomenological lattice model, a periodic lattice structure is taken as basis and the ions are expected to only vibrate around their strict positions due to the energy they get from a finite temperature while an electric force pulls them back to their original spot. The general Hamiltonian for this system is given as [61]

$$H = (E_{latt} + H_{ph}) + (T_{el} + V_{el-el}) + (V_{el-latt} + V_{el-ph}) \tag{2.10}$$

where E_{latt} is the energy of the lattice and $V_{el-latt}$ is the related potential built from the kinetic energy of the ions and the potential energies between ions and electrons and ions among themselves. The quantized vibrations are summarized in a phonon field whose non-interacting part is given by H_{ph} and the electrons in the system have a kinetic energy T_{el}, interact with each other according to V_{el-el} and with the phonons as V_{el-ph} due to the electrical potential arising from the vibrating ion.

Switching to zero temperature all vibrations (except for the quantum mechanical zero point motion) can be neglected and the lattice becomes static. The Hamiltonian of this so-called Bloch theory is given as

$$H_{Bloch} = T_{el} + V_{el-latt}(\mathbf{r}). \tag{2.11}$$

The potential possesses the periodicity of the lattice, namely $V_{el-latt}(\mathbf{r} + \mathbf{R}) = V_{el-latt}(\mathbf{r})$ when $\mathbf{R}$ is an arbitrary lattice vector. In order to solve this problem, it is convenient to transform from real to k-space and thereby use that the Fourier transform of a periodic function of the form $V(\mathbf{r} + \mathbf{R}) = V(\mathbf{r})$ follows as

$$V(\mathbf{r}) = \sum_{\mathbf{G} \in RL} V_{\mathbf{G}} e^{i\mathbf{G} \cdot \mathbf{r}} \tag{2.12}$$

with the reciprocal lattice (RL) vector $\mathbf{G}$. Solving the Schrödinger equation $H_{Bloch}\psi = E\psi$ for this problem yields [61] eigenfunctions with the identical periodicity compared to the underlying lattice structure

$$\psi_{n,\mathbf{k},\sigma}(\mathbf{r}) = u_{n,\mathbf{k}}(\mathbf{r}) e^{i\mathbf{k} \cdot \mathbf{r}} \chi_\sigma, \tag{2.13}$$

which is hidden in the lattice periodical function $u_{n,\mathbf{k}}(\mathbf{r} + \mathbf{R}) = u_{n,\mathbf{k}}(\mathbf{r})$. Here, the spin part is χ_σ whereas the spatial part is expressed via the exponential function $e^{i\mathbf{k} \cdot \mathbf{r}}$, n is the respective band index and the wave vector $\mathbf{k}$ is chosen to be within the first Brillouin zone since any other

vector would solely yield a copy of the same set of equations. Thus, it is obvious that mere plane waves simply modified via a periodic function yield solutions.

Jellium model
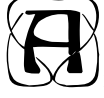
Another possibility to model the situation of an ion lattice with a free electron gas is offered by the Jellium model. Instead of working with a strict lattice as before, the Jellium model starts from a smeared out homogeneous positively charged background, the so-called ion jellium, which is expressed in terms of a static density. Thus, the periodic lattice potential is transformed into a constant one called V_{el-jel}, see figure 2.4.

Ignoring interactions among the electrons and hence looking only at the homogeneous part, the Hamiltonian of the Jellium model simply consists of the kinetic energy of the electrons

$$H_{jel} = T_{el}. \tag{2.14}$$

Solving the Schrödinger equation

$$H_{jel}\psi_{\mathbf{k},\sigma} = \frac{\hbar^2 k^2}{2m}\psi_{\mathbf{k},\sigma} \tag{2.15}$$

for this problem in a box with volume V and periodic boundary conditions leads to plane wave solutions

$$\psi_{\mathbf{k},\sigma}(\mathbf{r}) = \frac{1}{\sqrt{V}}e^{i\mathbf{k}\cdot\mathbf{r}}\chi_\sigma. \tag{2.16}$$

From this, the Hamiltonian in second quantized form can be written as [61]

$$H_{jel} = \sum_{\mathbf{k},\sigma}\frac{\hbar^2 k^2}{2m}c^\dagger_{\mathbf{k},\sigma}c_{\mathbf{k},\sigma} \tag{2.17}$$

using annihilation (creation) operators $c^{(\dagger)}_{\mathbf{k},\sigma}$.
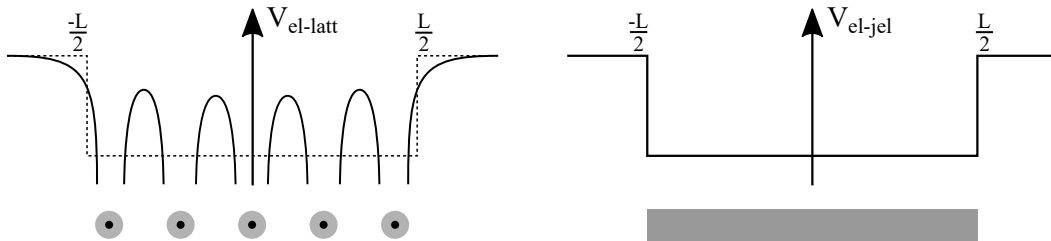
Figure 2.4: Left: Potential originating from the ions as considered in the lattice model. Right: Smeared out step-like potential obtained in the Jellium model picture. Based on [61].

FERMI SEA

$\mathcal{O}$rdering these states representing the wave functions of single particles, expressed in terms of kets as $\psi_{\mathbf{k},\sigma} = |\mathbf{k}, \sigma\rangle$, regarding their energies $\epsilon_{\mathbf{k}} = \hbar^2 k^2/2m$ from small to large and then filling the first N states according to the number N of electrons in the system, leads to the Fermi sea. It is expressed as [61]

$$|FS\rangle = c_{\mathbf{k}_{N/2},\uparrow}^{\dagger} c_{\mathbf{k}_{N/2},\downarrow}^{\dagger} \cdot ... \cdot c_{\mathbf{k}_1,\uparrow}^{\dagger} c_{\mathbf{k}_1,\downarrow}^{\dagger}|0\rangle \tag{2.18}$$

and yields the zero temperature ground state. The Fermi energy is defined as that energy of the highest occupied state and from this quantity also the Fermi wave number k_F, wavelength λ_F, velocity v_F and temperature T_F can be obtained as

$$k_F = \frac{\sqrt{2m\epsilon_F}}{\hbar}, \quad \lambda_F = \frac{2\pi}{k_F}, \quad v_F = \frac{\hbar k_F}{m}, \quad T_F = \frac{E_F}{k_B} \tag{2.19}$$

with the Boltzmann constant k_B. Due to its definition, for a system in the ground state, the states with wave number $|\mathbf{k}| < k_F$ equalling to energies $\epsilon_{\mathbf{k}} < \epsilon_F$ are occupied while all others are empty. Hence, the occupation can be expressed using a step function such as the Heaviside function $\theta(x)$ for zero temperature. When increasing the temperature, however the Fermi-Dirac distribution

$$n_F(\epsilon_{\mathbf{k}}) = \frac{1}{e^{\frac{\epsilon_{\mathbf{k}}-\mu}{k_B T}} + 1} \rightarrow \theta(\mu - \epsilon_{\mathbf{k}}) \quad \text{for} \quad T \rightarrow 0 \tag{2.20}$$

describes the occupation with the chemical potential μ. Much use of these quantities will be made in the various sections of chapters 3-5.

2.2.2 ADDING INTERACTIONS

$\mathcal{W}$hen not only the homogeneous, but also the inhomogeneous part including the interactions among the electrons encoded in the potential V_{el-el} is taken into account on top of the described Jellium model, this can be either done using perturbation theory results (see [61] and 2.9) or exploiting the Hartree Fock method (compare section 2.7.2).

2.2.3 REDUCED DIMENSIONS

$\mathcal{A}$lready in three dimensions, the model of the electron gas is useful to explain the occurrence of materials behaving as different as metals and insulators since the location of the Fermi energy relative to the different energy bands of the specific material defines this property. Nevertheless, also reducing the number of dimensions yields interesting results.

When combining different semiconductors such as gallium-arsenide (GaAs) and gallium-alumin-um-arsenide ($Ga_{1-x}Al_xAs$) which have very similar crystal structures resulting in interfaces of good quality, it is possible to obtain an electron gas reduced to two dimensions [61]. The general trick is that one of the materials (in this case GaAs) has a conduction band at a lower energy than the other. Doping the second material with silicon (Si) thus introduces conduction electrons to the system which tend to flow to the material with the lower energy band until they are held back by the resulting electrostatic potential caused by the Si ions. Thus, when balance is reached, a two-dimensional electron gas (2DEG) is fabricated at the interface and no longer just a theoretical construct. This also modifies the wave function from equation 2.16 to [61]

$$\psi_{k_x,k_y,n,\sigma}(\mathbf{r}) = \frac{1}{\sqrt{A}} e^{ik_x x} e^{ik_y y} \zeta_n(z) \chi_\sigma \qquad (2.21)$$

when A is the plane and the nth eigenfunction belonging to eigenenergy ϵ_n is expressed as $\zeta_n(z)$. Plane waves are kept in x- and y-directions whereas for the z-direction a quantization is found. An interesting and graphene-related example for a one-dimensional electron gas system is a carbon nanotube. It can be envisioned as a sheet of graphene that has been rolled up to form a cylindrical shape with a diameter of about $4\,nm$ and a much larger length. Like graphene, these carbon nanotubes have extraordinary properties such as being very strong and stiff when comparing their tensile strength and elastic modulus to other materials. They can be fabricated single walled or multi-walled and depending on the way the tube is rolled (defined via the edge that ends up at the end of the tube as zigzag, armchair or chiral), they can behave differently regarding their electrical properties, occupying the entire spectrum from being insulating, to semiconducting and metallic. The single particle wave function for this problem becomes one-dimensional and due to the geometrical symmetries it is convenient to switch to cylindrical coordinates (x, r, ϕ) since the π-bonds of the graphene layer bind the electrons to the surface of the nanotube. The result reads

$$\psi_{k_x,n,l,\sigma}(\mathbf{r}) = \frac{1}{\sqrt{L}} e^{ik_x x} R_{n,l}(r) Y_l(\phi) \chi_\sigma \qquad (2.22)$$

[61] with the length L, the polynomial degree of freedom l, the radial wave function $R_{n,l}(r)$ and the angular part given by the spherical harmonics $Y_l(\phi)$. At room temperature there is only one degree of freedom left, in which the electron can move, which is along the axis of the tube chosen in x-direction where also the plane wave remains, yielding almost perfect 1D behaviour. This makes carbon nanotubes interesting not only for experiments but also for testing one-dimensional theories such as the Luttinger liquid model (compare chapter 2.6).

If also the last dimension, in which the particles are free to move, is restricted, for example by adding the appropriate number of gates to a 2DEG, a zero-dimensional so-called artificial atom or quantum dot is created.

However, the 2DEG has often been used to contrast the results obtained in the chapters 3-5 for

graphene with results for a system with the same dimensions but different underlying physics since the electrons behave as Schrödinger or massless Dirac fermions, respectively.

2.3 LANDAU LEVELS AND QUANTUM HALL EFFECT IN 2DEG AND GRAPHENE

Both in the two-dimensional electron gas (2DEG) and graphene, the existence of Landau levels and the Quantum Hall Effect have been predicted and experimentally observed.
When applying a magnetic field perpendicular to the plane in which the 2DEG is situated, it is possible to define two sets of second-quantized bosonic ladder operators $a^{(\dagger)}$ and $b^{(\dagger)}$ which define the eigenstate of a Landau level as

$$|n, m\rangle = \frac{(a^\dagger)^n (b^\dagger)^m}{\sqrt{n!m!}} |0, 0\rangle \qquad (2.23)$$

with $n, m = 0, 1, 2, \dots$ and n being the Landau level index and the eigenvalue to the number operator $\hat{n} = a^\dagger a$ and analogously for $\hat{m} = b^\dagger b$ [62]. From the calculation follows the Hamiltonian

$$H = \hbar\omega_c \left(a^\dagger a + \frac{1}{2} \right), \qquad (2.24)$$

which formally describes a harmonic oscillator, and thus also the eigenenergies

$$E_n = \hbar\omega_c \left(n + \frac{1}{2} \right) \qquad (2.25)$$

depend only on the number n resulting in a high degeneracy since the energy is the same for all different m. This equals the fact that the energy of a Landau level, which can semi-classically be thought of as an electron describing a circular motion within the magnetic field, does not depend on its position in the plane which is encoded in the operators $b^{(\dagger)}$ [62]. The degree of this degeneracy can be expressed for a finite sample of width L_x and length L_y as

$$N_s = \frac{L_x L_y}{2\pi l_B^2} \qquad (2.26)$$

with the magnetic length $l_B = \sqrt{\hbar c / eB}$ yielding a useful length scale of the problem.
Adding leads to the 2DEG and applying a voltage results in a finite conductance since there are edge modes which can carry a charge across the sample. Within the semi-classical picture they can be thought of as skipping orbits consisting of a series of half-circles along the border of the sample leading to a propagating electron as depicted in figure 2.5. In terms of the energy spectrum this happens due to the bending of the Landau levels close to the edges of the Hall sample, which then cross the Fermi energy, forming a situation where the bulk is insulating while there are current carrying modes with opposite direction in the vicinity of the two sample edges. Thus, the
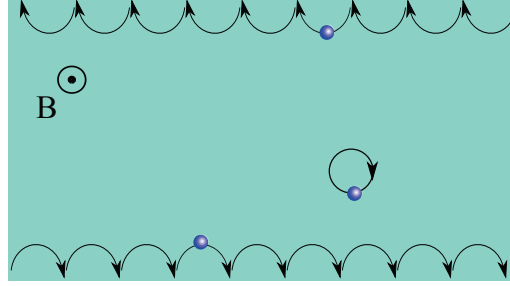
Figure 2.5: Finite-sized sample subject to a constant magnetic field B with Landau orbits in the bulk and skipping orbits along the edges.

counter-propagating modes are spatially well separated, reducing possible back-scattering and leading to a very precise quantized value of the conductance for low temperatures, namely the integer Quantum Hall Effect [61]

$$G^H = 2N\frac{e^2}{h} \tag{2.27}$$

where the factor 2 is included taking into account the spin degeneracy.

For graphene, however, the quantities have different values due to the difference in the behaviour of particles described by the Schrödinger equation as for the 2DEG and those behaving according to the Dirac equation like the massless Dirac fermions in graphene. Hence, the Landau levels in graphene have the energies

$$E_{n,gr} = \text{sgn}(n)\hbar\omega_c\sqrt{2|n|} \tag{2.28}$$

with $n \in \mathbb{Z}$ and also the Quantum Hall Effect shows plateaus at values differing from the ones noted before, namely

$$G_{gr}^H = \frac{4e^2}{h}\left(N + \frac{1}{2}\right), \tag{2.29}$$

making it a half-integer QHE. The reason for the heights of the plateaus is that all levels are four-fold degenerate due to spin and valley (or pseudospin) degeneracy accounting for the factor 4 but the zero-energy Landau level is occupied both by electrons and holes since it marks the symmetry point, and both plateaus at $\pm 1/2 \cdot (4e^2/h)$ belong to these contributions [4]. This half-integer QHE is very peculiar for graphene since even for graphite, a normal integer QHE with level spacing $4e^2/h$ is observed.

2.4 WAVEGUIDES

There are different methods to reduce the number of dimensions, a particle can possibly move in, ranging from conventionally confinements using electronic gates to special techniques only applicable to materials with peculiar properties such as graphene.

2.4.1 Conventional methods

For example, a conventional method is to use a structure like GaAs-GaAlAs, in which the electrons are already confined in a two-dimensional electron gas (compare section 2.2.3 and figure 2.6) a), and then to add gates such as Schottky gates using methods like lithography on top of the structure. Applying a negative voltage to these gates results in an expulsion of the electrons from the respective areas below the gates in the 2DEG-layer and thus an effectively one-dimensional channel is created, in which the electrons are confined. Such a structure is referred to as quantum wire or waveguide.

Furthermore, there are also other forms of quantum wires such as carbon nanotubes (as also described in section 2.2.3).

2.4.2 Methods for graphene

Regarding graphene, further methods exist to manufacture a waveguide. Within this material the electrons are already confined in a two-dimensional space and only one more dimension has to be reduced. The straightforward way would be to cut a nanoribbon using a traditional method like lithography but the resulting features like dispersion relation and band structure are expected to depend strongly on the width of this ribbon and the quality of its border. Furthermore, unavoidable features like disorder would lead to backscattering and other ramifications in such a geometry and hence not allow for the detection of effects such as the conductance quantization which would give evidence for the successful formation of a quantum wire.

Hence, it is desirable to find yet another route to achieve a waveguide without negative side
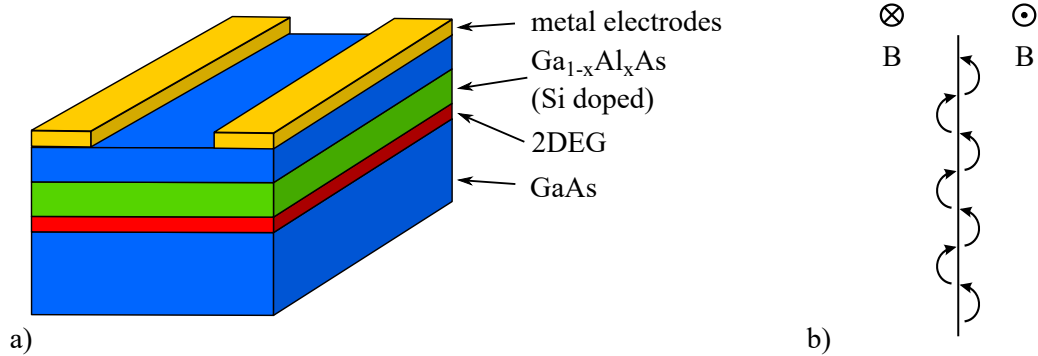
Figure 2.6: Left: Conventional method to obtain a waveguide by building GaAS(blue)-GaAlAs(green) heterostructures leading to the creation of a 2DEG (red) that can be further restricted using metallic gates (yellow), freely adapted from [61]. Right: Schematic drawing of a snake state.

effects. As described in [63], an inhomogeneous magnetic field profile containing an outer region with one direction and a strip in the center with opposite orientation of the magnetic field can be utilized. Whereas in the regions of constant field Landau orbits arise as described in the previous chapter, along the lines where the magnetic field changes direction so-called snake states are evoked which travel unidirectionally along these lines. Similarly to the skipping orbits in the Quantum Hall Effect, these states can be explained in the semi-classical picture: An electron in one of the two regions close to the changing line describes a motion along the circle of a Landau orbit but as soon as it crosses into the region with opposite magnetic field, the direction of rotation is turned and thus it results in a winding motion in the in-plane direction perpendicular to the axis in which the magnetic field profile is inhomogeneous, see figure 2.6 b). Since for a finite width of the central region, these snake states are spatially well separated, no backscattering is expected and for the finite-energy bands thus a quantized conductance can be found [63]. The zero-mode case is treated in chapter 3.

2.5 *P-N* JUNCTIONS IN GRAPHENE IN THEORY AND EXPERIMENT

$\mathcal{P}$-n junctions have widespread use in semi-conductor physics because they allow for the creation of different devices such as diodes, solar cells or transistors. With conventional materials, however, the fabrication process can be involved since it requires the combination and/or doping of materials.

Graphene's special linear dispersion relation, on the other side, provides the possibility to avoid chemical doping (e.g. by adding ions) entirely and create a *p-n* junction solely by applying metallic contacts and voltages. For example by adding a large backgate covering the entire graphene flake and a smaller top gate (compare figure 2.7), one can tune the entire junction continuously. Applying a voltage shifts the height of the Fermi level and thus the filling of levels, which thus becomes tunable in both valence and conductance band, such that all different strengths of *p* (hole-like) and *n* (electron-like) doping can be realized in both regions independently of each other. This makes the controlling of both carrier type and density possible within neighbouring areas of a single atomic layer [28] allowing for *p-n*, *n-n'* and *p-p'* junctions.

Depending on the strength of the magnetic field, different regimes can be observed: For low magnetic field strengths, the electron can cover a longer distance without being much affected by the magnetic deviation. When it hits the junction, it can either be reflected or transmitted as a hole due to the Klein tunnelling phenomenon in graphene (see section 2.1.3). Hence, it will be reflected back and forth either both in its half and across the entire cavity, resulting in Fabry-Pérot oscillations, whose signature can be observed experimentally [45].

Increasing the magnetic field, the regime is reached where the semi-classical picture of snake states can be utilized to explain the obtained features [43]. Unlike in the previous chapter where a magnetic field change lead to the characteristic bending of the trajectory, in the case of a *p-n*
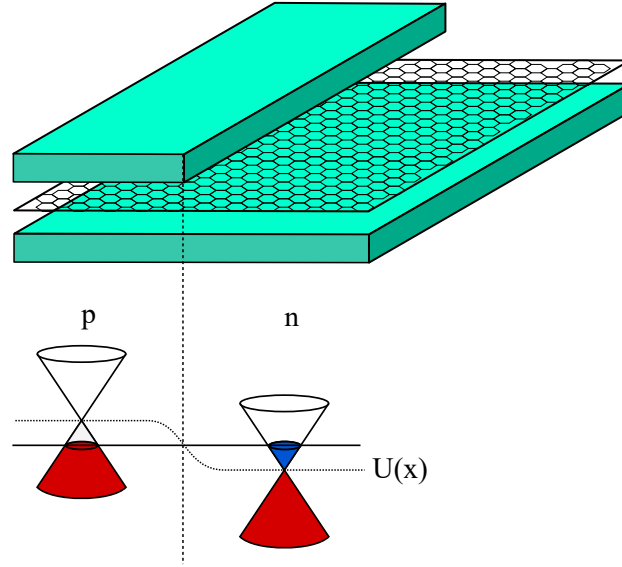
Figure 2.7: Experimental setup of a graphene sheet with top and back gates creating a *p-n* junction and the corresponding band structure at the Dirac point for the two regions caused by the potential $U(x)$. Loosely based on [28, 37].

junction the magnetic field is homogeneous but the charge carrier changes since an electron is transmitted as a hole and vice versa – and even perfectly under normal incidence due to the Klein paradox. As a result of the change of sign of the charge, also the direction of rotation is altered and the snaking motion is triggered. The cyclotron radius of this motion can be tuned either by changing the strength of the overall magnetic field or by altering the carrier density which can be achieved by tuning the relative voltage. When doing so over a wider range, the particle snake trajectory will alternatingly end up in the *p* or *n* part and then continue via skipping orbits to the respective lead. This effect was experimentally seen in an oscillating conductance [45].

In an even stronger magnetic field, the semi-classical picture does not hold and the quantum Hall regime is found, compare figure 2.8. As a result of the number of counter- (for the bipolar or *p-n* junction) or co-propagating (for the unipolar, i.e. *n-n'* or *p-p'* junction) states along the junction, a quantized conductance was observed [28] and explained [64, 65], whose plateaus depend on the carrier densities and thus on the applied voltages as

$$g = \min(|\nu_1|, |\nu_2|)\frac{e^2}{h} = 2\frac{e^2}{h}, 6\frac{e^2}{h}, 10\frac{e^2}{h}, ... \qquad (2.30)$$

Here, $\nu_{1,2}$ are the densities with $|\nu_i|$ being the number of edge modes in the region i and assumed to have the same sign, which means they propagate in the same direction. This means that only a certain number of states crosses the entire system and connects both leads, namely the smaller number of the two, whereas the rest of the modes is coupled only to one reservoir and does not add to the conductance [64].

For different signs of the densities, a multimode edge state is formed along the junction which
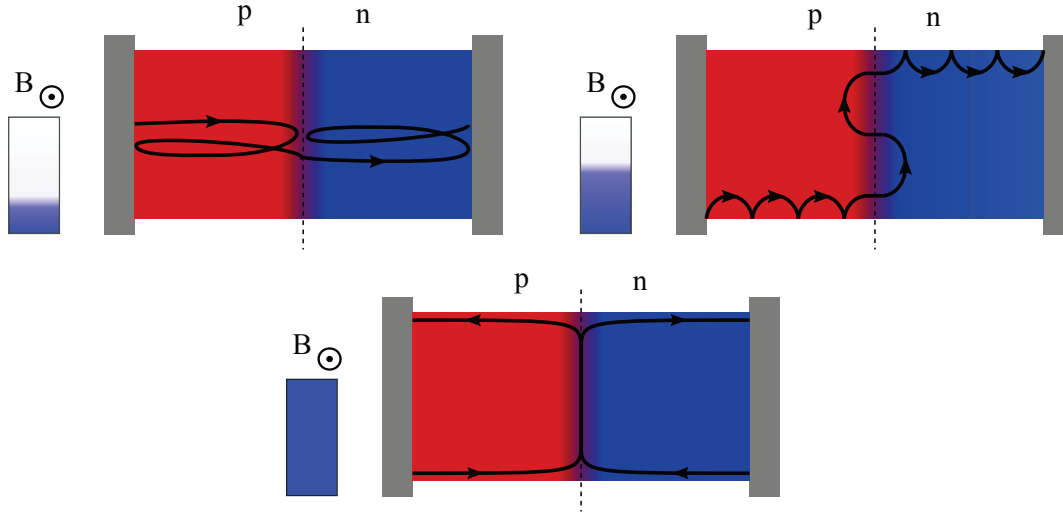
Figure 2.8: Schematic illustration of the evolution of the trajectories of the particles in a graphene *p-n* junction with increasing magnetic field B, from nearly undisturbed curves leading to Fabry-Pérot resonances (top left), to snake and skipping states (top right) and Quantum Hall edge states (bottom), freely adapted from [45].

consists of the $|\nu_1|$ and $|\nu_2|$ states which circulate in opposite direction. If full mixing is assumed to be present, the two-terminal conductance follows as

$$g = \frac{|\nu_1||\nu_2|}{|\nu_1| + |\nu_2|} \frac{e^2}{h} = 1\frac{e^2}{h}, \frac{3}{2}\frac{e^2}{h}, 3\frac{e^2}{h}, \frac{5}{3}\frac{e^2}{h}, ... \tag{2.31}$$

since there are $|\nu_1| + |\nu_2|$ channels in which the respective particle can be emitted and $|\nu_1||\nu_2|$ is the number of modes [64].

In the literature, also many examples of studies to heterojunctions of higher complexity such as *p-n-p'* or *n-p-n'* junctions can be found [29–31] where the same phenomena such as conductance quantization and oscillations have been reported. Referring to the topic of waveguides described in the previous section, also *p-n* junctions can be used to guide electrons in a graphene channel [36].

Furthermore, it is possible to vary the geometry of such a heterojunction. In [37] a STM tip was used to create a circular region with opposite charge carrier polarity with respect to the surrounding area and resulting effects such as whispering gallery modes have been observed.

Both a straight and a circular *p-n* junction in a constant magnetic field have been regarded theoretically in chapter 4 using an inhomogeneous potential $V(\mathbf{r})$.

2.6   LUTTINGER LIQUID

Most itinerant electron systems with three dimensions in which they are free to move can be captured using Landau's Fermi liquid picture [66, 67]. It describes the behaviour of many-

fermion systems without any phase transitions that could break symmetry and can be applied to a vast variety of systems such as metals.

However, once the desire to describe the properties of strongly interacting fermions confined to one dimension arises, which are not included in the Fermi liquid theory, it is convenient to consider the so-called Luttinger liquid picture. In order to arrive at this theory, the concept of the bosonization formalism can be exploited [68]. After going through the steps of this derivation, the result is a Hamiltonian similar to that of an elastic string whose eigenmodes are given by collective low-energy fluctuations of the density. This is one example where Luttinger liquids have characteristics which differ fundamentally from those of higher dimensional Fermi liquids. They on the other hand exhibit incoherent excitations of particle-hole pair type which are absent in a Luttinger liquid, just as single particle or quasiparticle-like excitations in general since all excited states are exclusively given by collective modes. This can be explained using a comparatively simple picture: Imagining a one-dimensional array of particles, one accelerates one of these in one direction. Out of necessity it will hit the next particle in line and transfer its momentum since interactions are allowed. The same procedure also happens to this particle and so on until the entire motion, which initially was localized, spreads throughout the chain.

Another intriguing property of the Luttinger liquid is the so-called spin-charge separation. Beginning from the fact that in a general system with interactions the charge and spin velocities are different, $u_\rho \neq u_\sigma$, meaning that the propagating charge and spin oscillations travel with varying velocities, it is possible to calculate [68] that the respective degrees of freedom have separate dynamics and after a certain time charge and spin are even localized at separate spatial positions. Furthermore, it is possible to define coefficients K_ρ and K_σ which depend heavily on the interaction. The one linked to the spin can be set to unity and thus the resulting power laws are all determined non-trivially by the Tomonaga Luttinger parameter $g_{TLL} = K_\rho$. An important signature is given by the power-law singularity of the momentum distribution function [68]

$$n(k) \propto n_{k_F} - c_1 \text{sgn}(k - k_F)|k - k_F|^\gamma \tag{2.32}$$

and the density of states at the Fermi energy E_F which can be expressed as [68, 69]

$$N(\omega) \propto |\omega|^\gamma \tag{2.33}$$

where $\gamma = (g_{TLL} + 1/g_{TLL} - 2)/4$. The only case where $g_{TLL} = 1$ and thus there is no singularity at the Fermi level, is given for vanishing interactions, i.e. when crossing to the Fermi liquid theory. In this model, the density of states should be finite and the momentum distribution step-like, as discussed in section 2.2.1.

There are also other quantities which can be expressed using asymptotic power laws depending only on g_{TLL} such as the Green function [69]

$$G(x) \propto x^{-1-\gamma}. \tag{2.34}$$

The above named features distinguish a Luttinger liquid clearly from a Fermi liquid and will be used in chapter 3 to identify the material on hand.

2.7 MEAN FIELD THEORY

$\mathcal{A}$ system of many interacting particles is often challenging to describe physically since the motion of one particle is determined by all others due to the interaction correlating all movements. An approximation, which creates a so-called mean field by averaging over the influences of all particles on the one chosen, fabricates an effective single particle problem easier to be solved. This is illustrated in figure 2.9. Moreover, in order to guarantee self-consistency, the mean field is chosen such that the free energy of the system is minimized. This technique is referred to as mean field theory.

2.7.1 GENERAL MECHANISM

$\mathcal{S}$ tarting with a Hamiltonian of the form

$$H = H_0 + V_{int} \tag{2.35}$$

which describes the underlying system composed of particles of two different kinds which are defined via the annihilation (creation) operators $a_\nu^{(\dagger)}$ and $b_\mu^{(\dagger)}$ and whose non-interacting part is given by

$$H_0 = \sum_\nu \xi_\nu^a a_\nu^\dagger a_\nu + \sum_\mu \xi_\mu^b b_\mu^\dagger b_\mu \tag{2.36}$$

while the potential defining the interaction reads

$$V_{int} = \sum_{\nu\nu'\mu\mu'} V_{\nu\mu,\nu'\mu'} a_\nu^\dagger b_\mu^\dagger b_{\mu'} a_{\nu'}, \tag{2.37}$$

following the derivation presented in [61].

The density operators $a_\nu^\dagger a_{\nu'}$ and $b_\mu^\dagger b_{\mu'}$ are assumed to deviate only slightly from the averages $\langle a_\nu^\dagger a_{\nu'} \rangle$ and $\langle b_\mu^\dagger b_{\mu'} \rangle$, and these small differences are declared as $d_{\nu\nu'}$ and $e_{\mu\mu'}$, respectively. Consequently, the Hamiltonian can be rewritten as

$$H = H_0 + V_{MF} + \sum_{\nu\nu'\mu\mu'} V_{\nu\mu,\nu'\mu'} d_{\nu\nu'} e_{\mu\mu'} \tag{2.38}$$

where the second term is the mean field interaction

$$V_{MF} = \sum_{\nu\nu'\mu\mu'} V_{\nu\mu,\nu'\mu'} \left(a_\nu^\dagger a_{\nu'} \langle b_\mu^\dagger b_{\mu'} \rangle + b_\mu^\dagger b_{\mu'} \langle a_\nu^\dagger a_{\nu'} \rangle - \langle a_\nu^\dagger a_{\nu'} \rangle \langle b_\mu^\dagger b_{\mu'} \rangle \right), \tag{2.39}$$
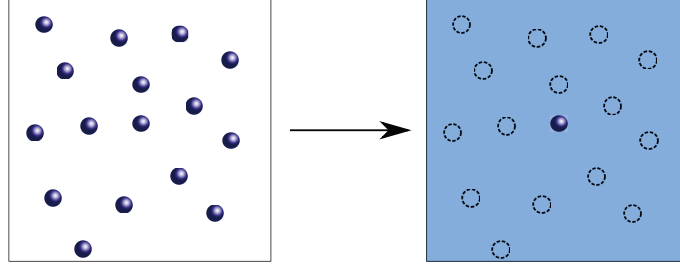
Figure 2.9: The mechanism of the mean field theory leads from the complicated situation of many interacting particles (left) to the situation of one particle under the influence of an averaged background (right). Freely adapted from [61].

and the last term can be neglected since it is by construction given as the product of two small numbers. Thus, the Hamiltonian reduces to $H_{MF} = H_0 + V_{MF}$. The expectation value $\langle a_\nu^\dagger a_{\nu'} \rangle$ can be evaluated self-consistently as

$$\langle a_\nu^\dagger a_{\nu'} \rangle_{MF} = \frac{1}{Z_{MF}} \text{Tr}\left(e^{-\beta H_{MF}} a_\nu^\dagger a_{\nu'} \right) \equiv \langle a_\nu^\dagger a_{\nu'} \rangle \tag{2.40}$$

since it is a result of minimizing the free energy of the system $F_{MF} = -k_B T \ln(Z_{MF})$ [61]. The mean field theory, or special adjustments of it, find application in several fields such as ferromagnets, superconductors where BCS theory is used (compare section 2.8.4) or the electron gas where the formulation of the mean field theory is called Hartree-Fock method.

2.7.2 HARTREE-FOCK METHOD

Reducing the situation considered in the previous chapter to just one species of particles, or, to be more precise, electrons, only one set of operators remains necessary and the indices μ and ν henceforth refer to the identical set of single particle states. The mean field theory for these special requirements is referred to as Hartree-Fock theory.

The Hamiltonian consists again of the two parts already described earlier

$$H = H_0 + V_{int} \tag{2.41}$$

but unlike before, the interaction term now contains more possible parts. While in the system with two different kinds of particles only direct interactions among one kind were allowed, which are called Hartree type interactions, with identical particles also the exchange, or Fock term is possible. Thus, the interaction potential can be written as [61]

$$V_{int} = \frac{1}{2} \sum_{\nu\nu'\mu\mu'} V_{\nu\nu',\mu\mu'} c_\nu^\dagger c_\mu^\dagger c_{\mu'} c_{\nu'} \tag{2.42}$$

where the ladder operator product $c_\nu^\dagger c_\mu^\dagger c_{\mu'} c_{\nu'}$ is within the picture of the mean field theory approximated as [62]

$$
\begin{aligned}
c_\nu^\dagger c_\mu^\dagger c_{\mu'} c_{\nu'} &\approx c_\nu^\dagger c_{\nu'} \langle c_\mu^\dagger c_{\mu'} \rangle_{MF} + \langle c_\nu^\dagger c_{\nu'} \rangle_{MF} c_\mu^\dagger c_{\mu'} \\
&\pm c_\nu^\dagger c_{\mu'} \langle c_\mu^\dagger c_{\nu'} \rangle_{MF} \pm \langle c_\nu^\dagger c_{\mu'} \rangle_{MF} c_\mu^\dagger c_{\nu'} \\
&- \langle c_\nu^\dagger c_{\nu'} \rangle_{MF} \langle c_\mu^\dagger c_{\mu'} \rangle_{MF} \mp \langle c_\nu^\dagger c_{\mu'} \rangle_{MF} \langle c_\mu^\dagger c_{\nu'} \rangle_{MF}.
\end{aligned}
\tag{2.43}
$$

This is a general expression where the upper arithmetic operator refers to bosons while the lower applies if there are fermionic particles to be considered, like in the example of electrons. The first two terms correspond to the direct interaction, the third and fourth yield the exchange interaction and the last two terms consisting of averages are subtracted in order to avoid double counting [61].

From this expression, the Hartree and Fock terms can be read off as

$$
\begin{aligned}
V_{int}^{Hartree} = \frac{1}{2} \sum V_{\nu\mu,\nu'\mu'} \overline{n}_{\mu\mu'} c_\nu^\dagger c_{\nu'} &+ \frac{1}{2} \sum V_{\nu\mu,\nu'\mu'} \overline{n}_{\nu\nu'} c_\mu^\dagger c_{\mu'} \\
&- \frac{1}{2} \sum V_{\nu\mu,\nu'\mu'} \overline{n}_{\nu\nu'} \overline{n}_{\mu\mu'}
\end{aligned}
\tag{2.44}
$$

where the $\overline{n}_{\lambda,\kappa}$ are abbreviated notations for the averages and

$$
\begin{aligned}
V_{int}^{Fock} = -\frac{1}{2} \sum V_{\nu\mu,\nu'\mu'} \overline{n}_{\nu\mu'} c_\mu^\dagger c_{\nu'} &- \frac{1}{2} \sum V_{\nu\mu,\nu'\mu'} \overline{n}_{\mu\nu'} c_\nu^\dagger c_{\mu'} \\
&+ \frac{1}{2} \sum V_{\nu\mu,\nu'\mu'} \overline{n}_{\nu\mu'} \overline{n}_{\mu\nu'}.
\end{aligned}
\tag{2.45}
$$

At last, the mean field Hamiltonian according to the Hartree-Fock approximation can be obtained as

$$
H^{HF} = H_0 + V_{int}^{Hartree} + V_{int}^{Fock}.
\tag{2.46}
$$

2.7.3 APPLICATION: COULOMB INTERACTION

$\mathcal{C}$onsidering the case of a homogeneous electron gas as hinted at before, the underlying interaction is caused by electric forces and called Coulomb interaction. In second quantized form it is in momentum space expressed as [61]

$$
V = \frac{1}{2\mathcal{V}} \sum_{\sigma_1 \sigma_2} \sum_{\mathbf{k}_1 \mathbf{k}_2 \mathbf{q}} V_\mathbf{q} c_{\mathbf{k}_1+\mathbf{q},\sigma_1}^\dagger c_{\mathbf{k}_2-\mathbf{q},\sigma_2}^\dagger c_{\mathbf{k}_2,\sigma_2} c_{\mathbf{k}_1,\sigma_1}
\tag{2.47}
$$

with the volume $\mathcal{V}$, the spin states encoded in $\sigma_{(1,2)}$, the momenta of the incoming electrons $\mathbf{k}_{(1,2)}$, the exchange momentum $\mathbf{q}$ and the coulomb potential $V_\mathbf{q}$. This situation is depicted in
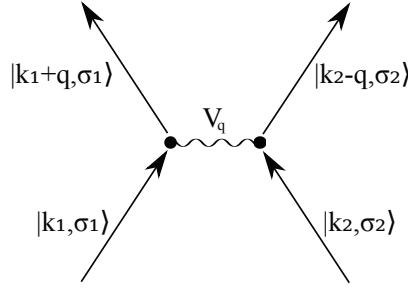
Figure 2.10: Feynman diagram illustrating the Coulomb interaction with incoming particles with wave momenta $\mathbf{k}_1$, $\mathbf{k}_2$ and spins σ_1 and σ_2, respectively, which interact via the Coulomb potential V_q and exiting particles with the properties $\mathbf{k}_1 + \mathbf{q}, \sigma_3$ and $\mathbf{k}_2 - \mathbf{q}, \sigma_4$.

figure 2.10.

With this the Hartree-Fock Hamiltonian for Coulomb interactions in electron gas follows as

$$H^{HF} = \sum_{\mathbf{k}\sigma} \xi_{\mathbf{k}}^{HF} c_{\mathbf{k}\sigma}^{\dagger} c_{\mathbf{k}\sigma} \tag{2.48}$$

with the quantity

$$\xi_{\mathbf{k}}^{HF} = \xi_{\mathbf{k}} + \sum_{\mathbf{k}',\sigma'} (V_0 - \delta_{\sigma,\sigma'} V_{\mathbf{k}-\mathbf{k}'}) n_{\mathbf{k}'\sigma'}. \tag{2.49}$$

Regarding this expression, the conclusion can be drawn that the direct or Hartree interaction corresponds to outgoing electrons which have the same properties as the incoming ones since the interaction process took place with an exchange momentum of $\mathbf{q} = 0$, while for the exchange or so-called Fock term the exchange momentum reads $\mathbf{q} = \mathbf{k} - \mathbf{k}'$. This is the case if the electrons actually exchange their momenta during the process.

The Hartree-Fock method will be employed in chapter 3.4 to treat the intraband interactions in the 0th6 Landau level in the zero mode sector.

2.8 SUPERCONDUCTIVITY

Yet another interesting example where symmetry breaking happens and a formulation of the mean field theory can be applied, is given by the superconducting phase transition occurring in superconductors.

2.8.1 RESISTANCE IN NORMAL CONDUCTORS

Generally, as already described in the models in section 2.2.1, ions vibrate around their lattice positions with quantized frequencies up to the maximally possible so-called Debye fre-
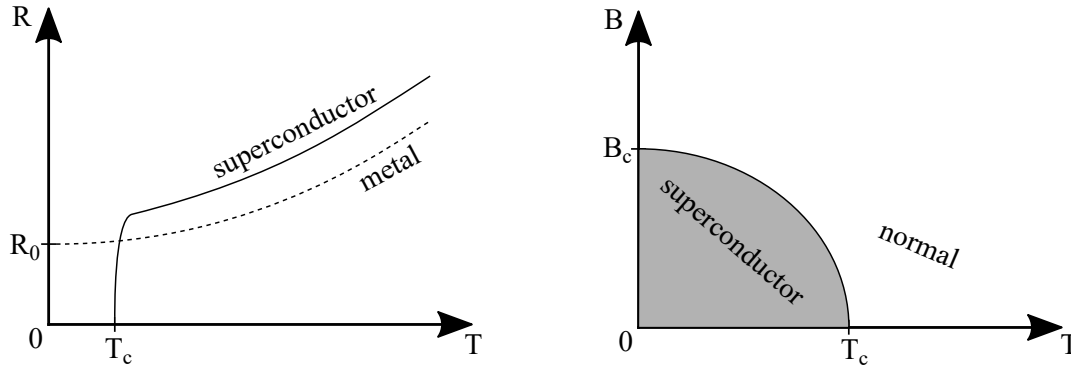
Figure 2.11: Left: Comparison of the resistance of normal metals and superconductors depending on the temperature. Right: The parameters of the critical temperature T_C and magnetic field B_C determine the transition between a normal and a superconducting material. Freely adapted from [70].

quency and electrons are randomly scattered due to these vibrations causing electron-phonon interaction. When an additional electrical potential is applied, the electrons get an overall drift and a current flows. Due to scattering at the vibrating ions or impurities, energy of the electrons is lost and absorbed by the lattice in the form of heat. As a cause of this dissipation, there is resistance, which for normal metals can be expressed as proportionality factor between current and applied voltage

$$V = R \cdot I. \tag{2.50}$$

This simple expression is called Ohm's law and captures despite its plainness the underlying physics in a wide range of resistance up to 24 orders of magnitude [70].

The resistance, however, is not a fixed value but depends on the temperature. While there is a temperature-independent part that originates from electron scattering at impurities or other imperfections in the material and leads to a finite resistance R_0 at zero temperature, the lattice oscillations and thus the scattering due to phonons lowers with decreasing temperature.

2.8.2 CONFINES OF SUPERCONDUCTORS

Different from normal conductors, superconductors don't develop a saturated finite resistance at low temperatures, as the Dutch physicist H. Kammerlingh Onnes found in 1911 but their resistance drops to zero below a certain critical temperature[1] T_C, compare the left panel of figure 2.11. Considering different isotopes of the same metal leads to the conclusion that the value of this critical temperature depends on the atomic mass as $T_C \propto M^{-1/2}$, which means that the lattice influences the process but only very subtly.

---

[1] There are also other materials which only exhibit superconducting properties under high pressure or as thin films [70].

Nevertheless, not only increasing the temperature can destroy the superconducting effect but also the raise of an external magnetic field, see figure 2.11, right panel. The critical magnetic field B_C at which superconductivity is destroyed depends on the temperature and can be expressed as [70]

$$B_C = B_0 \left[1 - \left(\frac{T}{T_C} \right)^2 \right].$$
(2.51)

Thus, the maximum value B_0 is reached for $T = 0K$ while B_C vanishes at the critical temperature. For most elemental superconductors B_C is very low [70]. The sharpness of the transition between super- and normal conductor upon reaching the critical field is defined by several parameters such as the relative direction and the geometry of magnetic field and material.

In addition to these two values, there is also a third quantity, namely the critical current I_C that can destroy superconductivity. It can be obtained as the current which will produce a magnetic field of the same magnitude as B_C.

2.8.3 MEISSNER EFFECT

As in a superconductor $E = 0$ must be true since it is not able to sustain electric voltages, one can deduce from Maxwell's equation that the magnetic flux inside it should be constant due to

$$\frac{\partial B}{\partial t} = -\nabla \times E = 0.$$
(2.52)

Thus, once a perfect conductor is placed inside a magnetic field, the flux should be constant within, also when it is cooled below the critical temperature T_C. This, however, is not the result found when observing the given situation. Instead of being frozen in the superconductor, the magnetic field is pushed outside of its volume, see figure 2.12. This effect is named Meissner effect after its discoverer Walter Meissner who found it in 1933 together with Robert Ochsenfeld [71]. The order of the two limits, i.e. whether the superconducting material is first placed in the magnetic field and then cooled down or vice versa, does not affect this finding in stark contrast to the

$T > T_c$ $\qquad\qquad\qquad$ $T < T_c$
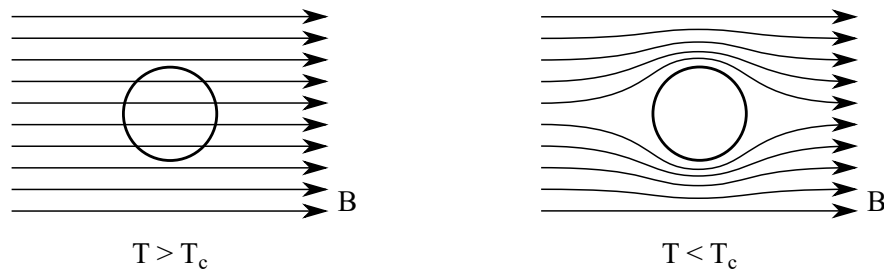
Figure 2.12: Illustration of the Meissner effect. Left panel: In a normal conductor, the magnetic field is also present inside the volume. Right panel: In a superconductor, the magnetic field lines are excluded from the body. Loosely based on [70].

situation at hand in normal conductors. This suggests that superconductivity can be regarded as a thermodynamical phase [70]. The expulsion of the magnetic field can be rationalised in terms of a screening current which runs along the surface and causes a magnetic field of the same magnitude and opposite orientation with respect to the external field, making the superconductor a perfect diamagnet with susceptibility $\chi = -1$ [70]. This property can be used to levitate a magnet over a superconductor.

The screening current flowing across the surface has to have a small but finite extension inside the material since otherwise the current density at the surface would be infinite. Therefore, also the magnetic field can reach into the superconductor although being exponentially suppressed according to

$$B(x) = B_0 e^{-\frac{x}{\lambda}} \tag{2.53}$$

with the so-called penetration depth λ whose magnitude is around $10-100\,\text{nm}$ for most pure metals [70]. Also the penetration depth depends on the temperature: Whereas between zero temperature and about $0.8 T_C$ it is nearly constant, it then rises exponentially fast until it is infinitely large at the critical temperature.

The magnetisation increases with rising external magnetic field and thus works against the penetration and then falls to zero upon advancing B_C, which turns out to be a reversible process. As a result of the expulsion of magnetic field lines from the interior of the superconductor, there is a higher concentration of these lines close to its surface, which leads to a modification of the value of B_C. This demagnetization effect depends on the geometry and the relative orientation of field and material[2] [70]. The inner magnetic field is given as

$$B_i = \frac{B_e}{1 - n} \tag{2.54}$$

as a function of the externally applied magnetic field B_e and the demagnetization factor n.

As a result, it is possible that there are conflicting points: Due to the above formula it can happen for non-zero n that the external field $B_e = B_C$ is applied such that the material should transform into a normal conductor. If that had happened however, the magnetization would have become approximately zero and the inner field would only still be a fraction of the critical field leading to a superconducting behaviour. Thus, between this certain fraction determined as $B_C/(1-n)$ and B_C the material is neither completely normal nor superconducting but is in an intermediate state. It manifests as alternating layers of superconducting and normal behaving material throughout the sample, which are oriented parallel to the field [70]. With increasing magnetic field, the proportion of normal areas increases at the cost of the superconducting amount and hence, the resistance grows continuously.

---

[2]E.g. for a spherical superconductor, the demagnetization factor is $n = 1/3$ whereas for a long but thin cylindrical shaped superconductor it depends on the relative orientation and is zero parallel to the axis and $n = 1/2$ for a perpendicular field [70].

2.8.4 BCS THEORY

$\mathcal{A}$s already mentioned in section 2.7, there is also a symmetry breaking for the transition from a normal to a superconductor: it is given by the loss of gauge invariance [61], which means that it is possible to add a constant phase for all electrons without changing the Hamiltonian. This was investigated by Bardeen, Cooper and Schrieffer and thus is called BCS theory. One finds, that it is possible within these materials to minimize their free energy by carrying a dissipationless current as long as the energy cost for this lies below the cost for leaving the superconducting state. The critical current I_C is reached when both energies are the same. Since the electron-electron interaction mediated by phonons is known [61] to couple electrons with opposite spin $\sigma = \uparrow, \downarrow$ and momentum $\mathbf{k}$, an operator for so-called Cooper pairs can be defined as

$$b_{\mathbf{k}} = c_{\mathbf{k},\downarrow} c_{-\mathbf{k},\uparrow}. \tag{2.55}$$

The BCS Hamiltonian reads [72]

$$H_{BCS} = \sum_{\mathbf{k},\sigma} \xi_{\mathbf{k}} c_{\mathbf{k},\sigma}^{\dagger} c_{\mathbf{k},\sigma} + \sum_{\mathbf{k},\mathbf{k}'} V_{\mathbf{k}\mathbf{k}'} c_{\mathbf{k},\uparrow}^{\dagger} c_{-\mathbf{k},\downarrow}^{\dagger} c_{-\mathbf{k}',\downarrow} c_{\mathbf{k}',\uparrow} \tag{2.56}$$

with a coupling strength $V_{\mathbf{k}\mathbf{k}'}$. This interaction leads to the coupling of electrons in time reversed states as Cooper pairs.

Going through the steps described for the Hartree Fock method described in section 2.7.2, assuming that the finite expectation value of the pair operator does not vary by a lot from its average, the Hamiltonian can be rewritten as

$$H_{BCS}^{MF} = \sum_{\mathbf{k}} \begin{pmatrix} c_{\mathbf{k},\uparrow}^{\dagger} & c_{-\mathbf{k},\downarrow} \end{pmatrix} \underbrace{\begin{pmatrix} \xi_{\mathbf{k}} & \Delta_{\mathbf{k}} \\ \Delta_{\mathbf{k}}^{*} & -\xi_{\mathbf{k}} \end{pmatrix}}_{\mathbf{H_k}} \begin{pmatrix} c_{\mathbf{k},\uparrow} \\ c_{-\mathbf{k},\downarrow}^{\dagger} \end{pmatrix} + \text{const.} \tag{2.57}$$

Using a unitary transformation

$$\mathbf{U_k} = \begin{pmatrix} u_{\mathbf{k}} & -v_{\mathbf{k}} \\ v_{\mathbf{k}}^{*} & u_{\mathbf{k}}^{*} \end{pmatrix} \tag{2.58}$$

the problem can be diagonalized via

$$\mathbf{U_k^{\dagger} H_k U_k} = \begin{pmatrix} E_{\mathbf{k}} & 0 \\ 0 & \tilde{E}_{\mathbf{k}} \end{pmatrix} \tag{2.59}$$

with

$$\begin{aligned} |u_{\mathbf{k}}|^2 &= \frac{1}{2} \left(1 + \frac{\xi_{\mathbf{k}}}{E_{\mathbf{k}}} \right) \\ |v_{\mathbf{k}}|^2 &= \frac{1}{2} \left(1 - \frac{\xi_{\mathbf{k}}}{E_{\mathbf{k}}} \right) \end{aligned} \tag{2.60}$$

and

$$E_{\mathbf{k}} = \sqrt{\xi_{\mathbf{k}}^2 + |\Delta_{\mathbf{k}}|^2} = -\tilde{E}_{\mathbf{k}}. \tag{2.61}$$

Considering the newly found fermionic operators which diagonalize this Hamiltonian and obey the transformation [61]

$$\begin{pmatrix} \gamma_{\mathbf{k},\uparrow} \\ \gamma_{-\mathbf{k},\downarrow}^\dagger \end{pmatrix} = \begin{pmatrix} u_{\mathbf{k}}^* & v_{\mathbf{k}} \\ -v_{\mathbf{k}}^* & u_{\mathbf{k}} \end{pmatrix} \begin{pmatrix} c_{\mathbf{k},\uparrow} \\ c_{-\mathbf{k},\downarrow}^\dagger \end{pmatrix} \tag{2.62}$$

from the old operators, one finds that they are composed as superpositions of electrons and holes and with these so-called bogoliubons, the Hamiltonian reads

$$H_{BCS}^{MF} = \sum_{\mathbf{k}} E_{\mathbf{k}}(\gamma_{\mathbf{k},\uparrow}^\dagger \gamma_{\mathbf{k},\uparrow} + \gamma_{\mathbf{k}\downarrow}^\dagger \gamma_{\mathbf{k}\downarrow}) + \text{const.} \tag{2.63}$$

From equation (2.61) it becomes obvious that no fermion excitations are possible with an energy of less than the value $|\Delta|$. Thus, this mean field parameter creates an energy gap in the spectrum, the so-called superconducting gap, which is given as [72]

$$\Delta_{\mathbf{k}} = -\sum_{\mathbf{k}'} V_{\mathbf{k}\mathbf{k}'} \frac{\Delta_{\mathbf{k}'}}{2E_{\mathbf{k}'}}. \tag{2.64}$$

This is the self-consistent BCS equation. BCS theory also gives a prediction linking this parameter to the critical temperature as [61, 72]

$$\frac{2\Delta(T=0)}{k_B T_C} = 3.53 \tag{2.65}$$

in good agreement with experiments. It behaves similar as the gaps in semiconductors but is about three orders of magnitude smaller [70]. Plotting the ratio $\Delta(T)/\Delta(T=0)$ against T/T_C yields a universal curve on which all BCS-superconducting materials lie.

The theory that states that the Cooper pairs and normal electrons can be regarded as two different fluids which mix between $T = 0$ where only Cooper pairs exist and T_C where there are only normal electrons, is called Two Fluid Model. It can be utilized to explain the peak in the specific heat at T_C as being caused by the additional amount of energy needed to excite a Cooper pair to a normal state [70], which can be identified with the superconducting gap.

Measuring the magnetic flux in a free space surrounded by a superconducting cylinder yields quantized values with a quantum of $\Phi_0 = h/2e$ where the factor of $2e$ is given by the charge of a Cooper pair [70].

The value of the energy gap can be determined using single particle tunnel experiments where a sharp jump in the current-voltage characteristic can be observed once the applied voltage reaches Δ/e.

2.8.5 NAMBU FORMALISM

An alternative notation for the above problem is the Nambu formalism. Its applicability is founded on the similarities between the Fröhlich interaction and Coulomb based electron-electron interaction. In, 1960 Yoichiro Nambu found a way to alter the formalism that was formerly used for the normal state such that it could be applied to the superconducting state [73]. Within the formalism, a spinor consisting of two components for the electron

$$\psi_{\mathbf{k}} = \begin{pmatrix} c_{\mathbf{k},\uparrow} \\ c_{-\mathbf{k},\downarrow}^{\dagger} \end{pmatrix}, \qquad \psi_{\mathbf{k}}^{\dagger} = \begin{pmatrix} c_{\mathbf{k},\uparrow}^{\dagger} & c_{-\mathbf{k},\downarrow} \end{pmatrix} \tag{2.66}$$

is constructed as before, and additionally a bare-phonon field operator

$$\phi_{\mathbf{q},\nu} = b_{\mathbf{q},\nu} + b_{-\mathbf{q},\nu}^{\dagger} \tag{2.67}$$

is implemented with $\mathbf{q}$ being the wave vector of the phonon defining the momentum exchange due to the Coulomb interaction and ν the phonon mode.

With this, the Hamiltonian of a system of electrons and phonons interacting via Coulomb interactions can be formulated as [72]

$$\begin{aligned}
H &= \sum_{\mathbf{k}} \epsilon_{\mathbf{k}} \psi_{\mathbf{k}}^{\dagger} \sigma_z \psi_{\mathbf{k}} + \sum_{\mathbf{q},\nu} \Omega_{\mathbf{q},\nu} b_{\mathbf{q},\nu}^{\dagger} b_{\mathbf{q},\nu} + \sum_{\mathbf{k},\mathbf{k}',\nu} g_{\mathbf{k},\mathbf{k}',\nu} \phi_{\mathbf{k}-\mathbf{k}'} \psi_{\mathbf{k}'}^{\dagger} \sigma_z \psi_{\mathbf{k}} \\
&+ \frac{1}{2} \sum_{\mathbf{k}_1,\mathbf{k}_2,\mathbf{k}_3,\mathbf{k}_4} \langle \mathbf{k}_3 \mathbf{k}_4 | V_C | \mathbf{k}_1 \mathbf{k}_2 \rangle (\psi_{\mathbf{k}_3}^{\dagger} \sigma_z \psi_{\mathbf{k}_1})(\psi_{\mathbf{k}_4}^{\dagger} \sigma_z \psi_{\mathbf{k}_2})
\end{aligned} \tag{2.68}$$

with the Bloch energy of an electron $\epsilon_{\mathbf{k}}$, the energy of a phonon $\Omega_{\mathbf{q},\nu}$, the matrix elements $g_{\mathbf{k},\mathbf{k}',\nu}$ of the electron-phonon interaction, the Coulomb potential V_C, which encodes the interaction of incoming and outgoing electrons with the different wavevectors $\mathbf{k}_i$, and the z-Pauli matrix $\sigma_z = \text{diag}(1, -1)$.

2.8.6 PROXIMITY-INDUCED SUPERCONDUCTIVITY

The Hamiltonian for a s-wave superconductor[3] with the gap Δ can be written as [74]

$$H_s = \frac{1}{2} \int d^3 r \psi^{\dagger}(\mathbf{r})(\xi_{\mathbf{p}} \sigma_z + \Delta \sigma_x) \psi(\mathbf{r}) \tag{2.69}$$

where

$$\xi_{\mathbf{p}} = \frac{\mathbf{p}^2}{2m} - \mu \tag{2.70}$$

---

[3]This notation relates to the symmetry, e.g. the gap with s-wave symmetry is $\Delta \sim \Delta_0 e^{i\phi}$.

is the normal state dispersion and the four-component Nambu spinors are given as

$$\psi(\mathbf{r}) = (\psi_\uparrow(\mathbf{r}), \psi_\downarrow(\mathbf{r}), \psi_\downarrow^\dagger(\mathbf{r}), -\psi_\uparrow^\dagger(\mathbf{r}))^T \tag{2.71}$$

where T denotes transposition. When put in the vicinity of another material, e.g. a one-dimensional wire, the superconductor provides modification of the physics of the wire due to the proximity effect and the Bogoliubov-de Gennes Hamiltonian of the one-dimensional system reads

$$H_d = \frac{1}{2} \int dx d^\dagger(x) \mathcal{H}_d d(x) \tag{2.72}$$

with

$$d(x) = (d_\uparrow(x), d_\downarrow(x), d_\downarrow^\dagger(x), -d_\uparrow^\dagger(x))^T. \tag{2.73}$$

Close to the Fermi energy,

$$\mathcal{H}_d = v_f p_x \sigma_z \tag{2.74}$$

follows with the momentum p_x relative to the Fermi point. Finally, the hybridization between the wire and the superconductor can be expressed via [74]

$$H_T = -\frac{t}{2} \int d^3 r [\psi^\dagger(\mathbf{r}) \sigma_z d(x) + d^\dagger(x) \sigma_z \psi(\mathbf{r})] \delta(y) \delta(z). \tag{2.75}$$

After some calculations, the induced gap follows as

$$\Delta_{ind} = Z \cdot \Gamma \simeq \begin{cases} \Gamma & \text{for } \Gamma \ll \Delta \\ \Delta & \text{for } \Gamma \gg \Delta \end{cases} \tag{2.76}$$

with a renormalization factor

$$Z = \frac{1}{1 + \frac{\Gamma}{\Delta}} \tag{2.77}$$

and $\Gamma = 2\pi \nu_0 t^2$ and the two-dimensional density of states ν_0 at the Fermi energy. This quantity massively modifies the spectrum according to

$$E(k) = \pm\sqrt{(Zv_F k)^2 + (\Delta_{ind})^2} \tag{2.78}$$

as well as the coherence length of the proximity-induced superconductivity

$$\xi = \frac{\hbar v_F}{\Gamma} \tag{2.79}$$

which is much smaller than the coherence length of the original s-wave superconductor for strong hybridization.

What happens if one combines a superconducting layer and a graphene sheet, thus introducing a proximity-induced superconducting gap also in the Hamiltonian of this system, will be discussed in chapter 5.

2.8.7 MAJORANA MODES

Majorana bound states have hermitian operators as creation and annihilation operators, i.e.

$$\gamma = \gamma^{\dagger} \tag{2.80}$$

and possess no dispersion depending on a momentum quantum number [74]. If they are in addition spatially isolated, they have zero excitation energy and other (non-Majorana) excitations are separated by a finite energy gap. Furthermore, when trying to define their quantum statistics, one finds out that they are neither bosonic nor fermionic. Instead, they seem to be of an entirely new type, which is denoted as nonabelian quantum statistics. This means that upon the exchange of two Majorana bound states, the resulting many-body state is neither unchanged (as would be the case for bosons obeying commutator algebra) nor simply multiplied with a minus sign (as for the fermionic anti-commutator algebra) but is subject to a unitary rotation in the subspace of the degenerate ground state [74].

It is no use to search for an excitation consisting in identical parts of electrons and holes to allow for the properties mentioned above in a normal metal or semiconductor because such excitons are bound states of two fermions, namely an electron sitting in the conduction band and a hole situated in the valence band. Thus, they are realized by products of two fermionic operators describing electrons and holes and hence obey bosonic algebra [74]. Required, on the other hand is an operator linear in fermionic operators and consisting in equal parts of electron and hole states such as

$$\gamma = c + c^{\dagger}. \tag{2.81}$$

This is closely related to the bogoliubons created in the BCS theory except for the fact that they are usually defined with a spin part as $\gamma_{\uparrow} = uc_{\uparrow} + vc_{\downarrow}^{\dagger}$ which spoils the wanted relation since then $\gamma_{\uparrow} \neq \gamma_{\uparrow}^{\dagger}$. Thus, the considered fermions have to be spinless in order to fulfil the algebra. This requirement, however, makes it impossible to use a conventional s-wave superconductor since its electrons have anti-symmetric spin singlet configurations while the orbital wave function obeys s-symmetry. The easiest solution is to use a spinless so-called p-wave superconductor whose orbital electron wave functions are antisymmetric and to search for zero-energy excitations in this setting. Indeed, it is possible to construct Majorana bound states in this environment [74].

2.8.8 THERMODYNAMICAL PROPERTIES

Exploiting the laws of thermodynamics, a lot of specialities of superconductors can be found which will be briefly summarized here. Firstly, the difference between the Gibbs free

energies of a superconductor in the normal and superconducting state without external magnetic field is given as

$$g_n(T, B_e = 0) - g_s(T, B_e = 0) = \frac{\mu_0 B_C^2}{2} \tag{2.82}$$

with the vacuum permeability μ_0. This prediction can be precisely verified experimentally [70]. The entropy of such a material in the superconducting state is always lower than in the normal state, defining the superconducting one as an ordered state. This fact can be used to cool down a sample as a result of applying a magnetic field.

The in comparison most characteristic feature for superconductors is, however, as mentioned above, the anomaly in the specific heat which has a jump at the critical temperature T_C.

In the absence of an external magnetic field, both the free energy and the entropy are continuous at T_C and these facts combined with the jump in the specific heat render this a transition of second order. In the presence of a finite magnetic field, on the other hand, the situation looks different. Both the latent heat, which is proportional to the difference of entropies, and the critical value B_C, which defines the difference in the free energies according to (2.82), are non-zero and the transition becomes first order.

Superconductors can also be used as thermal switches in the low temperature regime since their thermal conductivity decreases orders of magnitude at the critical temperature.

Furthermore, the Seebeck, Peltier and Thomson coefficients are all zero in superconductors making them perfect devices to measure the thermoelectric power of another material [70].

2.8.9 COHERENCE LENGTH

Another characteristic parameter is given by the coherence length. The fact, that the transition happens at a very sharp temperature up to $10^{-5} K$ implies that there must be long range phase coherence between the Cooper pairs taking part in the transition process. The distance over which the order parameter will change at the interface between a superconductor and a normal conductor is defined as coherence length. This quantity depends on the purity of the material since it is proportional to the mean free path of the electrons.

2.8.10 JOSEPHSON EFFECT

Combining two superconductors just separated by a thin insulating layer leads to the so-called DC Josephson effect. Below the critical temperature, Cooper pairs build due to virtual phonon interactions as described before and then condense to a ground state where all pairs have identical quantum-mechanical phase ϕ and can be described via one macroscopic wave function. The Cooper pairs face no resistance for tunnelling through the insulating layer and thus generate a supercurrent

$$I = I_C \sin(\Delta\phi) \tag{2.83}$$

which again leads to a phase difference $\Delta\phi$ between the superconducting order parameters on both sides. The critical current of the junction, denoted as I_C depends both on the temperature and parameters of the junction. For $I > I_C$ there is a finite voltage [70].

So far, there was no external electric field difference but still a supercurrent flow was observed. When a finite voltage is applied, the supercurrent oscillates with time at frequency $\nu = V/\Phi_0 =$ 484 MHz/µV·V[µV] [70] with the flux quantum Φ_0 defined earlier. The current-voltage characteristic exhibits plateaus at quantized values

$$V_n = \frac{nhf}{2e} \tag{2.84}$$

of the voltage with an integer n and a microwave frequency f with which the step height fluctuates. This means that whenever the condition $\nu \pm nf = 0$ is fulfilled, a new plateau emerges. The height of the plateau is again determined by the charge of a Cooper pair since when for a given voltage V the requirement $2eV = nhf$ is met, a Cooper pair can tunnel through the junction coherently with the absorption or emission of n microwave photons of frequency f [70].

2.8.11 EXPERIMENTAL VERIFICATION: SQUID-TECHNOLOGY

Both the Josephson effect and the flux quantization can be exploited to create a device referred to as **S**uperconducting **Qu**antum **I**nterference **D**evice (SQUID), which enables the user to measure magnetic fields as weak as $10^{-15}T$ in a wide range of application fields such as biomagnetism (e.g. to measure the neural activity inside a human brain), geomagnetism and solid state physics [70].

A DC SQUID can be built from two Josephson junctions put together on a superconducting ring with two side arms which are positioned at the two central points between the junctions. The current enters from one of these arms, say the left, and exits through the other. Such a device is shown in figure 2.13. In between, it branches in the two possible halves of the ring leading to interference effects as known from laser experiments such as the double slit fringes. This is possible since the Cooper pairs form a single wave function and are in phase, comparable to coherent light.

Since there are the DC Josephson junctions in the branches, there will be a finite voltage across the entire device once the current in the branch is larger than the critical current. The critical supercurrent of the junction reacts furthermore sensitively to the application of an external magnetic flux through the ring. It shows maximum values for a vanishing flux as well as for integer values of the flux quantum Φ_0 and is minimal for half-integer values of Φ_0.

Hence, as a consequence of interference both current and voltage fluctuations can be observed which resemble diffraction patterns. Due to its mechanism, the SQUID can detect small magnetic fields of the size of a fraction of the flux quantum making the creation of real time brain maps possible.
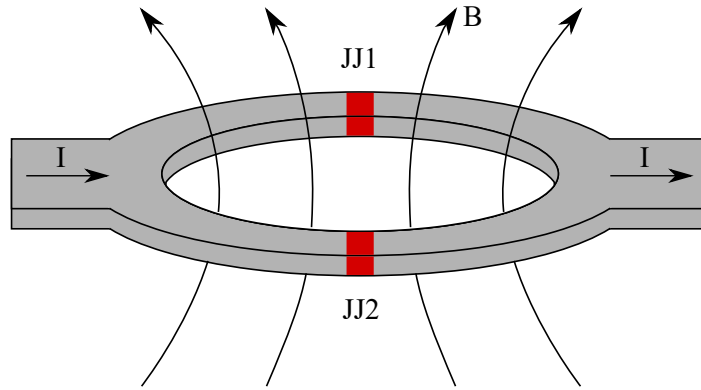
Figure 2.13: Schematic drawing of a SQUID where insulating material is distinguished as red while the superconductor is grey. Adapted from [70].

Another possibility is to build a resonant frequency (rf) SQUID which only needs one AC Josephson junction. If the AC current reaches its resonant frequency, the voltage across the ring, which again is interspersed by a magnetic flux, oscillates with the periodicity of the flux quantum. This device has to be cooled to the temperature of liquid helium [70].

The SQUID method can be utilized to experimentally test some of the results shown in chapter 4.

2.9   PERTURBATION THEORY

Exact solutions to mathematical problems are often beyond reach or depend intricately on the different parameters so that they can hardly be used. Approximate solutions can be achieved from a number of mathematical tools included in the perturbation theory. It can be exploited if the problem can be expressed in two terms where the first has a strong effect on the system and is exactly solvable and the second constitutes only a small perturbation as [75]

$$T(x) = T + xT'. \tag{2.85}$$

Here, x is a scalar parameter which is assumed to be small, xT' is the perturbation and $T(0) = T$ gives the uperturbed situation. It is now possible to express such a problem as Taylor expansion in x as

$$T(x) = T + xT^{(1)} + x^2 T^{(2)} + \dots . \tag{2.86}$$

Since the perturbation and thus the deviation from the exact solution for the unperturbed system is supposed to be small, it can be argued to truncate the series after a certain number of terms. Inserting this approximation into the original problem and solving for the different terms finally yields the values of the quantities $T^{(n)}$ and a sufficiently good estimation of the wanted solution, unless the problem is nonperturbative.

2.10 LINEAR RESPONSE THEORY
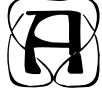
Another way of handling the influence of an external perturbation on a system is given by the linear response theory. As the name already tells, it assumes that the response of an observable to this small perturbation is proportional to it and only leaves the question how the coefficient defining this proportionality looks like.

2.10.1 KUBO FORMULA

Regarding a quantum system, which in thermodynamic equilibrium is described via the unperturbed Hamiltonian H_0, with an added time dependent perturbation $H'(t)$ switched on at a time $t = t_0$ according to

$$H(t) = H_0 + H'(t)\theta(t - t_0), \tag{2.87}$$

the expectation value of an operator A at a time $t > t_0$ is given as [61]

$$\langle A(t) \rangle = \frac{1}{Z_0} \sum_n \langle n(t)|A|n(t) \rangle e^{-\beta E_n} = \frac{1}{Z_0} \text{Tr}[\rho(t)A]. \tag{2.88}$$

In this expression, $Z_0 = \text{Tr}[\rho_0]$ is the partition function to the density operator ρ_0, the $\{|n(t)\rangle\}$ form a complete set of time dependent eigenstates with eigenenergies $\{E_n\}$, evolving according to the Schrödinger equation

$$i\partial_t |n(t)\rangle = H(t)|n(t)\rangle, \tag{2.89}$$

$\beta = 1/k_B T$ is the inverse temperature and the density matrix evolving with time reads

$$\rho(t) = \sum_n |n(t)\rangle\langle n(t)|e^{-\beta E_n}. \tag{2.90}$$

It is convenient to consider the interaction picture denoted as $|\hat{n}(t)\rangle = e^{iH_0 t}|n(t)\rangle$ and thus

$$|n(t)\rangle = e^{-iH_0 t}|\hat{n}(t)\rangle = e^{-iH_0 t}\hat{U}(t, t_0)|\hat{n}(t_0)\rangle \tag{2.91}$$

with the unperturbed initial eigenstates $|n(t_0)\rangle$ and the unitary operator [61]

$$U(t, t_0) = e^{iH_0 t}e^{-iH(t-t_0)}e^{-iH_0 t_0} \approx 1 - i \int_{t_0}^t dt' H'(t'). \tag{2.92}$$

With this the expectation value follows to first order in the perturbation as

$$
\begin{aligned}
\langle A(t) \rangle &= \langle A(t) \rangle_0 - i \int_{t_0}^{t} dt' \frac{1}{Z_0} \sum_n e^{-\beta E_n} \langle n(t_0) | A(t) H'(t') - H'(t') A(t) | n(t_0) \rangle \\
&= \langle A(t) \rangle_0 - i \int_{t_0}^{t} dt' \langle [A(t), H'(t')] \rangle_0
\end{aligned}
\tag{2.93}
$$

where $\langle ... \rangle_0$ denotes averaging in the equilibrium situation with only H_0 acting on the system and $[x, y] = xy - yx$ is a commutator. This result can be rewritten using the retarded correlation function

$$
C_{AH'}^R(t, t') = -i\theta(t - t') \langle [A(t), H'(t)] \rangle_0
\tag{2.94}
$$

as the linear response result

$$
\delta \langle A(t) \rangle = \langle A(t) \rangle - \langle A(t) \rangle_0 = \int_{t_0}^{\infty} dt' C_{AH'}^R(t, t') e^{-\eta(t - t')},
\tag{2.95}
$$

which is referred to as Kubo formula where the exponential factor with infinitesimal small $\eta \rightarrow 0^+$ was added to ensure that a response is suppressed for times $t \gg t_0$ [61].

Fourier transforming leads to

$$
C_{AH'}^R(t, t') = \int_{-\infty}^{\infty} \frac{d\omega}{2\pi} e^{-i\omega t} C_{AH', \omega}^R(t - t')
\tag{2.96}
$$

and thus the corresponding result in the frequency domain

$$
\delta \langle A_\omega \rangle = C_{AH', \omega}^R(\omega) = \int_{-\infty}^{\infty} dt e^{i\omega t} e^{-\eta t} C_{AH', \omega}^R(t).
\tag{2.97}
$$

2.10.2 CONDUCTANCE

The Kubo formula finds useful application for a lot of calculations, as example, the conductance has been chosen here since it will be evaluated using exactly this method in chapter 3.5. The conductance G is according to Ohm's law

$$
I = G \cdot V
\tag{2.98}
$$

the coefficient defining the proportionality between the current I and the applied voltage V and therefore allows for the use of linear response theory. After some algebra, the conductance follows as [61]

$$
G = \lim_{\omega \to 0} \frac{ie^2}{\omega} C_{II}^R(\omega)
\tag{2.99}
$$

with the retarded current-current correlation function which in time domain is given as

$$
C_{II}^R(t - t') = -i\theta(t - t') \langle [\hat{I}(t), \hat{I}(t')] \rangle.
\tag{2.100}
$$

The current operator $\hat{I}(t)$ describes the current flowing through an arbitrarily chosen cross section of the sample at a time t.

The open issue remains to calculate explicitly the value of the correlator. Since it requires evaluation at different times and depends on the time dependent perturbation, one possibility is to employ the Kelydish Green's function approach discussed in section 2.11.

2.11 Keldysh formalism

Widespread use in mesoscopic systems for the description of transport phenomena falls to the Keldysh nonequilibrium Green's function technique. The standard time-ordered zero-temperature single-particle Green's function is given by [76]

$$\mathcal{G}(x,t;x',t') = -\frac{i}{\hbar}\frac{\langle\Psi_0|\mathcal{T}\{\psi_H(x,t)\psi_H^\dagger(x',t')\}|\Psi_0\rangle}{\langle\Psi_0|\Psi_0\rangle} \tag{2.101}$$

with the time ordering operator $\mathcal{T}$, the wavefunctions $\psi_H(x,t)$ being eigenfuntions of the Hamiltonian H and the exact ground state $|\Psi_0\rangle$.

In the interaction picture, which is adopted here, the starting point is given by a Hamiltonian $H = H_0 + V(t)$ where H_0 does not depend on the time and is separated from the time-depending part $V(t)$. Performing a unitary transformation using only the trivial part H_0 [61] leads to both time-dependent states $\hat{\psi}(t)$ and operators $\hat{\mathcal{O}}(t)$ where the states develop with the more intricate interaction part of the Hamiltonian according to

$$\hat{\psi}(t) = U(t)\psi(0) \tag{2.102}$$

with the unitary operator

$$U(t) = e^{iH_0 t}e^{-iHt} \tag{2.103}$$

whereas the operators are only influenced by H_0,

$$\hat{\mathcal{O}}(t) = e^{iH_0 t}\hat{\mathcal{O}}(0)e^{-iH_0 t}. \tag{2.104}$$

In the next step, it is useful to define the S-matrix

$$S(t,t') = U(t)U^\dagger(t') \tag{2.105}$$

with which the wavefunction $\hat{\psi}(t')$ can be transformed to $\hat{\psi}(t)$ as

$$\hat{\psi}(t) = S(t,t')\hat{\psi}(t'). \tag{2.106}$$

One complexity of the definition in equation (2.101) is that the exact ground state $|\Psi_0\rangle$ required for computing the Green's function is actually a result to be obtained using this exact function. In order to circumvent this intricacy, the known non-interacting ground state $|\Phi_0\rangle$ can be used and then connected to the exact one via

$$|\Psi_0\rangle = S(0, -\infty)|\Phi_0\rangle \tag{2.107}$$

leading to [76]

$$\mathcal{G}(x, t; x', t') = -\frac{i}{\hbar} \frac{\langle \Phi_0 | \mathcal{T}\{S(\infty, -\infty)\hat{\psi}(x, t)\hat{\psi}^\dagger(x', t')\}|\Phi_0\rangle}{\langle \Phi_0 | S(\infty, -\infty)|\Phi_0\rangle} \tag{2.108}$$

using $\langle \Psi_0| = \langle \Phi_0 | S(\infty, 0)$ and that the S-matrix conforms to the group property $S(t, t') = S(t, \tau)S(\tau, t')$. Expanding the S-matrix perturbatively in $V(t)$ yields

$$S(\infty, -\infty) = \sum_{n=0}^{\infty} \frac{(-i)^{n+1}}{n!} \int_{-\infty}^{\infty} dt_1...dt_n \mathcal{T}\{V(t_1) \cdot ... \cdot V(t_n)\}. \tag{2.109}$$

Due to the fact that an average potential $V(t)$ contains three to four field operators, terms similar to

$$\langle \Phi_0 | \mathcal{T}\{\hat{\psi}(t)\hat{\psi}^\dagger(t')\hat{\psi}^\dagger(t_1)\hat{\psi}^\dagger(t_2)\hat{\psi}(t_2)\hat{\psi}(t_1)\}|\Phi_0\rangle \tag{2.110}$$

and of higher order need to be evaluated. Using Wick's theorem which states that this can be done by summing over all pairwise contractions the result [76]

$$\mathcal{G}(x, t; x', t') = -\frac{i}{\hbar} \sum_{n=0}^{\infty} (-i)^n \int_{-\infty}^{\infty} dt_1...dt_n \langle \Phi_0 | T\hat{\psi}(x, t)\hat{\psi}^\dagger(x', t')V(t_1) \cdot ... \cdot V(t_n)|\Phi_0\rangle_{conn} \tag{2.111}$$

is obtained after some combinatoric considerations. The sum only considers connected diagrams which are topologically different from each other.

The above results were achieved studying a system in equilibrium. When turning to nonequilibrium, it is possible that the system does not return to the initial starting state even after infinitely long times. Thus, the state at $t = -\infty$ is not necessarily the same as the one at $t = \infty$. The Hamiltonian for the newly considered system is

$$H = h + H'(t), \quad h = H_0 + H_i \tag{2.112}$$

where H_0 is trivial and can be treated using Wick's theorem, H_i contains all many-body aspects, and the rapidly varying time-dependent external perturbation $H'(t)$, for example caused by an electric field, i.e. the nonequilibrium term, is assumed to only be switched on after a time t_0. Going through similar calculations as above, also for this more complicated case, a structurally alike formalism can be obtained.

Due to the inequality between the initial and the final state, it is not advantageous anymore to
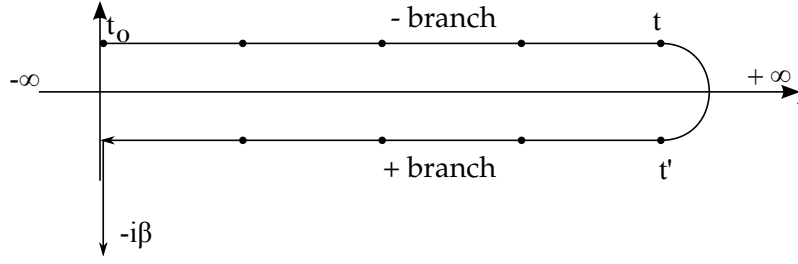
Figure 2.14: Example of a Keldysh contour with positive and negative branches as well as the real and imaginary time axes.

use time-ordering as implemented before using $\mathcal{T}$ but to order along the Keldysh contour. In general, it starts at t_0 but can also be extended to $t_0 \to -\infty$ if initial correlations are not of interest for the regarded problem since this piece of information gets lost doing this. The contour then leads to the point t where the wanted quantity should be evaluated, which is called the forward branch and denoted by $s = -$. It can be extended to ∞ before turning back to build the backward branch $s = +$, which leads again to the starting point t_0 and from there along the imaginary time-axis from 0 to $-i\beta$ where $\beta = 1/k_B T$ is the inverse temperature, see figure 2.14. If the initital contribution from the part from t_0 to $t_0 - i\beta$ is negligible and one thus performs both extensions, the result is a contour with only two branches with the first starting at $-\infty$, going to ∞ called C_1 and the second returning to $-\infty$ called C_2. Hence, the contour-ordered Green's function is composed of four different parts as [76]

$$\mathcal{G}(x,t;x',t') = \begin{cases} \mathcal{G}_c(x,t;x',t') & t,t' \in C_1 \\ \mathcal{G}^>(x,t;x',t') & t \in C_2, t' \in C_1 \\ \mathcal{G}^<(x,t;x',t') & t \in C_1, t' \in C_2 \\ \mathcal{G}_{\tilde{c}}(x,t;x',t') & t,t' \in C_2 \end{cases} \tag{2.113}$$

with the time-ordered Green's function

$$\begin{aligned} \mathcal{G}_c(x,t;x',t') &= -i\langle \mathcal{T}[\psi_H(x,t)\psi_H^\dagger(x',t')]\rangle \\ &= -i\Theta(t-t')\langle \psi_H(x,t)\psi_H^\dagger(x',t')\rangle + \Theta(t'-t)\langle \psi_H^\dagger(x',t')\psi_H(x,t)\rangle, \end{aligned} \tag{2.114}$$

and the antitime-ordered Green's function

$$\begin{aligned} \mathcal{G}_{\tilde{c}}(x,t;x',t') &= -i\langle \tilde{\mathcal{T}}[\psi_H(x,t)\psi_H^\dagger(x',t')]\rangle \\ &= -i\Theta(t'-t)\langle \psi_H(x,t)\psi_H^\dagger(x',t')\rangle + \Theta(t-t')\langle \psi_H^\dagger(x',t')\psi_H(x,t)\rangle, \end{aligned} \tag{2.115}$$

as well as the greater function

$$\mathcal{G}^>(x,t;x',t') = -i\langle \psi_H(x,t)\psi_H^\dagger(x',t')\rangle \tag{2.116}$$

and the lesser function

$$\mathcal{G}^{<}(x,t;x',t') = +i\langle\psi_H^\dagger(x',t')\psi_H(x,t)\rangle.$$

(2.117)

Due to $\mathcal{G}_c + \mathcal{G}_{\tilde{c}} = \mathcal{G}^{<} + \mathcal{G}^{>}$, only three of the above are linearly independent.

With these functions important quantities such as the electron density or the current can be calculated as done in chapter 3.5.

Magnetic graphene waveguide

In this chapter the general setup of a magnetic waveguide in a clean graphene sheet was examined. For this situation a zero-energy flat band as well as finite energy snake states should be present. The questions pursued in the following were whether it is possible to create a dispersion and even conductance due to introducing interactions in and between the levels and if the answer is positive, how the dispersion will look like. This is counter-intuitive from the outset since usually interactions tend to suppress conductance. The entire chapter is based on the publication [77].

This approach could lead to a novel experimental method to probe the existence of electron-electron interactions in clean graphene via transport experiments since there is only a finite conductance in the presence of interactions. Furthermore the peculiar state of the resulting one-dimensional conductor is studied and contrasted to the standard description via the Luttinger liquid theory.

3.1 SETUP

$\mathbb{I}$n contrast to other, conventional methods for building waveguides as described in section 2.4, the confinement of electrons in this construction is realized through the usage of an inhomogeneous magnetic field $\boldsymbol{B} = B(x)\hat{\boldsymbol{e}}_z$ pointing in z-direction, given by

$$B(x) = B\,\mathrm{sgn}(|x| - d/2) \tag{3.1}$$

and shown in figure 3.1. It represents a special case of the magnetic field geometries considered in [63]. This corresponds to a constant positive magnetic field everywhere except in a stripe of width d around $x = 0$ where its direction is turned around while its magnitude stays the same. In the areas of constant magnetic field, i.e. far away from the positions $x = \pm d/2$ where the field is inverted, there are modes that correspond to relativistic Landau levels (depicted here with the classical picture of cyclotron orbits), including also a zero energy mode [7, 9, 78, 79]. Along the lines where the jump occurs, a different kind of modes can be observed. Due to their movement according to the classical picture, they are called snake states. In this classical approach, electrons close to the field changing lines show a circular motion until they reach the point where the sign and their direction of rotation changes, and thus carry out a wave-like movement along the
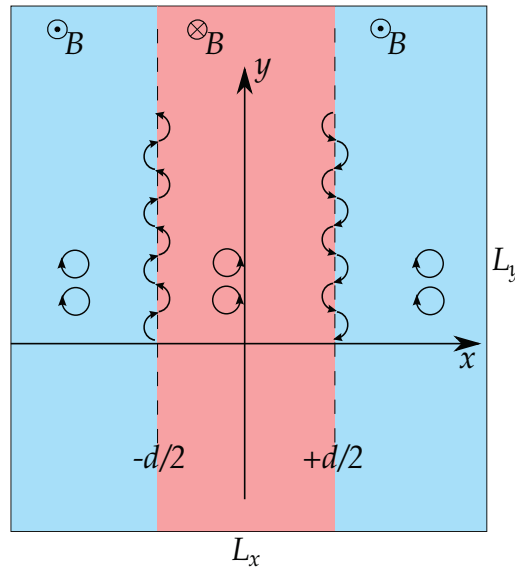
Figure 3.1: Graphene sheet with dimensions L_x and L_y seen from above. Coloured areas correspond to the directions of the magnetic field as also indicated by the symbols referring to in- and out-of-plane; the abrupt changes occur at $x = \pm d/2$. Furthermore depicted are different classical electron orbits that correspond to the $n = 1$ mode: the cyclotron orbits that happen far away from the changing points are an illustration of the Landau levels whereas the wavy lines at the transition between the regions are called snake states. See also [77].

transition line[1]. The different aspects of single-particle spectra for such a magnetic graphene waveguide (MGW) have already been studied [63, 88–91] and experimental evidence for the existence of such modes has already been reported [43–45].

For the given setup the counterpropagating snake modes [63, 88, 92–94] are well separated and thus a quantized conductance will be found for non-zero energy bands [89], but still the question arises whether there will be a conductance for the zero-energy modes and how it will look like. It is worth noting that although this specific magnetic field profile is kept throughout the calculation to present determined results, a similar outcome is anticipated for different profiles [63]. Therefore it is not indispensable to experimentally realize atomically sharp magnetic field changes as considered here theoretically.

Furthermore, the real magnetic field could also be replaced by strain-induced so-called pseudo-magnetic fields [95, 96], or, allowing some small modifications, the surface states found on three-dimensional topological insulators [97, 98] could be used to investigate a similar situation.

3.2 Single-particle model

$\mathcal{C}$lose to the point of neutrality in graphene, the electrons behave as two-dimensional massless Dirac fermions [6, 99] and thus the low-energy physics in this system are well described by these low-energy quasiparticles. For the applied magnetic field in equation (3.1) the single-particle description [63, 88] can be carried out utilizing the single-particle Hamiltonian

$$H_0 = v_F \boldsymbol{\sigma} \cdot \left(-i\boldsymbol{\nabla} + \frac{e}{c}\boldsymbol{A} \right) - e\Phi \tag{3.2}$$

where the last term vanishes since there is only a magnetic and no electric field present. The quantity $v_F \approx 10^6$ m/s is the Fermi velocity in graphene, $\boldsymbol{\sigma} = (\sigma_x, \sigma_y)$ consists of the 2×2 Pauli matrices, $\boldsymbol{\nabla} = (\partial_x, \partial_y)$ contains the partial derivatives and arises from substituting the momentum $\boldsymbol{p}$. The vector potential $\boldsymbol{A}$ entails the magnetic field, can be derived from the relation $\boldsymbol{B} = \boldsymbol{\nabla} \times \boldsymbol{A}$ and follows as

$$\boldsymbol{A} = A(x)\hat{\boldsymbol{e}}_y, \quad A(x) = B \times \begin{cases} x + d & x < -d/2 \\ -x, & |x| < d/2, \\ x - d, & x > d/2 \end{cases} \tag{3.3}$$

if one uses the Landau gauge. This choice ensures that the problem is homogeneous in the y-direction, thus $k_y = k$ is a good quantum number and classifies the eigenstate for every band

---

[1]Concepts of how to use inhomogeneous magnetic fields like this to direct Dirac fermions have been studied before [80–87].

index n.

Hence, the Hamiltonian is thoroughly defined and can be exploited to solve the Dirac equation

$$H_0\Psi_{n,k} = E_{n,k}\Psi_{n,k}, \tag{3.4}$$

with the eigenenergies $E_{n,k}$ and the spinor eigenstates $\Psi_{n,k}(x,y)$ belonging to these energies. Those quantities are labelled via the indices n (band-index) and k (the already mentioned conserved momentum along the y-axis). Due to this conservation, the x- and y-dependent parts can be separated and thus the wave functions can be written as

$$\Psi_{n,k}(x,y) = \frac{e^{iky}}{\sqrt{L_y}}\psi_{n,k}(x), \quad \psi_{n,k}(x) = \begin{pmatrix} \phi_{n,k}(x) \\ i\chi_{n,k}(x) \end{pmatrix} \tag{3.5}$$

where the spinor components $\phi_{n,k}(x)$ and $\chi_{n,k}(x)$, which refer to the two sublattices in graphene, still include a normalization constant with the condition $\int dx(\phi_{n,k}^2 + \chi_{n,k}^2) = 1$, while the y-dependent part reduces to simple plane waves.

The eigenfunctions obey moreover the following symmetry relations (ψ^* denotes the complex conjugate of ψ):

$$\begin{aligned} \psi_{n,k}(x) &= \sigma_z\psi_{-n,k}(x) \quad (n \neq 0), \tag{3.6} \\ \psi_{n,k}(x) &= (-1)^{n+1}\psi_{n,-k}^*(-x). \end{aligned}$$

The first one presents a connection of states with opposite band index via a particle-hole transformation, which implies a mirror-symmetry of the energy spectrum (i.e. $E_{-n,k} = -E_{n,k}$) in the single-particle picture, whereas the second is a result of the combination of the one-dimensional node rule and inversion symmetry.

3.2.1 General finite energy wave functions

Inserting the Hamiltonian (3.2) into equation (3.4) and solving the resulting differential equations, as it has also been done in [63, 100], yields solutions for the wave functions. The calculation shall be briefly sketched in the following.

The differential equations can be easily expressed as

$$\begin{aligned} (\partial_x^2 - V_+ + E^2)\phi_{k,n} &= 0 \tag{3.7} \\ (\partial_x^2 - V_- + E^2)\chi_{k,n} &= 0 \end{aligned}$$

where the dependencies of the different spinor components have been separated from one another, dimensionless units have been introduced (lengths are measured in units of the magnetic length $l_b = \sqrt{\hbar c/eB_0}$ whereas the vector potential is expressed in $l_B B_0$, the energy in $E_B = \hbar v_F/l_b$

and the wave vector k is given in units of the inverse magnetic length, i.e. l_b^{-1}), and the new quantity $V_\pm = \pm\partial_x A(x) + (k + A(x))^2$ has been adopted to shorten the notation.

For the three different areas of the magnetic field (which have a different vector potential A, respectively), one can always find substitutions for the parameters, such that the result is the differential equation

$$\left(\frac{d^2}{dq^2} + p + \frac{1}{2} - \frac{q^2}{4}\right)\phi = 0 \tag{3.8}$$

for one of the spinor components. Two linear independent solutions of this equation are given by the parabolic cylinder functions $D_p(q)$ and $D_p(-q)$ [101, 102] and while for the two outer regions only the normalizable solution survives, i.e. the one that goes to zero for $x \to \pm\infty$, respectively, a linear combination of both is kept for the central region $|x| < d/2$.

The second spinor component is obtained via recursion formulas [101]

$$\left(\frac{d}{dq} - \frac{q}{2}\right) D_p(q) = -D_{p+1}(q)$$

$$\frac{d}{dq}D_p(q) + \frac{q}{2}D_p(q) - pD_{p-1}(q) = 0 \tag{3.9}$$

and hence, inserting the different q and p, the general wave equations follow as (compare [77, 100])

$$\psi_{n,k;I}(x) = C_I^{(n,k)}\begin{pmatrix} D_{-1+E^2/2}\left(-\sqrt{2}(x + k + d)\right) \\ -\frac{i\sqrt{2}}{E}D_{E^2/2}\left(-\sqrt{2}(x + k + d)\right) \end{pmatrix}, \tag{3.10}$$

for the first region where $x < -d/2$,

$$\psi_{n,k;II}(x) = \sum_\pm C_{\pm,II}^{(n,k)}\begin{pmatrix} D_{E^2/2}\left(\pm\sqrt{2}(x - k)\right) \\ \mp\frac{iE}{\sqrt{2}}D_{-1+E^2/2}\left(\pm\sqrt{2}(x - k)\right) \end{pmatrix}, \tag{3.11}$$

in the middle region with $|x| < d/2$ and for the last region, i.e. $x > d/2$ it reads

$$\psi_{n,k;III}(x) = C_{III}^{(n,k)}\begin{pmatrix} D_{-1+E^2/2}\left(\sqrt{2}(x + k - d)\right) \\ \frac{i\sqrt{2}}{E}D_{E^2/2}\left(\sqrt{2}(x + k - d)\right) \end{pmatrix}. \tag{3.12}$$

The quantities $C_i^{(n,k)}$ are in general complex coefficients and all the energies $E = E_{n,k}$ have to be found for each band index n and disperse with k.

In order to further investigate the properties of these coefficients and the wave functions in total, it is useful to restart again with the non-interacting Hamiltonian, which, for the given case, can be shortened and for each k expressed as [77]

$$H_0^{(k)} = -i\sigma_x\partial_x + [k + A(x)]\sigma_y. \tag{3.13}$$

Under inversion with respect to x, here denoted as $\mathcal{R}_x : x \to -x$, $A(x)$ is antisymmetric and thus the entire Hamiltonian is symmetric under the inversion

$$\left[H_0^{(k)}, \Xi\right]_- = 0, \quad \Xi = \mathcal{R}_k \mathcal{R}_x \mathcal{C}, \tag{3.14}$$

where $\mathcal{C}$ is the notation for complex conjugation and $\mathcal{R}_k$ is defined analogously to $\mathcal{R}_x$. Applying the operator Ξ, whose eigenvalues are given by $\xi = \pm$, to the wave functions, one obtains

$$\Xi\psi_{n,k}(x) = \psi_{n,-k}^*(-x) = \pm\psi_{n,k}(x). \tag{3.15}$$

From this relation also symmetry conditions for the coefficients follow, namely

$$C_I^{(n,k)} = \xi\left(C_{III}^{(n,-k)}\right)^*, \quad C_{\pm,II}^{(n,k)} = \xi\left(C_{\mp,II}^{(n,-k)}\right)^*. \tag{3.16}$$

For convenience the coefficients are assigned real values by choosing the overall phase accordingly. Consequently also the spinor components ϕ and χ can be chosen real valued.

From the matching conditions $\psi_{n,k;I}(-d/2) = \psi_{n,k;II}(-d/2)$ and $\psi_{n,k;II}(d/2) = \psi_{n,k;III}(d/2)$ that apply for the wave functions since they have to be continuous at the meeting of the three regions, and the expressions for the wave functions (3.10) - (3.12), a system of equations is obtained. It can be rewritten as a matrix-vector-multiplication and reads

$$\boldsymbol{M}_{n,k}(E) \cdot \boldsymbol{C}_{n,k} = 0 \tag{3.17}$$

where the vector $\boldsymbol{C}_{n,k} = \left(C_I^{(n,k)}, C_{+,II}^{(n,k)}, C_{-,II}^{(n,k)}, C_{III}^{(n,k)}\right)^T$ encodes all the coefficients.

3.2.2 THE DISPERSION RELATION

The 4×4 matrix $\boldsymbol{M}_{n,k}(E)$ however contains the parabolic cylinder functions obtained from the matching conditions and thus depends non-trivially on the eigenenergies $E = E_{n,k}$. Therefore a numerical root-finding method has to be used to find the solutions of the condition

$$\det \boldsymbol{M}_{n,k}(E) = 0 \tag{3.18}$$

from which the energies should be obtained. In this case the bisection method was selected since it is a rather simple algorithm that doesn't for example require the analytical derivative.

For this method in general an interval $[a, b]$ is chosen, on which the function $f(x)$, whose root with respect to x is wanted, is continuous. In the next step the values $\text{sgn}(f(a))$ and $\text{sgn}(f(b))$ are compared because there is a single root $f(x_0) = 0$ with $x_0 \in [a, b]$ only if the signs are different, i.e. $\text{sgn}(f(a)) \neq \text{sgn}(f(b))$. If this is the case, a value exactly in the middle of this interval is calculated, namely $c = (a + b)/2$, and then again the signs are compared and for the next step the interval $[a, c]$ or $[c, b]$ is chosen, depending on where the root is located [103]. This scheme is
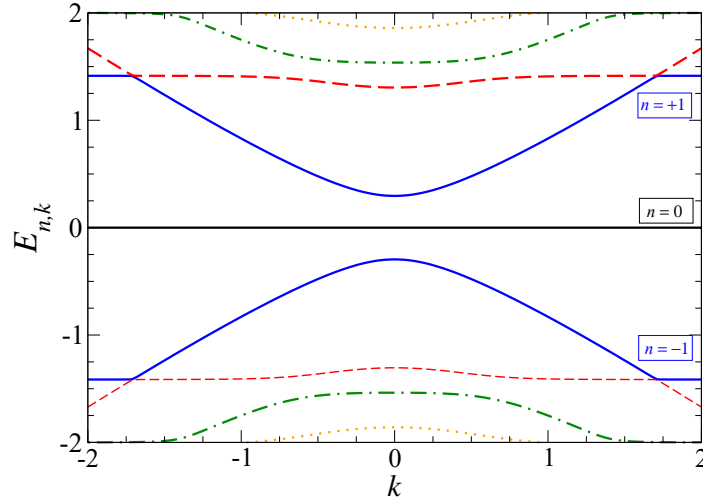
Figure 3.2: Dispersion relation of the non-zero energy modes gained via a numerical root-finding method for a value $d = 2l_B$. Energies $E_{n,k}$ are given in units of the magnetic energy E_B and the momentum is measured in the inverse magnetic length l_B^{-1}. The energy bands $n = 0, \pm 1$ will be of special importance and there is an avoided crossing present between the $n = \pm 1$ and $n = \pm 2$ bands that is not visible without zooming in. See [63, 77].

iterated until the function value is sufficiently small or the interval is extremely small and the value for the root is stored.

In this manner the dispersion relation in figure 3.2 was obtained. Furthermore, equation (3.17) also yields the relations between the coefficients $C_j^{(n,k)}$ for the different n- and k-values and $j \in 1, 2, 3$. Hence, while the first coefficient is received from the normalization condition, the others follow from these relations and thus the wave functions are finally fully acquired numerically.

3.2.3 DEPENDENCE ON WAVEGUIDE WIDTH

As visible in the outer regions of figure 3.2, the dispersion becomes flat for large $|k|$-values and assumes the characteristic values $E_{n,k}^{(d=0)} = \mathrm{sgn}(n)\sqrt{2|n|}$ of the relativistic and k-independent Landau levels [6, 7, 9, 78, 79] that are also obtained for the case of a vanishing waveguide $d = 0$. The reason for this behaviour is easily found: For large $|k|$ the system is in a state where a nearly constant magnetic field is present since one is far away from the waveguide region.

But apart from this also another dependence on the waveguide width d can be observed. If the eigenvalue problem from equation (3.18) is solved for different d, the energy of the gap between the $n = 1$ and the zero mode $n = 0$ can be plotted versus this parameter and thus the figure 3.3 is acquired.
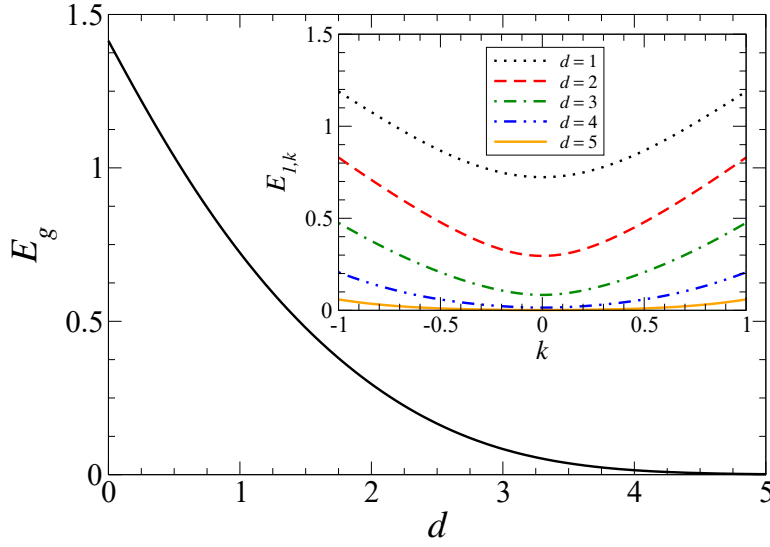
Figure 3.3: The main panel shows the dependence of the energy gap E_G, which is the difference between the minimum energy of the first band and the zero-energy band, on the width of the waveguide d. In the inset the first energy level with $n = 1$ is depicted for the small k-region to see its behaviour. [77]

It is visible that this energy gap decays with the width d. Therefore only a certain width can be considered and here $d \lesssim 2l_B$ is chosen since for bigger d the single-particle gap is no longer large compared to the Coulomb energy scale typical in this system. Therefore, the implemented approach of a perturbation treatment would break down.

Nevertheless, it is still valuable to consider the limit $d \to \infty$ where the gap energy so rapidly decays: Regarding the case of infinite d, it becomes obvious that the result is the opposite from the situation with $d = 0$. Whereas for vanishing d the waveguide disappears and one is left with a constant positive magnetic field B in z-direction, with increasing d the central region of the waveguide becomes larger and finally there exists only a constant negative magnetic field with strength $-B$. Therefore, as a result from increasing d, the magnetic field in the bulk is reversed as $B\hat{\boldsymbol{e}}_z \to -B\hat{\boldsymbol{e}}_z$ and thus also the bulk eigenstates change from the well-known standard Landau levels to shifted Landau levels with a modified index $\tilde{n} \in \mathbb{Z}$ in the time-reversed system,

$$\psi_{\tilde{n},k}(x) = \frac{1}{\sqrt{1 + \text{sgn}(|\tilde{n}|)}} \begin{pmatrix} \varphi_{|\tilde{n}|}(x + k) \\ i \, \text{sgn}(\tilde{n}) \varphi_{|\tilde{n}-1|}(x + k) \end{pmatrix}. \tag{3.19}$$

Here the sign-function is defined as $\text{sgn}(n) = (1, 0, -1)$ for $(n > 0, n = 0, n < 0)$ and the normalized eigenstates of the one-dimensional harmonic oscillator are represented by φ_n.

In the inset of figure 3.3 the behaviour of the $n = 1$ level is depicted. For increasing d it flattens and approaches zero energy and ultimately it combines with the $n = -1$ level, which behaves

analogously due to the mirror symmetry in the energy, to form the new zero mode. Simultaneously the avoided crossing of the $n = \pm 1$ and $n = \pm 2$ levels shift to higher $|k|$ values.

The newly built zeroth Landau level, that arises from the merging described before, only has an upper spinor component while the original zero mode for finite d only has a lower component as will be derived later. From the parabolic cylinder functions for this case one obtains

$$\psi_{n,k}(x) \rightarrow \pi^{-1/4} e^{-(x-k)^2/2} \begin{pmatrix} 1 \\ 0 \end{pmatrix}, \quad E \rightarrow 0. \tag{3.20}$$

3.2.4 Zero-mode wave functions

Starting from the condition $E_{n=0,k} = 0$ for the zero modes and solving again equation (3.4), one ends up with a different result [77, 100].

For this situation, i.e. $E_{0,k} = 0$ the differential equations (3.7) reduce to

$$[\partial_x - k - A(x)] \phi_{k,0} = 0 \tag{3.21}$$
$$[\partial_x + k + A(x)] \chi_{k,0} = 0.$$

Evaluating this, choosing the non-divergent solution and applying the matching conditions at $x = \pm d/2$ one finds that the zero-mode wave functions only have a lower spinor component which is non-zero – in contrast to the $d \rightarrow \infty$ limit where the ground state only had an upper component that did not vanish. They read

$$\psi_{0,k}(x) = \begin{pmatrix} 0 \\ i\chi_{0,k}(x) \end{pmatrix} \quad \text{with} \tag{3.22}$$

$$\chi_{0,k}(x) = \frac{e^{d|x|-(x+k)^2/2}}{N_{0,k}} \times \begin{cases} 1, & |x| > d/2, \\ e^{(|x|-d/2)^2}, & |x| < d/2, \end{cases}$$

where $N_{0,k}$ is a normalization constant. It can be rewritten as $N_{0,k} = \sqrt{Y(k)}$ with the auxiliary function

$$Y(z) = \sum_{\pm} \left(e^{(z \mp d)^2} \text{erfc} \left(\pm [z \mp d/2] \right) \pm i e^{-z^2 + d^2/2} \text{erfc} \left(-i[z \mp d/2] \right) \right), \tag{3.23}$$

which contains the complementary error function $\text{erfc}(z)$ [101, 102] and is in principle complex-valued but gives positive real values for real-valued arguments like k in this case.

It is obvious that the zero mode has a much simpler mathematical form since its main contribution originates from exponential functions and not from parabolic cylinder functions as the general result. Therefore, the zero-energy modes will be treated separately first before including the interactions with other modes.

For a finite-size waveguide the following properties of the probability density distribution

$|\psi_{0,k}(x)|^2$ are fulfilled: For $|k| < d/2l_B^2$ there is a local minimum in the probability density at $x = kl_B^2$ whereas local maxima exist for $|k| \lesssim d/l_B^2$ in the vicinity but not inside the waveguide region.

For $d = 0$ on the other hand, the zero mode describes the $n = 0$ Landau level in the resulting constant magnetic field and thus the function $\chi_{0,k}$ mathematically reduces to ground-state wave-functions of the harmonic oscillator shifted by an offset.

In combination with the observation that the snake states, especially the ones with band index $n = \pm 1$, develop a probability density maximum around the sign-changing points of the magnetic field, i.e. for $x = \pm d/2$, the only interaction-induced transitions between zero and non-zero bands that will be of importance in the later calculations occur under the condition $|k| \lesssim d/l_B^2$.

3.3 Including interactions

When we consider the situation of a partially filled $n = 0$ level and subsequently filled lower and empty upper bands, no conductance can arise without including interaction effects. Therefore in this chapter we include the Coulomb interactions in a second-quantized notation via the interaction Hamiltonian

$$\hat{H}_I = \frac{1}{2} \int d\boldsymbol{r} d\boldsymbol{r}' \, V(\boldsymbol{r} - \boldsymbol{r}') \hat{\Psi}^\dagger(\boldsymbol{r}) \hat{\Psi}^\dagger(\boldsymbol{r}') \hat{\Psi}(\boldsymbol{r}') \hat{\Psi}(\boldsymbol{r}) \tag{3.24}$$

where the fermionic annihilation (creation) field operators are given by

$$\hat{\Psi}^{(\dagger)}(\boldsymbol{r}) = \sum_{n,k} \Psi_{n,k}^{(*)}(\boldsymbol{r}) \, c_{n,k}^{(\dagger)}. \tag{3.25}$$

They act at the position $\boldsymbol{r} = (x, y)$, include the wave functions defined in equation (3.5) and the fermionic operators, which obey the anticommutator algebra $\{c_{n,k}, c_{n',k'}^\dagger\} = \delta_{nn'}\delta_{kk'}$ and $\{c_{n,k}, c_{n',k'}\} = 0 = \{c_{n,k}^\dagger, c_{n',k'}^\dagger\}$.

The potential in the Hamiltonian is a Coulomb potential modified by a screening gate in the distance R from the graphene plane, which results in an additional image charge term, and reads

$$V(\boldsymbol{r}) = \alpha \left(\frac{1}{|\boldsymbol{r}|} - \frac{1}{\sqrt{|\boldsymbol{r}|^2 + 4R^2}} \right). \tag{3.26}$$

The fine structure constant α in graphene takes values that depend on the dielectric features of its environment [6, 99] and lie in the range $\alpha \approx 0.1$ to 2.

Performing a Fourier transform to momentum space, the Hamiltonian yields

$$\hat{H}_I = \frac{1}{2} \sum_{n_1,n_2,n_3,n_4} \sum_{k,k',q} V_{k,k';q}^{(n_1,n_2,n_3,n_4)} c_{n_1,k}^\dagger c_{n_2,k'}^\dagger c_{n_3,k'-q} c_{n_4,k+q} \tag{3.27}$$
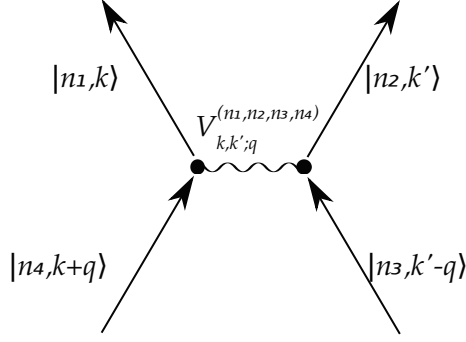
Figure 3.4: The Feynman diagram for the Coulomb interaction with interaction strength $V_{k,k';q}^{(n_1,n_2,n_3,n_4)}$ is depicted with the incoming particles that are annihilated in bands n_3 and n_4 with respective wave vectors $k' - q$ and $k + q$, as well as the outgoing electrons. These are created in the bands n_1 and n_2 with the momenta k and k'.

and can be visualized as in the Feynman diagram in figure 3.4. It includes the Coulomb matrix elements

$$V_{k,k';q}^{(\{n_j\})} = \frac{1}{L_y} \int \frac{dk_x}{2\pi} \tilde{V}(k_x, q) \mathcal{F}_{k,q}^{(n_1,n_4)}(k_x) \mathcal{F}_{k',-q}^{(n_2,n_3)}(-k_x), \tag{3.28}$$

which again are built using the the Fourier transform of the Coulomb potential from equation (3.26), which reads

$$\tilde{V}(k_x, k) = 2\pi\alpha \frac{1 - e^{-2R\sqrt{k_x^2+k^2}}}{\sqrt{k_x^2 + k^2}}, \tag{3.29}$$

and the form factors

$$\mathcal{F}_{k,q}^{(n,n')}(k_x) = \int dx \, e^{-ik_x x} \psi_{n,k}^\dagger(x) \cdot \psi_{n',k+q}(x). \tag{3.30}$$

For the numerical evaluation described later it is convenient to exploit the symmetry relations

$$\begin{aligned}
\mathcal{F}_{k,q}^{(0,n)}(k_x) &= -\mathcal{F}_{k,q}^{(0,-n)}(k_x), \\
\mathcal{F}_{k,q}^{(n,n')}(k_x) &= \mathcal{F}_{k,q}^{(-n,-n')}(k_x), \\
\mathcal{F}_{k,q}^{(n,n')}(k_x) &= \mathcal{F}_{k+q,-q}^{(n',n)}(k_x), \\
\mathcal{F}_{k,q}^{(n,n')}(k_x) &= (-1)^{n+n'} \mathcal{F}_{-k,-q}^{(n,n')}(-k_x)
\end{aligned} \tag{3.31}$$

in order to save computation time and memory. The first and second of the relations in equation (3.31) exclusively hold for $n \neq 0$ and $n' \neq 0$. Another useful property, namely the behaviour under complex conjugation,

$$\mathcal{F}_{k,q}^{(n,n')}(k_x) = \left(\mathcal{F}_{k,q}^{(n,n')}(-k_x) \right)^*, \tag{3.32}$$

is the cause of real-valued Coulomb matrix elements. Furthermore they also obey a number of handy symmetry relations:

$$
\begin{aligned}
V_{k,k';q}^{(n_1,n_2,n_3,n_4)} &= V_{k',k;-q}^{(n_2,n_1,n_4,n_3)} \\
&= V_{k+q,k'-q;-q}^{(n_4,n_3,n_2,n_1)} \\
&= (-1)^{n_1+n_2+n_3+n_4} V_{-k,-k';-q}^{(n_1,n_2,n_3,n_4)}.
\end{aligned}
\tag{3.33}
$$

An analytical expression for the result of the form factors is only possible for the zero modes and yields

$$
\mathcal{F}_{k,q}^{(0,0)}(k_x) = \frac{Y\left(k + \frac{q+ik_x}{2}\right)}{\sqrt{Y(k)Y(k+q)}}
\tag{3.34}
$$

with the auxiliary function $Y(z)$ already defined in equation (3.23).

For the general case of non-zero energy however, the x-integral in equation (3.30) has to be carried out numerically for all combinations of k, q and k_x that remain necessary after making use of the symmetry relations (3.31). To implement the integration, a numerical variant of the Riemann integral has been used, which estimates the value of the integral along a curve with the sum of the area of all rectangles, created by multiplying the distance of two points in the discrete grid on the x-axis with the value of the function $f(x)$. Thereafter the needed Coulomb matrix elements can – under consideration of their symmetry relations (3.28) and the fact that not all elements will influence the resulting conductance in the end – be calculated numerically by evaluating the k_x-integration. Additional checks of the quality of the numerical integrations have been made, testing the convergence by changing the number of discrete points as well as the integration limits since it is not possible to reach $\pm\infty$ numerically.

For a shortened notation the quantity

$$
W_{k,k';q}^{(n_1,n_2,n_3,n_4)} = \frac{1}{2}\left(V_{k,k';q}^{(n_1,n_2,n_3,n_4)} - V_{k',k;q+k-k'}^{(n_2,n_1,n_3,n_4)} \right)
\tag{3.35}
$$

is introduced. It is obtained via an antisymmetrization, which echoes the anticommutator algebra of the fermions, regarding the exchange of (n_1, k) and (n_2, k') from the Coulomb matrix elements.

3.4 Hartree-Fock treatment of the zero mode

First of all, the zero mode sector alone is regarded and therefore no virtual interband transitions, i.e. interaction processes with $n \neq 0$ bands are allowed. We consider the already mentioned situation of a zero mode that is partially filled with all upper bands ($n > 0$) empty and all bands with negative energy ($n < 0$) fully occupied and define the zero mode filling via the filling factor $\nu = N/N_s$. This is a valid assumption unless the typical scale of the Coulomb
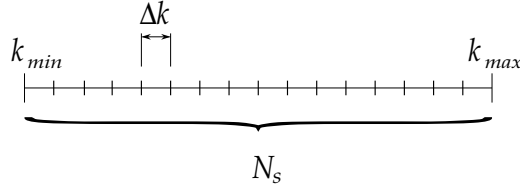
Figure 3.5: The discrete grid of the N_s states in the first Brillouin zone of the k-space with $k_{min} < k < k_{max}$ and spacing Δk is shown.

energy reaches the order of the single-particle energy gap E_g. The degree of degeneracy and also the number of available k-states in the Brillouin zone

$$N_s = \frac{(L_x - 2d)L_y}{2\pi l_B^2} \tag{3.36}$$

can be achieved for the case of a rectangular sample with the lengths L_x and L_y, as shown in figure 3.1, and is identical to the total magnetic flux expressed in units of the magnetic flux quantum. The k-states are numbered by the index n_y in the boundaries $-N_s/2 < n_y < N_s/2$ and thus assumes the values $k = 2\pi n_y/L_y$. This discrete grid is illustrated in figure 3.5.

The Hamiltonian for the considered system is given via the interaction Hamiltonian in equation (3.27) since for the zero mode the kinetic energy term vanishes. Due to the fact that only intraband interaction processes are permitted, all $n_j = 0$ for $j = 1, ..., 4$ and furthermore the analytic expressions (3.34) for the form factors can be employed. Nevertheless, it is impossible already for this reduced situation to find numerically exact or even analytical solutions for system sizes that are not very small.

Hence, here the standard Hartree-Fock theory (see section 2.7.2), that can be found in many textbooks [61, 104], is used to gain results that are not expected to differ qualitatively from the exact solutions. Also for the homogeneous magnetic field, which in our language means there is no magnetic waveguide for $d \to 0$, insight in the physics apart from the fractional quantum Hall regime and the connected rational filling factors is gained via HF approximations [6, 99, 105–110]. With the Coulomb matrix elements defined in the section before, the HF potential can be written as

$$W_{k,k'} = 2W_{k,k';q=0}^{(0,0,0,0)} = V_{k,k';0}^{(0,0,0,0)} - V_{k',k;k-k'}^{(0,0,0,0)} \tag{3.37}$$

where the definition of the antisymmetrized Coulomb matrix elements (3.35) has been used. The first term represents the direct interaction (Hartree term) with exchange momentum $q = 0$ whereas the second expression comes from the exchange interaction (Fock term) with $q = k - k'$. With this quantity the single-particle energies can be computed as

$$\varepsilon_k = \sum_{k'} W_{k,k'} n_{k'} \tag{3.38}$$

employing the self-consistently determined occupation number

$$n_k = \left\langle c_{0,k}^\dagger c_{0,k} \right\rangle, \tag{3.39}$$

which is also the HF order parameter at the same time[2]. Taking its expectation value has to be performed with respect to the zero-mode Hamiltonian in the HF approximation. Furthermore, the HF parameter has to fulfil the condition $\sum_k n_k = N = \nu N_s$ for a given filling factor ν.

In the beginning of the HF iteration a normalized and randomly chosen initial distribution of the occupation number is found and symmetrized according to $n_{-k} = n_k$, assuming even numbers for N and N_s. In the following step the HF single-particle energies are calculated as described in equation (3.38). Because of the symmetry relations of the Coulomb matrix elements in (3.33) also these energies are symmetric, $\varepsilon_{-k} = \varepsilon_k$. According to this energy distribution, the N states with lowest energy are occupied and thus the occupation distribution n_k is updated. This procedure is repeated until the iteration reaches convergence. The ground-state energy in the HF approximation is given as

$$\mathcal{E}_0^{\mathrm{HF}} = \frac{1}{2} \sum_k \varepsilon_k n_k \tag{3.40}$$

and can be utilized to check this convergence. While for most initial configurations the HF energy quickly converges to a minimum, there is a number of local energy minima and therefore it depends on the initial state where the iteration ends and which energy it results in. The global minimum is found numerically by comparing the converged results of a few hundred different random initial distributions. These results are reliable since all computed quantities, like for example the Fermi momentum or the ground-state energy itself, behave smoothly when parameters are varied.

The resulting single-particle energies of the converged iteration are shown in figure 3.6 for different filling factors ν. These values, as well as those shown in figure 3.7, are obtained for a fine structure constant $\alpha = \alpha_0 = 0.5$. To take the step from these results to the ones corresponding to other values $\alpha \neq \alpha_0$ an easy scaling of the important quantities is sufficient. With this the changed variables for arbitrary α follow as $\varepsilon_k^{(\alpha)} = (\alpha/\alpha_0)\varepsilon_k^{(\alpha_0)}$ and as a consequence also $v^{(\alpha)} = (\alpha/\alpha_0)v^{(\alpha_0)}$ whereas the Fermi momentum k_F exhibits no dependence on α.

Regarding the behaviour of the HF dispersion of the zero mode, one can see a lot of structure, but the prominent features for all filling factors are the dips for small wave vectors k around the origin as well as for large momenta. While the previously mentioned are what was expected, namely states located in the region of the waveguide with momenta $|k| < d/l_B^2$, the later are more puzzling since originally one would expect flat behaviour of the dispersion for large $|k|$. The existence of these profound energy minima, that lie below the chemical potential and therefore represent occupied states, corresponds to spatially localized states, so-called "Pauli holes", in the

---

[2]Due to this choice of the HF order parameter other scenarios as for example charge density wave ordering or Wigner crystal formation, that has already been observed for a homogeneous magnetic field and some filling factors ν [104, 107–109], are neglected. In contrast to the unscreened situation ($R \to \infty$) however, an externally gate screened MGW is considered and thus phases like that are not anticipated to occur.

(a)

(b)

(c)

(d)
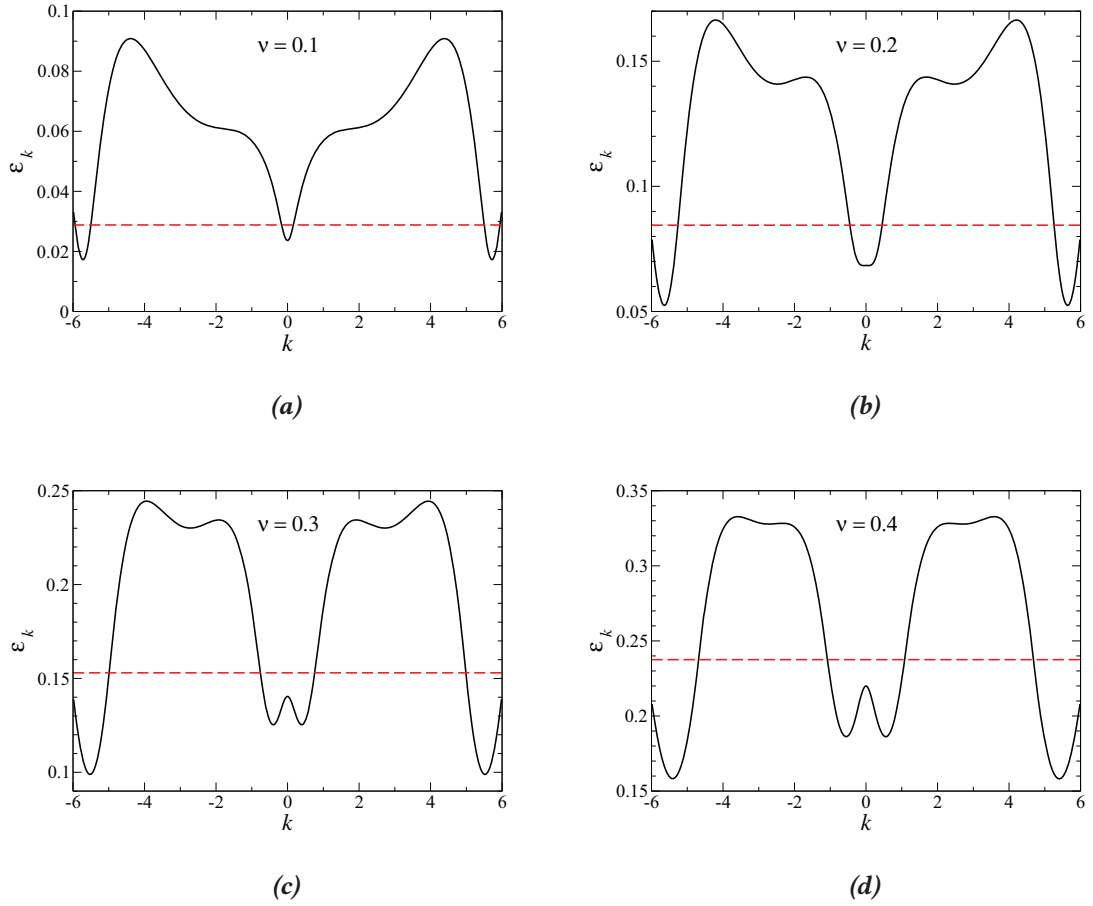
Figure 3.6: Zero-mode HF energies, self-consistently determined for different filling factors ν, plotted versus wave vector k. Energies are given in units of E_B, momenta in l_B^{-1}. Calculations are made for the following parameters: Wave guide width $d = 2l_B$, fine structure constant $\alpha = 0.5$, number of available states $N_s = 400$, system dimensions $L_x = 16l_B$ and thus resulting $L_y = 209.4l_B$ and the zone boundary $k_{max} = \pi N_s/Ly = 6l_B^{-1}$, as well as the distance to the screening gate $R = d$. [77]

vicinity of the boundaries of the sample $x = \pm L_x/2$.

Despite the fact that these boundary states do not affect the resulting conductance due to the small interaction elements with the higher bands for these large k values - in fact for the numerical evaluation only states below a certain cutoff with $|k| \leq k_C \approx d/l_B^2$ are kept - it is nevertheless interesting to further investigate the occurrence of these states. In order to tackle this inquiry a look at the case of a homogeneous magnetic field ($d \to 0$) is helpful. For this limit, the auxiliary function $Y(z)$ defined in equation (3.23) simplifies to the expression $Y(z) \to 2e^{z^2}$. As a consequence also the form factors take the shorter and simpler form $\mathcal{F}_{k,q}^{(0,0)}(k_x) \to e^{-(k_x^2+q^2)/4}e^{i(k+q/2)k_x}$ and combining this, the zero-mode Coulomb matrix elements for $d \to 0$ read

$$V_{k,k';q}^{(0,0,0,0)}\Big|_{d\to 0} \to \frac{2\alpha}{L_y}\Big[K_0\left(|q(k-k'+q)|\right) - K_0\left(|q|\sqrt{4R^2+(k-k'+q)^2}\right)\Big] \qquad (3.41)$$

where K_0 is the modified Bessel function [101]. With these ingredients and the simple assumption of an equal and k-independent occupation distribution $n_k = \nu$, the HF zero-mode energies defined in equation (3.38) follow as

$$\varepsilon_k \simeq \frac{\nu L_y}{2\pi}\int_{-L_x/2}^{L_x/2} dk' W_{k,k'}. \qquad (3.42)$$

Substituting the variable of integration k' such that it absorbs k leads to energies ε_k that are independent of k. Already with this simplified model in the $d \to 0$ limit, however, one finds that states which are localized near the margin of the sample exhibit a similar dispersion.

Furthermore, the dependence of the dispersion on the filling factor ν is an interesting feature: There is always a minimum around the position $k = 0$ in the dispersion although for small fillings of $\nu \lesssim 0.08$ the dip becomes so shallow that it doesn't cross the Fermi energy and thus no occupation for these states happens. For the larger fillings shown in figure 3.6, it is obvious that this minimum crosses the dotted line that marks the Fermi level and for further increase of ν it splits into two minima symmetrical around $k = 0$. This behaviour can be explained with a look at the already mentioned minima in the probability density $|\psi_{0,k}(x)|^2$ which occur for $x = kl_B^2$ under the condition $|k| < d/2l_B^2$ since due to the lowered Coulomb repulsion the split minima are thus energetically favourable.

Only the depicted regime for the filling factor, $0.1 \lesssim \nu \lesssim 0.4$, will be kept in the following for evaluation since there are no occupied states in the waveguide region for lower ν and for higher fillings of about $\nu \gtrsim 0.5$ the danger arises that the HF energy surpasses the energy gap. For this case, i.e. when $\varepsilon_k > E_g$, the underlying assumption of bands that are separated, is not valid any longer. Therefore, the perturbation method applied here is only reasonable in the filling factor window noted above.

The positions in k-space where the energy band ε_k crosses the Fermi energy are identified as Fermi momenta $k = \pm k_F$ and shown in figure 3.7(a). It is visible that the dependence of the effective Fermi momentum k_F on the filling factor ν is well described as linear and, for the regarded fillings, stays below the waveguide width, $k_F \lesssim d$. Linearising the spectrum around these k_F-points and taking the numerical derivative, one finds an approximation of the effective
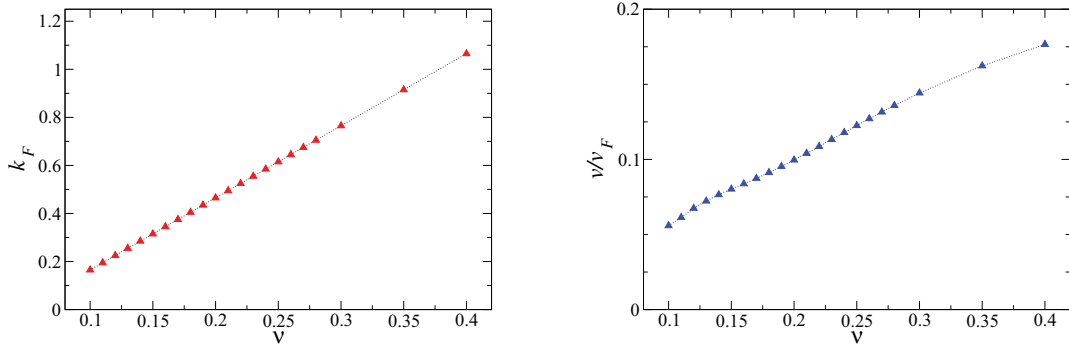
(a) Fermi momentum k_F versus filling factor ν.

(b) Effective Fermi velocity v versus ν.

Figure 3.7: Depicted is the ν-dependence of Fermi momentum and corresponding effective Fermi velocity in units of the Fermi velocity in graphene induced by interactions and shown for the same parameters as in figure 3.6. The dotted curve does not represent a fit, but is only a straight connection between neighbouring points and is meant to be only a guideline for the spectator. [77]

Fermi velocity and the result can be seen in figure 3.7(b). Also this quantity shows a basically linear dependence on the filling factor.

The results that have been shown in this section and obtained from the converged HF procedure hint at the existence of a pair of left- and right-movers which are a result of the single-particle dispersion that has been induced via interactions within the zero-mode band. Their Fermi momenta are well defined by the crossing of the energy band with the Fermi level and the dispersion around these points can be regarded as linear.

The current matrix element along the y-direction (evaluated at $y = 0$) is in general defined as

$$I_{n,k;n'k'} = v_F \int dx \, \psi_{n,k}^{\dagger}(x)\sigma_y\psi_{n',k'}(x) \tag{3.43}$$

with the symmetry relations

$$
\begin{aligned}
I_{n,k;-n,k'} &= -I_{n,k';-n,k}, \\
I_{0,k;n,k'} &= (-1)^{n+1}I_{0,-k;n,-k'}
\end{aligned}
\tag{3.44}
$$

for arbitrary n. Since the zero-modes in equation (3.22) only have a lower spinor component, there is no possibility to find a non-vanishing current as defined in equation (3.43). Therefore, no current can arise for the $n = 0$ case, even though there are the left- and right-movers described above. Thus, the counter-intuitive situation of a not flat dispersion without current is achieved. This would even still be valid for exact solutions of this problem since they also can not create an upper component, therefore no current can exist and thus

$$I_{0,k;0,k'} = 0 \tag{3.45}$$

holds, unless interactions with and virtual transitions to other bands are included. These will be treated in the following section.

3.5 ZERO-TEMPERATURE DC-CONDUCTANCE

gain the situation with a partially filled $n = 0$ band is considered but to continue the analysis, now not only intra- but also inter-band interactions are necessary. The aim is to find out whether a finite linear zero-temperature DC-conductance can be induced by these Coulomb interactions in the clean system regarded here. If it were possible, the presented setup would yield the opportunity to probe for the existence of interactions in the sample by measuring the conductance since it would only become finite in the presence of electron-electron interactions. The HF results achieved for the interactions inside the $n = 0$ band that have been presented in the previous section will be of further use in these calculations. They have been shown to give rise to the existence of an effective filling factor-dependent Fermi momentum $k_F(\nu)$ and an occupation of states with energy below the corresponding Fermi energy $E_F = \varepsilon_{k_F}$. Hence, it is possible to rewrite the full Hamiltonian as

$$H = \hat{H}_0 + \hat{W}. \tag{3.46}$$

But unlike before where solely the non-interacting physics were included in $\hat{H}_0$, in this scenario also the HF results of the intra-band $n = 0$ Coulomb interactions are treated within this quantity and merely the interactions with other bands have to be considered for $\hat{W}$. Thus one can write

$$\hat{H}_0 = \sum_{n,k} \tilde{E}_{n,k} c_{n,k}^\dagger c_{n,k} \tag{3.47}$$

where the single-particle energies are included as the normal energies for higher bands $\tilde{E}_{n\neq 0,k} = E_{n,k}$ and the effective HF single-particle energies $\tilde{E}_{0,k} = \varepsilon_k$ for the $n = 0$ band.

Furthermore, the ground state $|\Psi_0\rangle$ for $\hat{W} = 0$ hence corresponds to a Fermi sea whose occupation for zero temperature can be expressed as

$$f_{n,k} = f(\tilde{E}_{n,k}), \quad f(E) = \Theta(E_F - E) \tag{3.48}$$

with the Fermi function $f(E)$ and the Heaviside function defined as

$$\Theta(z_0 - z) = \begin{cases} 1, & \text{if } z > z_0 \\ \frac{1}{2}, & \text{if } z = z_0 \\ 0, & \text{if } z < z_0. \end{cases} \tag{3.49}$$

3.5.1 STANDARD KUBO FORMALISM

Regarding linear response theory, the linear conductance follows from the standard Kubo formula (compare section 2.10.1) with the Fourier transform of the retarded current-current correlator $\Pi^R(\omega)$ as [61, 111]

$$G = -e^2 \lim_{\omega \to 0} \frac{\text{Im}\Pi^R(\omega)}{\omega}.$$ (3.50)

This correlation function is in the time domain defined as

$$\Pi^R(t) = -i\Theta(t)C(t)$$ (3.51)

where $\Theta(t)$ is again the Heaviside function and

$$C(t) = \langle\Phi|[\hat{I}(t), \hat{I}(0)]_-|\Phi\rangle$$ (3.52)

includes the commutator of the time-dependent current operators $\hat{I}(t) = e^{iHt}\hat{I}e^{-iHt}$. The particle current operator that describes the current in y-direction is given by

$$\hat{I} = \sum_{n,n'} \sum_{k,k'} I_{n,k;n',k'} c^\dagger_{n,k} c_{n',k'}$$ (3.53)

where the matrix elements $I_{n,k;n',k'}$ are defined in equation (3.43). In addition, the normalized ground state of the entire Hamiltonian H is $|\Phi\rangle$.

For the further evaluation, it is convenient to rewrite the current-current correlator as

$$C(t) = X(t) - X(-t)$$ (3.54)

where the auxiliary correlation function $X(t)$ then reads

$$X(t) = \langle\Phi|\hat{I}(t)\hat{I}(0)|\Phi\rangle.$$ (3.55)

Moreover, there are other properties of the correlator $C(t)$ worth mentioning: First of all, from $C(-t) = -C(t)$ follows that $\tilde{C}(0) = 0$ must be true. Second, the relation $C^*(-t) = C(t)$ holds and therefore the Fourier transform $\tilde{C}(\omega)$ has to be real-valued only. In addition, one can find that $\tilde{C}(\omega)$ is connected with the imaginary part of $\Pi^R(\omega)$, thus corresponding to a spectral function describing fluctuations in the current, and this relation can be expressed as $\text{Im}\Pi^R(\omega) = -\tilde{C}(\omega)/2$. All this put together, the conductance can also be written as

$$G = \pi G_0 \frac{d\tilde{C}}{d\omega}(\omega = 0)$$ (3.56)

with the conductance quantum $G_0 = e^2/h$.

3.5.2 Keldysh formalism

Employing the Keldysh Green's function approach (see also [111] and section 2.11) presents a convenient way to involve $\hat{W}$ in the calculations. Within this technique, the value of a certain quantity – in this case the correlator $X(t)$ – is evaluated at a specific time t by considering the entire time evolution which starts at $t = -\infty$ and develops until $t = +\infty$, which is called forward branch, and afterwards returns to $t = -\infty$ (backward branch). The forward and backward branches are denoted with the Keldysh index $s = \pm$. With operators defined within the interaction picture according to $\hat{I}(t) = e^{it\hat{H}_0}\hat{I}e^{-it\hat{H}_0}$ and adding an index s to all dynamical quantities which corresponds to the different branches of the Keldysh contour, for example $\hat{I}(t) \to \hat{I}_s(t)$, the variables in the Keldysh formalism are calculated. Hence $X(t)$ can be formulated using the time evolution operator

$$U(t,t') = e^{i(t-t')H} = e^{-it\hat{H}_0}\mathcal{T}_\tau \exp\{-i\int_{t'}^{t} d\tau \hat{W}(\tau)\}e^{it'\hat{H}_0} \tag{3.57}$$

with the time-ordering operator $\mathcal{T}_\tau$ and reads

$$X(t) = \left\langle \Phi_0 \left| U(-\infty,t)\hat{I}U(t,+\infty)U(+\infty,0)\hat{I}U(0,-\infty) \right| \Phi_0 \right\rangle, \tag{3.58}$$

or in a reformulated form:

$$X(t) = \left\langle \Phi_0 \left| \mathcal{T}_C \left[S(\infty)\hat{I}_-(t)\hat{I}_+(0) \right] \right| \Phi_0 \right\rangle. \tag{3.59}$$

Here

$$S(\infty) = \mathcal{T}_C \exp\left(-i \int_{-\infty}^{\infty} d\tau \sum_{s=\pm} s\hat{W}_s(\tau) \right) \tag{3.60}$$

represents the time-evolution operator in the interaction picture and all these definitions require the time-ordering operator $\mathcal{T}_C$ that works along the contour of the Keldysh branches. The variable $W_s(\tau)$ that appears in the last definition (3.60) inside the sum over s demonstrates that formally all
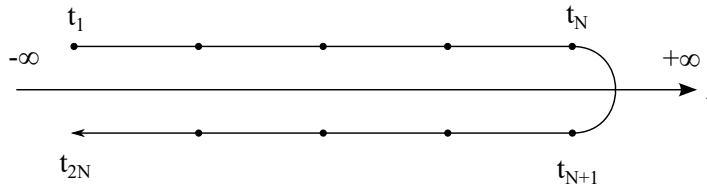
Figure 3.8: Schematic sketch of the Keldysh formalism concept. Depicted are the forward and backward branches (denoted as $s = \pm$, respectively) along the time axis, as well as a number of discrete points in time.

dynamical variables have been doubled when being labelled by the Keldysh index s and encodes the interactions.

3.5.3 PERTURBATION THEORY

For further evaluation, the conductance will be written as a perturbation expansion in the interaction Hamiltonian $\hat{W}$ that has already been mentioned before and is constructed to yield the effects of virtual inter-band transitions. The series up to the second order (compare section 2.9) reads

$$G = \sum_m G^{(m)} = G^{(0)} + G^{(1)} + G^{(2)} + O(\hat{W}^3). \tag{3.61}$$

Accordingly, also the quantity $X(t)$ can be expressed via an analogous series as

$$X(t) = \sum_m X^{(m)} = X^{(0)} + X^{(1)} + X^{(2)} + ..., \tag{3.62}$$

where the term of mth order reads

$$
\begin{aligned}
X^{(m)}(t) &= \frac{(-i)^m}{m!} \int_{-\infty}^{\infty} d\tau_1 \cdots d\tau_m \sum_{s_1,...,s_m=\pm} s_1 \cdots s_m \\
&\times \left\langle \Phi_0 \left| \mathcal{T}_C \left[\hat{W}_{s_1}(\tau_1) \cdots \hat{W}_{s_m}(\tau_m) \hat{I}_-(t) \hat{I}_+(0) \right] \right| \Phi_0 \right\rangle.
\end{aligned} \tag{3.63}
$$

Furthermore, the Keldysh Green's function for fermions is defined as [111]

$$\mathcal{G}^{(s,s')}_{n,k,n',k'}(t - t') = -i \langle \mathcal{T}_C \{ c_{n,k,s}(t) c^{\dagger}_{n',k',s'}(t') \} \rangle. \tag{3.64}$$

Applying Wick's theorem to the products of free fermion operators, which are time-ordered along the Keldysh contour, in equation (3.63), the ground state average $X^{(m)}$ can be written in terms of non-interacting Keldysh Green functions of the form

$$\mathcal{G}^{(s,s')}_{n,k}(t - t') = -i \langle \Phi_0 | \mathcal{T}_C [c_{n,k,s}(t) c^{\dagger}_{n,k,s'}(t')] | \Phi_0 \rangle. \tag{3.65}$$

In Keldysh space the components after Fourier transformation are given by

$$
\begin{aligned}
\tilde{\mathcal{G}}^{(s,s)}_{n,k}(E) &= \frac{s}{E - \tilde{E}_{n,k} + is\,\mathrm{sgn}\left(\tilde{E}_{n,k} - E_F\right)\,0^+}, \\
\tilde{\mathcal{G}}^{(s,-s)}_{n,k}(E) &= 2\pi i s f(sE)\,\delta\left(E - \tilde{E}_{n,k}\right)
\end{aligned} \tag{3.66}
$$

where again the Fermi function $f(E)$ and the sign function $\mathrm{sgn}(E)$ are utilized.

3.5.4 DIAGRAMMATIC APPROACH

With these ingredients it is possible to calculate all necessary terms of the conduction, but they also allow for the construction of conduction diagrams according to a certain number of rules. First of all, every diagram has to consist of two two-point external vertices corresponding to the current operators $\hat{I}_-(t)$ and $\hat{I}_+(0)$ with respective Keldysh indices $s = \pm$ in equation (3.63). In the diagram language they are represented by filled circles.

Second, a diagram of mth order contains exactly m four-point internal vertices which represent the interaction Hamiltonian $\hat{W}$. Thus they stand for the m terms $\hat{W}_{s_1}(\tau_1)...\hat{W}_{s_m}(\tau_m)$ and are depicted as filled squares. The distinction between two- and four-point vertices is visible in the scheme by the number (two or four, respectively) of lines coming in and/or going out of the vertex, and it can be understood regarding the number of particles participating in the process. Whereas for the current operator in equation (3.53) only two fermionic operators, namely $c_{n,k}^\dagger$ and $c_{n',k'}$ are needed, four of these take part in the definition of the interaction Hamiltonian $\hat{W}$, which equals equation (3.27) without taking into account the intra-band interactions with $n_1 = ... = n_4 = 0$ that are already encoded in H_0.

In addition taking into account the Keldysh normalization condition $\langle \Phi_0 | S(\infty) | \Phi_0 \rangle = 1$, which pays respect to the fact that vacuum diagrams are considered here, and also $\langle \Phi | \hat{I}_\pm(t) | \Phi \rangle = 0$, only connected diagrams have to be considered.

Furthermore, there is a so-called "selection rule" which allows the convenient neglecting of some diagrams and the corresponding terms without the necessity of lengthy calculations. Its origin is to be found in the vanishing current matrix elements (3.45) for intra-band interactions in the
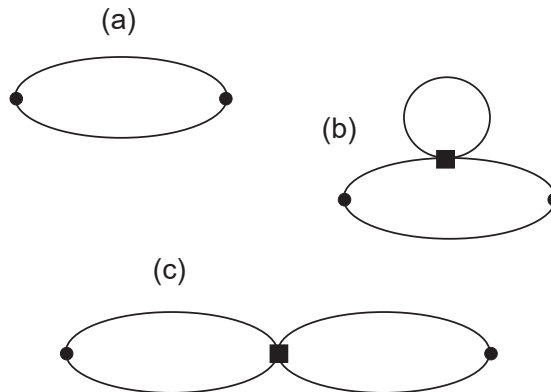
Figure 3.9: Diagrammatic expressions for the orders $m = 0$ in panel (a) and $m = 1$ in pictures (b) and (c). [77]
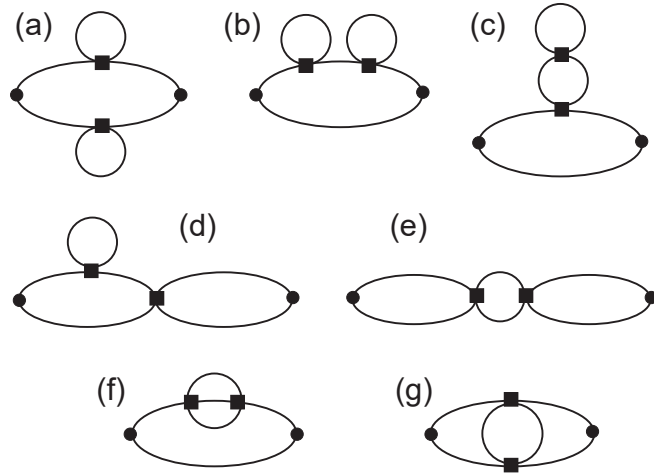
Figure 3.10: Diagrams belonging to second order ($m = 2$). [77]

$n = 0$ band[3] and it states that the contribution of a certain diagram to the conduction is zero whenever it contains a current vertex with a Keldysh index s which is linked to two other vertices that happen to have the opposite index $-s$.

The corresponding diagrams up to the second order are shown in the figures 3.9 for the zeroth and first order and 3.10.

3.5.5 CONDUCTANCE UP TO SECOND ORDER

The zeroth-order contribution to the conductance, which represents the case without inter-band transitions is expected to vanish following the lines of the discussion made in section 3.4. To verify this anticipation, the calculation is carried out nevertheless. The expression related to the only existing zeroth-order diagram in figure 3.9 (a) can be written as

$$X^{(0)}(t) = \sum_{n,k;n',k'} \left| I_{n,k;n',k'} \right|^2 \mathcal{G}_{n,k}^{(-,+)}(t) \mathcal{G}_{n',k'}^{(+,-)}(-t) \tag{3.67}$$

and its Fourier-transform reads

$$\tilde{X}^{(0)}(\omega) = 2\pi \sum_{n,k;n',k'} \left| I_{n,k;n',k'} \right|^2 (1 - f_{n,k}) f_{n',k'} \delta(\tilde{E}_{n,k} - \tilde{E}_{n',k'} - \omega). \tag{3.68}$$

---

[3]To be precise, it is a consequence following from $\lim_{\omega \to 0} dZ_{s=\pm}(\omega)/d\omega = 0$ where $Z_s(\omega) = \int dE(\ldots)\tilde{\mathcal{G}}_{n,k}^{(-s,s)}(E + s\omega)I_{n,k;n',k'}\tilde{\mathcal{G}}_{n',k'}^{(s,-s)}(E)$, which is obtained from Eqs. (3.45) and (3.66).

Using that $dF(E)/dE = -\delta(E - E_F)$ due to the definition of the Fermi function (3.48), the zeroth-order conduction is given by

$$G^{(0)}/G_0 = \frac{\pi^2 \rho_0^2}{2} \operatorname{Tr}_F(I \circ I) \tag{3.69}$$

where $\rho_0 = 1/\pi v$ is the density of states and $v = \partial_k \varepsilon_{k=k_F}$. Besides, further convenient definitions to shorten the notation have been used in this expression: On the one hand, the symbol "$\circ$" stands for Fermi level convolution and thus the matrix elements of $A \circ B$ are given by

$$(A \circ B)_{n,k;n',k'} = \sum_{\pm} A_{n,k;0,\pm k_F} B_{0,\pm k_F;n',k'} \tag{3.70}$$

while on the other hand "Tr_F" declares a Fermi level trace according to

$$\operatorname{Tr}_F A = \sum_{\pm} A_{0,\pm k_F;0,\pm k_F}. \tag{3.71}$$

Considering these last two definitions (3.70) and (3.71), it is obvious that all matrix elements are evaluated at the Fermi level which lies inside the $n = 0$ band and due to equation (3.45), this conductance contribution vanishes, i.e. $G^{(0)} = 0$.

Moreover, exploiting the first-order diagrams and the corresponding equations, the first-order conductance correction can be calculated to be

$$G^{(1)}/G_0 = -2\pi^2 \rho_0^2 \operatorname{Tr}_F \left[I \circ (\delta I - K) \right]. \tag{3.72}$$

The first, term involving the quantity

$$\delta I = [I, \Lambda]_-, \tag{3.73}$$

originates from the diagram in figure 3.9 (b). Here, δI is the commutator of the current matrix with the elements $I_{n,k;n',k'}$ and the auxiliary hybridization matrix Λ defined via

$$\Lambda_{n,k;n',k'} = \frac{\delta_{k,k'}(1 - \delta_{n,n'})}{\tilde{E}_{n,k} - \tilde{E}_{n',k}} \sum_{n_1,k_1} f_{n_1,k_1} W_{k,k_1;q=0}^{(n,n_1,n_1,n')}. \tag{3.74}$$

In k-space Λ is diagonal and it captures the virtual transitions from one band to another, induced due to interactions. Therefore, δI describes the leading order of the renormalization of the current matrix by virtual interband transitions.

The second term arises from diagram 3.9 (c) and includes the fluctuation matrix K, whose matrix elements are given by

$$K_{n,k;n'k'} = \sum_{n_1,k_1;n_2,k_2} \delta_{k_2,k_1+k'-k} \frac{f_{n_1,k_1} - f_{n_2,k_2}}{\tilde{E}_{n_2,k_2} - \tilde{E}_{n_1,k_1}} I_{n_1,k_1;n_2,k_2} W_{k_2,k;k-k_1}^{(n_2,n,n_1,n')}. \tag{3.75}$$

Also this contribution, belonging to the first correction, vanishes identically, i.e. $G^{(1)} = 0$, since it again entails the current matrix I evaluated at the Fermi points. The first non-zero term for this situation can therefore only be found in the second-order contribution. For a different situation, however, which doesn't sport the characteristic vanishing current matrix elements, the equations (3.69) and (3.72) can also represent finite contributions and thus be considered as "non-interacting conductance", as well as the ballistic interpretation of the "interaction correction", respectively [112–114]. Such a setting would already be given for the considered magnetic graphene waveguide, if there was an energy shift and hence a $n \neq 0$ band had been partially filled, since then the Fermi level convolution and trace would take place in a finite-energy band with finite current matrix elements.

The second-order conductance is given by a sum of topologically distinct diagrams shown in figure 3.10. Taking a closer look at these pictures, one finds that, due to the "selection rule" mentioned earlier, the process associated with diagram (c) does not contribute to the conductance (as it was already true for the diagram in figure 3.9 (b)), because it is not possible to distribute a Keldysh index to the lower four-point vertex such that there is no current vertex connected to two vertices with opposite index. Furthermore, also the diagrams (f) and (g) yield no finite result due to the fact that their expressions contain products of several Fermi functions and hence the energy constraints which result from these can never be fulfilled.

Thus, the entire conductance up to second order in this perturbative approach is obtained as

$$G = G^{(2)} = G_a^{(2)} + G_b^{(2)} + G_d^{(2)} + G_e^{(2)}. \tag{3.76}$$

The first two terms, evaluated at once, yield

$$(G_a^{(2)} + G_b^{(2)})/G_0 = 2\pi^2 \rho_0^2 \operatorname{Tr}_F(\delta I \circ \delta I) \tag{3.77}$$

whereas the third term gives

$$G_d/G_0 = -4\pi^2 \rho_0^2 \operatorname{Tr}_F(\delta I \circ K) \tag{3.78}$$

and the last diagram leads to

$$G_e/G_0 = 2\pi^2 \rho_0^2 \operatorname{Tr}_F(K \circ K). \tag{3.79}$$

Everything added up, the finite and positive result for the conductance to second order in $\hat{W}$ reads

$$G/G_0 = 2\pi^2 \rho_0^2 \operatorname{Tr}_F\left[(\delta I - K) \circ (\delta I - K)\right]. \tag{3.80}$$

For the limit $d \to 0$ however, this result does not hold, since for the flat zero-mode dispersion ε_k in this situation k_F is ill-defined.

### 3.5.6 Numerical evaluation and resulting conductance

Deeper insight in the behaviour and dependence of the result for the conductance in equation (3.80) can only be achieved by exploiting numerical methods. The inquiry still left open is whether there is a finite conductance for the zero-mode and also if and how it depends on the filling factor.

In principle, for a thorough analysis all interaction matrix elements for interactions between all possible energy bands have to be calculated. Since this would be lengthy and is additionally not expected to yield much more information, only the $n = 0$ plus the energetically closest $n = \pm 1$ bands are taken into account which create the main contribution to the conductance.

Furthermore, as already described earlier, a momentum cutoff k_c is introduced. This bandwidth allows only momenta $|k| < k_c$ for the evaluation to assure that the edge states with large momenta do not take part in the calculations. This effectively implies a restriction of the single-particle Hilbert space and has the additional benefit that less k-states have to be considered, hence less values for all matrices and thus less calculations are needed. For the numerics the same parameters have been chosen as before. Therefore, for the given value for the waveguide width $d = 2l_B$ a cutoff $k_c = 1.6 l_B^{-1}$ has been selected. To validate this choice, also other values inside the cutoff range $1.5 \lesssim k_c l_B \lesssim 1.7$ have been tested and found not to change the result significantly.

For the numerical calculation of the conductance, a lot of steps are necessary: To begin with, the energies of the three bands $n = 0, \pm 1$ that have already been obtained via bisection and HF techniques and shown before in figures 3.2 and 3.6, are needed[4]. In the next step, the wave functions for all needed k and a discrete number of x states are evaluated where for the higher bands first the different coefficients $C_i^{(\pm 1, k)}$ have to be obtained via the normalization condition and equation (3.17). Thirdly, the form factors and current matrix elements for the required values of k, k', q and n have to be calculated using their definitions (3.30) and (3.43), respectively, making also use of the corresponding symmetry relations (3.31) and (3.44), and stored. Moreover, the necessary interaction matrix elements are evaluated in different loops varying the fine structure constant α and all the dependent variables according to the rules given in section 3.4. In addition, the filling factor ν, which requires not only simple scaling arguments but reading of the different results from the HF scheme for the depending quantities (effective Fermi velocity v, $n = 0$ energy spectrum ε_k and hence the Fermi energy E_F and Fermi momentum k_F), is included. To achieve this, the definition (3.35) and furthermore included quantities, involving also the Coulomb potential (3.29), are implemented and again the symmetry relations (3.33) are taken advantage of to ensure that no expendable calculations are carried out. With all these stored values the matrices δI and K are built according to (3.73) and (3.75) where the Fermi factors are included as Heaviside functions. Everything put together, the conductance for different ν and α can be obtained.

---

[4]It is worth noting that the energy dispersion for the $n = \pm 1$ bands does not depend on the filling factor whereas the $n = 0$ dispersion does as seen in figure 3.6.
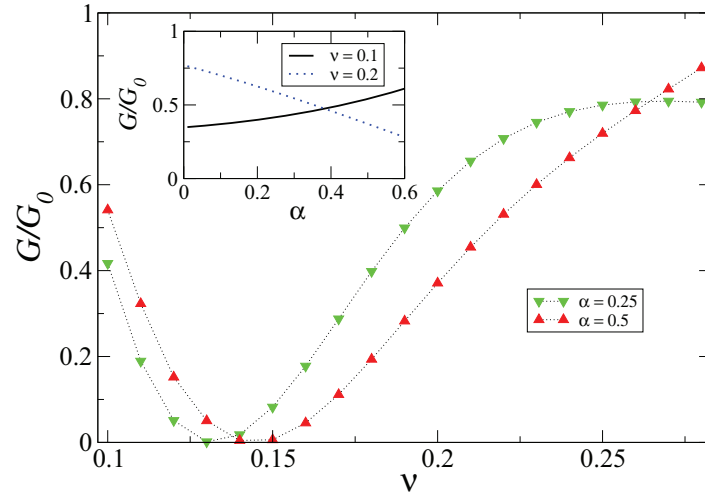
Figure 3.11: Zero-mode MGW DC-conductance as given in equation (3.80) depending on the filling factor ν for two chosen values of the fine structure constant α in the main panel, as well as the dependence on α for two distinct values of ν in the inset. Parameters are chosen as before and the dotted line in the main panel is again only meant to be a guide to the eye instead of a real fit. [77]

The zero-temperature MGW conductance clearly shows a dependence on the filling factor ν, as depicted in the main panel of figure 3.11. Obviously, there also exists a minimum around $\nu = \nu_{\min}$ where for a fine structure constant of $\alpha = 0.5$ a value of $\nu_{\min} \approx 0.145$ can be read off. An explanation for the existence of this prominent feature can be found in the Coulomb-assisted hybridization between the zero-mode and $n = \pm 1$ bands: Whereas the $n = -1$ band is still rather close to the zero-mode band for small fillings, which imply also a little chemical potential as explained in section 3.4, the Fermi level approaches the $n = 1$ band for larger ν. Therefore, for small ν the quantity δI and the current renormalization effects included within are the dominant force while for higher fillings the part of the fluctuation matrix K takes over and presides over the other contribution. For a filling $\nu \approx \nu_{\min}$ almost total cancellation of the two terms can be found.

Considering the dependence of the conductance on the fine structure constant α on the contrary for two different values of ν, as depicted in the inset of figure 3.11, positioned left and right of the minimum, one finds a simpler behaviour, as expected from the simple scaling arguments made before. For a certain filling, the conductance monotonically increases or falls with α, depending on whether $\nu < \nu_{min}$ or $\nu > \nu_{min}$, respectively. This is merely a consequence of the shifting of the minimum to higher values with increasing α, as visible in the main panel, which again is a result of the upward shifting of the chemical potential with α. Due to this, the cancellation of the terms in equation (3.80) is moved to larger ν values.

Regarding the limit $\alpha \to 0$, from naive interpolation of the curves in the inset, one would assume

a finite conductance. This cannot be true since without interactions the conductance must vanish as explained before. The reason for this seeming contradiction lies in the fact that the HF theory applied before remains valid only for a frequency scale ω much smaller than the effective zero-mode bandwidth, which is proportional to α. As a result the limit $\alpha \to 0$, which directly implies that the ε_k bandwidth goes to zero, is not allowed within the boundaries of this model since then the limit $\omega \to 0$, which is essential for equation (3.80), cannot be accomplished any longer. Furthermore, also the particle-hole symmetry seems to be broken since for larger values of ν (not shown here) where this approach is not substantiated any more the conductance has very high values and the expected connection between ν and $1 - \nu$ states is not present. This is a result of the short-range interaction potential established in equation (3.29) since for a simple interaction decaying as $1/r$ where $\tilde{V}_{1/r}(q = 0) = 0$ is required by electroneutrality, particle-hole symmetry would still hold and thus $G_{1/r}(\nu) = G_{1/r}(1 - \nu)$ should be true.

The questions asked in the beginning of this section can be answered affirmatively: First there is a finite zero-mode conductance and second it strongly depends on the filling factor ν. This might enable the probing of the existence of interactions due to transport experiments because it yields a conducting phase which is interaction-induced and shows a strong, measurable signature.

But still not all inquiries have been satisfactorily addressed yet. The question still arises, what kind of a state of matter this interaction-induced conductor represents and whether it is possible to be described using the Fermi liquid or Tomonaga-Luttinger liquid theory.

3.6 INTERPRETATION REGARDING THE TLL FORMALISM

The situation, when – in contrast to the calculations presented in this approach – the chemical potential does not intersect the $n = 0$ but one of the other bands, is portrayed in [89] for a similar MGW. Within this model, an entirely different result has been observed: While here a conductance that strongly, but continuously depends on the filling factor ν is obtained, for the other case a conductance quantized in multiples of G_0 is found. This originates from the fact that transport is mainly dominated by the spatially well-separated (and thus protected from back-scattering) left and right-moving snake states. Furthermore, no dependence on the filling factor of the respective band is anticipated for this case in contrast to the result obtained here. In [89], it is also shown that the state of matter achieved for the finite-energy bands intersected by the chemical potential represents a conventional Tomonaga-Luttinger liquid, which is created by electron-electron interactions and proves to be mostly unaffected by disorder effects. For this case, it was also possible to obtain the finite temperature power-law corrections that are expected for a TLL, compare section 2.6.

Hence, the question arises whether the state in which our system is, can also be described using the TLL formalism. This might be possible since we have an effective one-dimensional material as well as electron-electron interactions, which are known to have destabilizing effects on the

state of the Fermi liquid for one-dimensional band metals with low-energy excitations close to the Fermi points, limited due to phase-space restrictions. In case of an affirmative answer, all properties for the low-energy regime should be describable using one parameter[5][69, 116, 117]. This dimensionless interaction parameter g_{TLL} determines the Kubo conductance according to

$$G = g_{TLL}G_0 \tag{3.81}$$

for a clean and infinitely long TLL and restores the Fermi liquid limit for $g_{TLL} = 1$ [118]. It is given by

$$g_{\text{TLL}} = \left[\frac{\pi}{v} \frac{\partial^2 (\mathcal{E}_0/L_y)}{\partial k_F^2} \right]^{-1/2} \tag{3.82}$$

with the single-particle velocity $v = |\partial_k \varepsilon_{k=k_F}|$ and the ground-state energy density $\mathcal{E}_0/L_y$ and is determined via the ground-state compressibility due to the interaction strength [69, 119]. With this parameter also other quantities in a TLL can be expressed in terms of certain power-laws, for example correlation functions as the single-particle equal-time Green's function

$$\langle \hat{\Psi}(x, y)\hat{\Psi}^\dagger(x, 0) \rangle \sim |y|^{-\gamma} \tag{3.83}$$

where the exponent is given by $\gamma = 1 + [g_{\text{TLL}} + 1/g_{\text{TLL}} - 2]/4$, see [69, 120].

The parameter defined in equation (3.82) is the same as used in [89], and is derived from the Coulomb interactions that exist between the counterpropagating snake states and can thus be varied by changing the waveguide width d. Without these interactions, the snake states, which are spatially located near the sign-changing lines of the magnetic field as seen in figure 3.1, simply propagate without disturbance at the Fermi velocity v_F.

This case with the partially filled $n = 0$ band, however, cannot be described using the TLL formalism because of a number of reasons: In the first place, no Fermi surface exists without interactions since only with Coulomb interactions switched on an effective dispersion, which is not flat (compare figure 3.6), emerges. Secondly, assuming that the interactions cause the existence of a TLL, it would be possible to calculate a Fermi velocity v and momentum k_F (like shown in figure 3.7) using the dispersion. As a consequence, a g_{TLL} can be obtained from its definition (3.82) and the HF ground-state energy in equation (3.40) can be calculated. This expression, however, does not describe the conductance according to (3.81) adequately.

This is especially impossible due to the vanishing zero-mode conductance caused by the form of the zero-mode eigenstates when only regarding the $n = 0$ band. Thus, this band cannot be classified within Luttinger liquid theory using the bosonized Gaussian field formalism [116]. Even including inter-band interactions when a non-vanishing conductance is received, the unconventional dependence on the filling factor ν, which does not fit the TLL definition (3.81) either, remains to be considered.

---

[5]Ignoring the spin sector, still two parameters have to be considered in principle but since additionally Galilei invariance holds for the continuum model considered here, the number of TLL parameters is further reduced to one.

Summing up, the $n = 0$ band – in contrast to all other $n \neq 0$ bands – cannot be treated within the Luttinger liquid theory. How to describe this phase in more detail is left for future research.

3.7 CONCLUSIONS

While electron-electron interactions normally tend to suppress conductance in materials, as it has been shown in [112–114], for the case shown in this chapter a genuinely different effect has been found. Instead of weakening the conductance, Coulomb interactions[6] create a finite conductance in the MGW. Thus, an insulator is transformed into a conductor by switching on interactions.

In the previous sections, the whole analysis has been described starting from the setup and the single-particle description. Furthermore, the different wave functions have been derived and HF results for the zero-mode sector and hence interactions only within the $n = 0$ band have been presented. Finally, the non-vanishing zero-temperature result with a non-trivial dependence on the filling factor ν has been displayed. This state of matter cannot be described by the conventional TLL description used for interacting 1D conductors [120].

In order to summarize the main message, the physics of the $n = 0$ band are different from those of the other bands, which develop a quantized conductance. In contrast, the conductance found for the zero-energy level is non-universal and shows a strong dependence on the partial filling of the $n = 0$ level.

The vanishing of this conductance when the electron-electron interactions are switched off hence yields a novel and direct way to probe the existence of interactions via transport experiments.

Furthermore, a similar behaviour is expected to arise also for other settings than the MGW. One example is given by carbon nanotubes with metallic properties that are positioned inside a magnetic field, which is inhomogeneous on the length scale of the radius, such that its direction is perpendicular to the axis that runs along the tube [121]. Therefore, a finite magnetic flux exists inside the tube and a finite degeneracy of the zeroth Landau level according to $\Phi/(hc/e)$ can be ensured using the index theorem [7, 91]. For such a system, a behaviour corresponding to the MGW studied here is anticipated, including the $n = 0$ band dispersion for intra-band interactions, as well as the development of a finite conductance only for the existence of inter-band interactions and thus the possibility to switch between insulating and conducting states via interactions. In addition, these $n = 0$ Landau level conductance features are expected to differ considerably from those of the other $n \neq 0$ levels.

---

[6]In the case $d = 0$ these interband Coulomb interactions would correspond to Landau level mixing [115].

4

Graphene *p-n* junctions

Within the model considered in this chapter the applied magnetic field is – unlike in section 3 – taken constant over the entire graphene sample while now a *p-n* junction is evoked using an inhomogeneous potential[1] $V(\mathbf{r})$. Similarly to the snake states that existed in the case of a magnetic field with adjacent regions of positive and negative $\mathbf{B}$, also in this case chiral interface states are obtained that travel along the *p-n* interface. Due to Klein tunnelling in graphene it is possible that an electron is transmitted from an *n*-doped region into a *p*-doped region as a hole with a finite probability $P(\vartheta)$ that depends on the angle of incidence ϑ. In the perpendicular and constant magnetic field the two particles of opposite charge describe circular motions of opposite orientation sense and thus allow again for a snaking movement along the *p-n* interface. But other than in the previous chapters, this isn't the only possibility: Unless the incidence angle is $\vartheta = 0$, i.e. the case of perpendicular impinging for which Klein tunneling becomes perfect (resulting in $P(0) = 1$), there is always a finite probability $1 - P(\vartheta)$ that the particle is reflected back and performs a skipping orbit like in the semiclassical picture of an edge state, e.g. for the conventional quantum hall effect. Hence, the motion of a particle will in general consist of a random sequence of snaking and skipping orbits, semiclassically spoken [123–125].

In the following, two different geometries will be discussed, namely a straight and a circularly shaped *p-n* junction. Numerical studies of related situations can be found in [126, 127]. For both systems, a clean graphene sheet without disorder is assumed in agreement with the high quality that can be accomplished lately and interaction effects are not taken into account (in contrast to e.g. devices featuring *p-n-p* junctions where interactions between counter-propagating interface states can lead to non-Fermi liquid behaviour [89]).

Possibly, the predictions within this chapter might also for example apply to the Dirac fermions that arise in the surface states in topological insulators [128–131].

The content of this section can also be found in the publication [132].

---

[1] Another possibility to create qualitatively good *p-n* junctions in graphene is given by the controlled diffusion of metallic contacts, compare [122].

4.1 Straight *p*-*n* junction

At first, the geometry of a straight interface between the *p*- and *n*-doped regions in the plane is studied.

4.1.1 Model

The low-energy Dirac fermions in the graphene sheet are described using the standard Dirac-Weyl Hamiltonian in two dimensions according to

$$H = v_F \sigma_x \left(p_x + \frac{e}{c} A_x \right) + v_F \sigma_y \left(p_y + \frac{e}{c} A_y \right) + V \sigma_0, \tag{4.1}$$

with the momentum $p_{x,y} = -i\partial_{x,y}$ and the matrices $\sigma_{x,y,z}$ (with identity σ_0) are the Pauli matrices acting on the sublattices defined by the two-atomic basis in the Wigner-Seitz cell of the honeycomb lattice. The spatial components of the vector potential, namely (A_x, A_y) contain the homogeneous magnetic field $B = \partial_x A_y - \partial_y A_x$ with $B > 0$ which is applied perpendicular to the sheet[2]. Choosing the Landau gauge for simplicity, this yields $(A_x, A_y) = (0, Bx)$.

Electrostatic gating can create a scalar potential $V(x, y)$ which in this case of the straight junction is considered to be constant in y-direction and to develop a step in x-direction as

$$V(x) = V_0 \operatorname{sgn}(x), \tag{4.2}$$

where $V_0 > 0$. Although the model of a sharp junction is used for the calculations, the spatial variation is assumed to be smooth on atomic distances in graphene since thus the quasiparticles are not scattered between the different K-valleys. In experiments the realization of a sharp step potential is involved, and also theoretically the minimum distance over which the potential varies has been determined to be the magnetic length l_B [64]. Nevertheless, the description in (4.2) describes sufficiently well the underlying physics and simplifies the mathematical treatment [128, 129]. Furthermore, the situation at a single K point is considered and also the spin is not considered allowing for compact notation.

Dimensionless units measuring energies[3] and length in multiples of the magnetic energy and magnetic length according to

$$E_B = \sqrt{2} v_F / l_B, \; l_B = \sqrt{c/eB} \tag{4.3}$$

---

[2]Here, a true external magnetic field is considered. Nevertheless the formalism can easily be adapted to also handle strain-induced so-called pseudo-magnetic fields.

[3]Note the difference to the units in the last chapter is just given by a factor $\sqrt{2}$ in the energy and only used to simplify the notation.
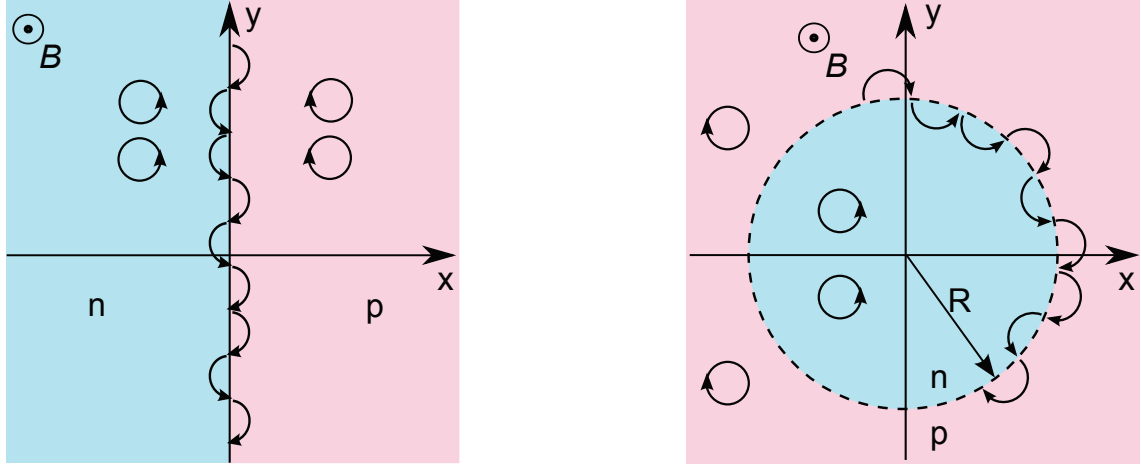
Figure 4.1: Different graphene *p-n* junctions considered here, i.e. the straight case (left panel) and the circular geometry (right panel), including sketches of examples for semiclassical cyclotron and chiral skipping-snaking interface states. Blue and pink coloured areas symbolize *n*-doped and *p*-doped regions, respectively, where the potential is constant $V = -V_0$ and $V = +V_0$; everywhere a constant magnetic field B is applied. [132]

with $\hbar = 1$ are employed during these chapters. The two setups for the straight and circular geometry are schematically depicted in figure 4.1.

Due to the homogeneity along the y-direction, the problem of the straight junction can effectively be reduced to a one-dimensional system, and the spinor eigenstates can be written as

$$\Psi_k(x, y) = e^{iky}\Phi_k(x), \quad \Phi_k(x) = \begin{pmatrix} u_k(x) \\ iv_k(x) \end{pmatrix}, \tag{4.4}$$

with $k = k_y$ being the conserved wavenumber. Defining the new coordinate $q = \sqrt{2}(x + k)$, ladder operators $a = \partial_q + q/2$ and $a^\dagger = -\partial_q + q/2$ can be created which fulfil the commutation relation $[a, a^\dagger] = 1$. With these (and the dimensionless units), the Dirac-Weyl Hamiltonian can be rewritten as

$$H = \begin{pmatrix} V(x) & -ia \\ ia^\dagger & V(x) \end{pmatrix}. \tag{4.5}$$

Furthermore, one finds that for regions where the potential has a constant value, i.e. $V(x) = V = $ const,

$$(V - E)u + av = 0, \quad a^\dagger u + (V - E)v = 0 \tag{4.6}$$

is obtained and inserting these into one another, this yields a representation of Weber's differential equation, namely

$$\left[a^\dagger a - (E - V)^2\right]v = \left[\frac{d^2}{dq^2} + (E - V)^2 + \frac{1}{2} - \frac{q^2}{4}\right]v = 0. \tag{4.7}$$

Weber's equation is solved by parabolic cylinder functions and exploiting their recurrence relations (compare [101, 102])

$$aD_p(q) = pD_{p-1}(q), \quad a^\dagger D_p(q) = D_{p+1}(q), \tag{4.8}$$

it becomes obvious that $v = D_p(q)$ with $p = (E - V)^2$ and q as defined above is a solution to equation (4.6). The second, independent solution is given by $D_p(-q)$ which can easily be checked regarding that $q \to -q$ leads to $a \to -a$ as well as $a^\dagger \to -a^\dagger$ and thus the operator $a^\dagger a$ remains unchanged. Hence, the two independent (non-normalized) spinor solutions can be constructed as

$$
\begin{aligned}
\Phi_{k,V}^{(1)}(x) &= \begin{pmatrix} (E - V)D_{(E-V)^2-1}(\sqrt{2}(x + k)) \\ iD_{(E-V)^2}(\sqrt{2}(x + k)) \end{pmatrix} \\
\Phi_{k,V}^{(2)}(x) &= \begin{pmatrix} -(E - V)D_{(E-V)^2-1}(-\sqrt{2}(x + k)) \\ iD_{(E-V)^2}(-\sqrt{2}(x + k)) \end{pmatrix}.
\end{aligned}
\tag{4.9}
$$

Considering the asymptotic behaviour for large real positive and negative values of the argument [101], it follows that the solution $\Phi^{(2)}$ must be taken on the left side of the *p-n* interface where $x < 0, V = -V_0$ while $\Phi^{(1)}$ solves the problem on the right side ($x > 0, V = V_0$). With complex coefficients $c_{</>}$ this can be summarized as

$$\Phi_k(x) = \begin{Bmatrix} c_< \Phi_{k,-V_0}^{(2)}(x), & x < 0, \\ c_> \Phi_{k,+V_0}^{(1)}(x), & x > 0, \end{Bmatrix} \tag{4.10}$$

4.1.2 ENERGY SPECTRUM

The matching condition for $x = 0$ together with the condition of normalizability yields the quantization condition for the energies

$$\Delta_k(E) = \det \left[\Phi_{k,-V_0}^{(2)}(0), \Phi_{k,+V_0}^{(1)}(0) \right] = 0 \tag{4.11}$$

as well as the coefficients. Using a similar numerical bisection method as in chapter 3, equation (4.11) can be solved and yields the spectra in figure 4.2 for different values of V_0. As visible the solutions $E = E_{n,k}$ which are labelled by the band index n which corresponds to the Landau level index for zero potential, i.e. $V_0 = 0$, and the wavenumber k have an antisymmetric behaviour following from $\Delta_k(E) = \Delta_{-k}(-E)$:

$$E_{-n,-k} = -E_{n,k}. \tag{4.12}$$

The energy spectrum just reduces to the relativistic Landau levels $E_{n,k}^{(0)} = \text{sgn}(n)\sqrt{|n|}$ if the case of a vanishing potential $V_0 = 0$ is regarded. Here, $\text{sgn}(n)$ represents the sign function and the
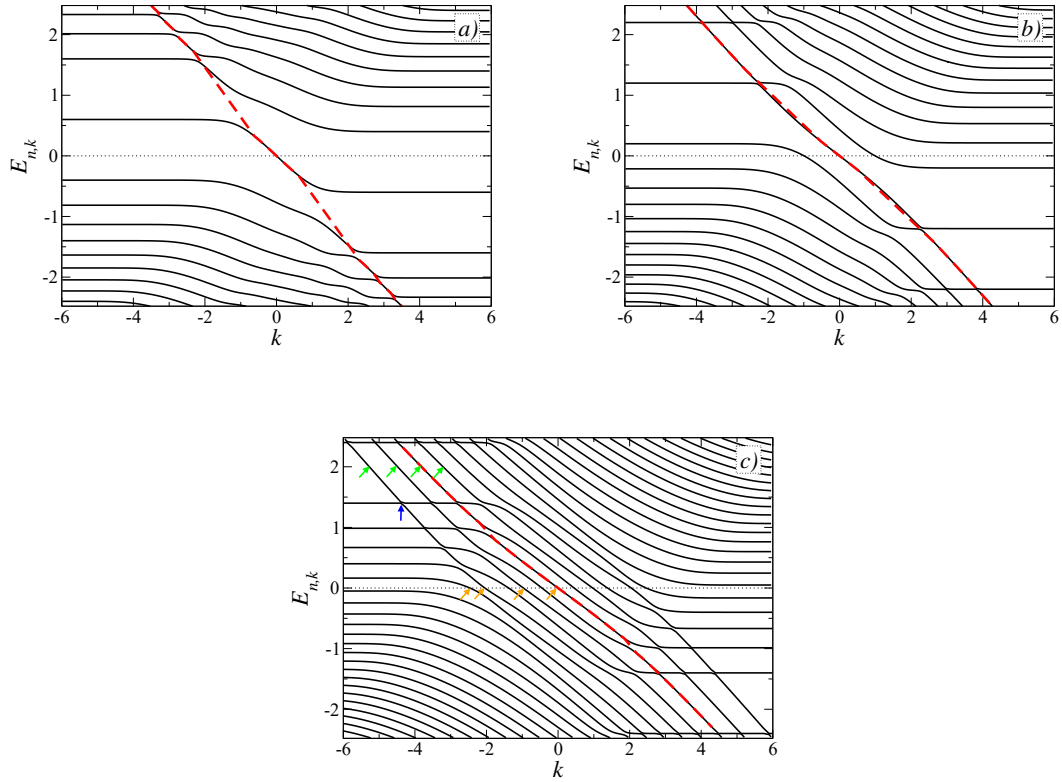
Figure 4.2: Energy spectrum $E_{n,k}$ depending on wavenumber k obtained numerically for a straight junction for different values of the potential V_0, namely: (a) $V_0 = 0.6$, (b) $V_0 = 1.2$, (c) $V_0 = 2.4$. Red dashed curves are guides to the eye only and illustrate the central chiral interface state passing through $k = E = 0$. The green (orange) arrows in (c) indicate states at fixed energy $E = 2$ ($E = 0$) for which density profiles are shown in figure 4.6 (figure 4.7). The avoided crossing which is depicted in figure 4.5 happens at the position of the blue vertical arrow. [132]

energies become independent of the wavenumber k, although the corresponding cyclotron orbits have their center at values $\bar{x} = -k$. Exactly such flat, dispersionless parts of the energy levels can also be spotted in the spectra in figure 4.2 for large $|k|$. Since for large $|k|$, the corresponding states are also located far away from the interface in the bulk (since this inflicts large $|x|$ values) these states are mostly unaffected by the change in the potential created by the *p-n* junction and hence only experience a constant potential of $\pm V_0$. Therefore, they are simply Landau levels shifted by the respective potential. This can in addition be verified by expanding the parabolic cylinder functions for large arguments according to [101]

$$D_p(z) = z^p e^{-z^2/4} \left(\sum_{n=0}^{N} \frac{(-p/2)_n(1/2 - p/2)_n}{n!(-z^2/2)^n} + O|x^2|^{-N-1} \right), \quad \text{for} \quad |\arg z| < \frac{3\pi}{4},$$

$$D_p(z) = (z)^p e^{-z^2/4} \left(\sum_{n=0}^{N} \frac{(-p/2)_n(1/2 - p/2)_n}{n!(-z^2/2)^n} + O|z^2|^{-N-1} \right) +$$

$$- \frac{\sqrt{2\pi}}{\Gamma(-p)} e^{p\pi i} z^{p+1} e^{z^2/4} \left(\sum_{n=0}^{N} \frac{(p/2)_n(1/2 + p/2)_n}{n!(z^2/2)^n} + O|z^2|^{-N-1} \right),$$

$$\text{for} \quad \frac{\pi}{4} < \arg z < \frac{5\pi}{4} \tag{4.13}$$

where the first line corresponds to positive real arguments $z > 0$ and the second expression is valid for real negative arguments $z < 0$. Focussing for simplicity only on the limit $k \to +\infty$, the determinant yields

$$(E + V_0) \left(\frac{e^{-k^2}}{\sqrt{2}k} - \frac{\sqrt{2\pi}}{\Gamma(1 - p)} e^{i\pi p} \right) + (E - V_0) \left(-\frac{e^{-k^2}}{\sqrt{2}k} - \frac{\sqrt{2\pi}}{\Gamma(p)} e^{i\pi p} \right) = 0. \tag{4.14}$$

when inserting the asymptotic formula for large positive arguments from above. The quantity p here has the value $p = (E + V_0)^2$ since for positive k, the negative x-region has to be considered. Further analysis shows that there are only small corrections that exponentially depend on k, namely

$$\delta_0 = \frac{V_0 e^{-k^2}}{k}, \; \delta_n = \frac{n(1 + 2V_0)e^{-k^2}}{\sqrt{2}k(1 + 2nV_0)n!} \tag{4.15}$$

where the first value is the correction of the zeroth and the second is the correction of the nth Landau level. Analogously also for negative k values, finally exactly the shifted Landau levels are obtained as

$$E_{n,|k| \to \infty} \simeq -\text{sgn}(k)V_0 + \text{sgn}(n)\sqrt{|n|}. \tag{4.16}$$

Each level with a fixed band index n is continuously connected between these two flat asymptotic values and thus for $V_0 > 0$ there is always the $n = 0$ level that crosses $E = 0$ at the position $k = 0$. Additionally, when the $n = \pm 1$ levels cross zero energy there will be two additional modes that cross $E = 0$ at finite k, and so on, resulting in an odd number of such modes which in fact correspond to the chiral interface states, for non-zero potential.

This continuity of the levels also leads to a closing of the gaps between neighbouring levels with

increasing potential: Already for $V_0 = 0.5$ the $n = \pm 1$ levels for $k \to \pm\infty$ align with the $n = 0$ level in the limit $k \to \mp\infty$ and thus the spectrum becomes gapless for any larger values of V_0.

4.1.3 PROPERTIES OF CHIRAL INTERFACE STATES

Furthermore, the chiral interface states can be analysed in more detail. From their slope, one can calculate the velocity with which they travel along the y-axis as

$$\frac{v_{n,k}}{v_F} = \sqrt{2}\frac{\partial E_{n,k}}{\partial k} = -\sqrt{2}\left(\frac{\partial_k \Delta_k(E)}{\partial_E \Delta_k(E)}\right)_{E=E_{n,k}}. \tag{4.17}$$

For the $n = 0$ mode this velocity can even be evaluated analytically around the position $E = 0 = k$: First of all, the parabolic cylinder functions are expanded to lowest order in their argument q as

$$D_p(q) \approx \frac{2^{\frac{p}{2}}\sqrt{\pi}}{\Gamma\left(\frac{1}{2} - \frac{p}{2}\right)} - \frac{2^{\frac{p+1}{2}}\sqrt{\pi}}{\Gamma\left(-\frac{p}{2}\right)}q \, , q \ll 1. \tag{4.18}$$

Next, this expression is inserted into the condition (4.11) and since considering small energies, $E \ll V_0$ is assumed and hence the simplification $(V_0 \pm E)^2 \approx V_0^2 \pm 2EV_0$ is implemented. With the Taylor series of the form $\Gamma(a \pm bE) \approx \Gamma(a) \pm \Gamma'(a)bE$, where a, b are functions of V_0, and some algebra, this results in

$$\begin{aligned}\frac{v_s}{v_F} &= \frac{\sqrt{2\pi}\, 2^{V_0^2}V_0\Gamma(1 - V_0^2)}{1 + V_0^2[\psi(1 - V_0^2/2) - \psi(1/2 - V_0^2/2)]} \\ &\times \left(\frac{1}{\Gamma^2(1/2 - V_0^2/2)} - \frac{1}{\Gamma(-V_0^2/2)\Gamma(1 - V_0^2/2)}\right)\end{aligned} \tag{4.19}$$

where $\Gamma(z)$ is the Gamma function and the Digamma function is $\psi(z) = d\ln\Gamma/dz$. This result is shown in figure 4.3 and defined as $v_s = -v_{n=0,k=0}$. The velocity first grows quickly with increasing potential strength V_0 and then develops an oscillatory behaviour that seems to be damped. The steep increase for the small $V_0 \ll 1$ limit is given by $v_s = (2/\sqrt{\pi})V_0 l_B$. This value is identical to the velocity of a classical particle caused by the drift force resulting from a crossed magnetic and electric field ($E \times B$-drift) and represented by the blue dashed line. For the opposite limit $V_0 \gg 1$ the oscillations seem to die out and converge to a certain value. It is depicted by the dotted red line and is given by $v_s = (2/\pi)v_F$. This value corresponds to the semiclassical expectation for a situation where a pure snake trajectory built from alternating semi-circles occurs caused by perpendicular incidence of the Dirac fermions on the interface [123–125]. The slopes of the central state around $E = k = 0$ that have been gained from linear regression fitted to the spectra in figure 4.2 for the three values $V_0 = 0.6$ (1.2, 2.4) of the potential strength yield values of $v_s/v_F \simeq 0.76$ (0.65, 0.63), respectively, in very good agreement with the result in equation
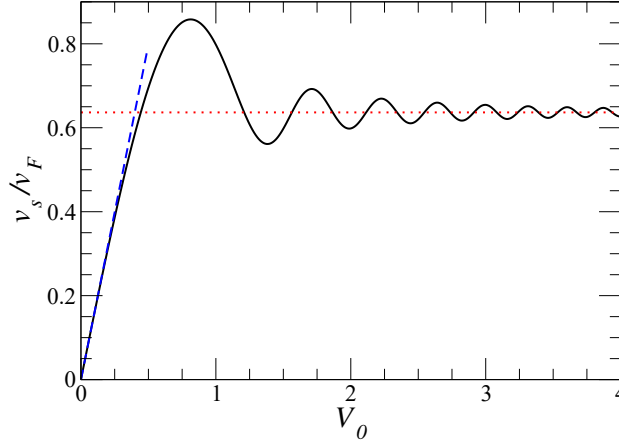
Figure 4.3: Velocity $v_s = -v_{n=0,k=0}$ of the central chiral interface state around $E = 0$ depending on the potential strength V_0. The analytical result from Eq. (4.19) is depicted as the black solid line while the dashed blue line gives the drift velocity $v_s/v_F = 2\sqrt{2/\pi}V_0$ predicted for the limit of a small potential step $V_0 \ll 1$ and the dotted red line represents the limit of large V_0 where $v_s/v_F = 2/\pi \simeq 0.63$. [132]

(4.19). In addition, such fits have also been extracted for the large energy range of the spectra since not only the regime $|E| \lesssim 1$ but also the range with $|E| \gtrsim 1$ shows linear behaviour but with a different slope. For this region values of $v_\infty/v_F \simeq 0.95$ (0.92, 0.82) have been found which is in accordance with the expectation that $v_\infty \to v_F$ for $|E| \gg V_0$ [63].

Also the oscillation as a function of $V_0/E_B \sim V_0\sqrt{B}$ visible in figure 4.3 itself is noteworthy since its extrema take place for special values of the potential strength, namely $V_0 = \sqrt{N}$ with N being a natural number. For exactly these specific values an analytical treatment of the matching condition (4.11) for zero energy is possible since then the index p reduces to the integer values $p = N$ and hence the parabolic cylinder functions can be simplified using the Hermite polynomials $H_N(z)$ as [102]

$$D_N(q) = -2^{N/2}e^{-q^2/4}H_N(q/\sqrt{2}). \tag{4.20}$$

With this, one can show that there are $2N - 1$ solutions of the matching equation $\Delta_k(E = 0) = 0$ at values $k = \{0, \pm k_1, \ldots, \pm k_{N-1}\}$, where the k_i are given by the $N - 1$ positive zeroes of the Hermite polynomials $H_N(k)$. From this, one can derive the number of energy bands $E_{n,k}$ that cross $E = 0$ at a certain value k for a given potential within the range

$$\sqrt{N - 1} < V_0 \leq \sqrt{N} \tag{4.21}$$

to be $2N - 1$. This prediction is consistent with the spectra for the three values of the potential strength where in figure 4.2 there are 1 (3, 11) states crossing zero energy in panel (a) ((b), (c)). Hence, for an arbitrary non-zero potential strength V_0 there will always be a chiral interface
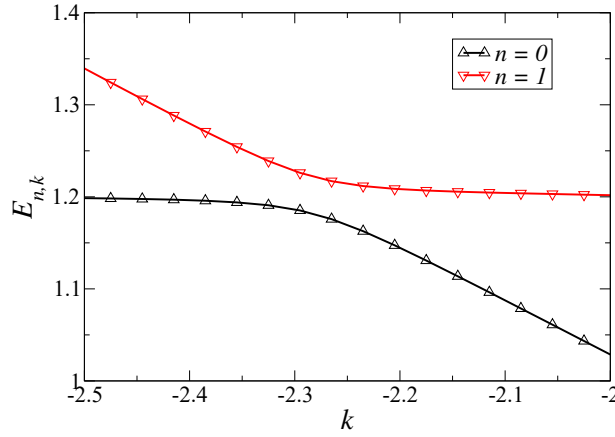
Figure 4.4: Zoom of the spectrum in figure 4.2 (b) for $V_0 = 1.2$ showing in more detail the avoided crossing between the energy levels with band indices $n = 0$ (black line, triangles up) and $n = 1$ (red, triangles down). The triangles mark the positions where values have numerically been calculated for the discrete k-grid.

state[4] – at least the one crossing the point $E = k = 0$.

But what exactly is such a chiral interface state? In the different panels of figure 4.2 several can be seen and as an example, the central one is always visibly enhanced utilizing the dashed red line. Nevertheless it should be regarded as a guide to the eye only, as it does not represent a true eigenstate for all values of k as it runs along different bands with different band indices n which are divided by avoided crossings which become smaller with higher potential strength V_0 and energy E. A closer picture of such an avoided crossing is shown in figure 4.4 on whose scale the different energy levels become distinguishable. The chiral interface state has a negative group velocity and consists of parts of approximately linear slope that have already been discussed for the central state before.

4.1.4 PROBABILITY DENSITY

After calculating the eigenfunctions $\Psi_{n,k}(x,y)$ for a given energy $E_{n,k}$ from the matching condition and the normalization, also further quantities like the probability density $\rho_{n,k}(x)$ or the particle current density, or, to be more specific, its y-component $J_{n,k}(x)$ to the given eigenstate can be evaluated as

$$\rho_{n,k}(x) = \Psi_{n,k}^\dagger \sigma_0 \Psi_{n,k}, \quad J_{n,k}(x) = v_F \Psi_{n,k}^\dagger \sigma_y \Psi_{n,k}. \tag{4.22}$$

---

[4]This contradicts a statement in [128] where a vanishing of all states was predicted for V_0 larger than a certain threshold.
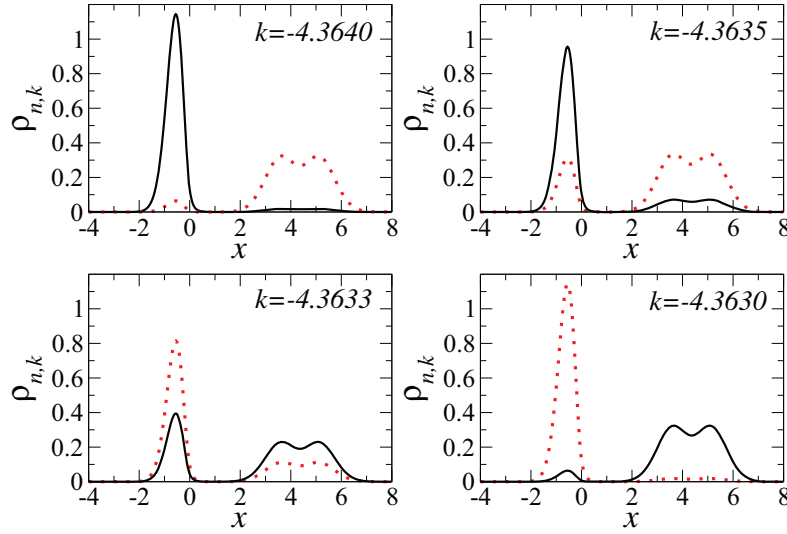
Figure 4.5: Probability density $\rho_{n,k}$ versus position x for different values of k around the avoided crossing of the $n = 0$ (black line) and $n = -1$ (dotted red curve) levels for $V_0 = 2.4$ indicated by the blue arrow in figure 4.2 (c). [132]

With these properties the different states and energy levels can be further analysed. For example, one of the already discussed avoided crossings has been considered in greater detail in figure 4.5. Here, the probability density for the two bands ($n = 0$ and $n = -1$) participating in the crossing has been depicted for different values of the wavenumber k in the range where the crossing takes place, namely for $-4.364 \leq k \leq -4.363$. In the first panel which means in the situation left of the crossing in figure 4.2 (c) the $n = -1$ band has the probability density form of a Landau level. This can be concluded from the fact that it is centered away from the interface and approximately around the expected value $\bar{x} = -k$. It corresponds to the flat dispersion left of the crossing. On the other hand, observing the $n = 0$ band, which comes down with a steep slope to join the other level in the avoided crossing considered, shows that it is located very close to the interface marking it as a chiral interface state. Throughout the evolution of the panels the states morph and exchange roles so that the interface state is furthermore carried by the $n = 0$ band which evolves right of the crossing with approximately the same slope as the $n = -1$ band had before while this band becomes a flat Landau-like level.

Furthermore, also the probability densities of other states have been observed and a choice is shown in the following: In figure 4.7 four states for $V_0 = 2.4$ and with energy $E = 0$ have been displayed which are indicated by the orange arrows in figure 4.2 (c) while the green arrows in this panel correspond to the four states investigated in figure 4.6 which have energy $E = 2$. These latter states can be seen to be centered on only one side of the interface and rather close to it – in fact, much closer than the corresponding Landau levels at $V_0 = 0$ would be, which are centered at $\bar{x} = -k \simeq +5.27, +4.48, +3.82$, and $+3.21$ for the chosen values. Hence, they
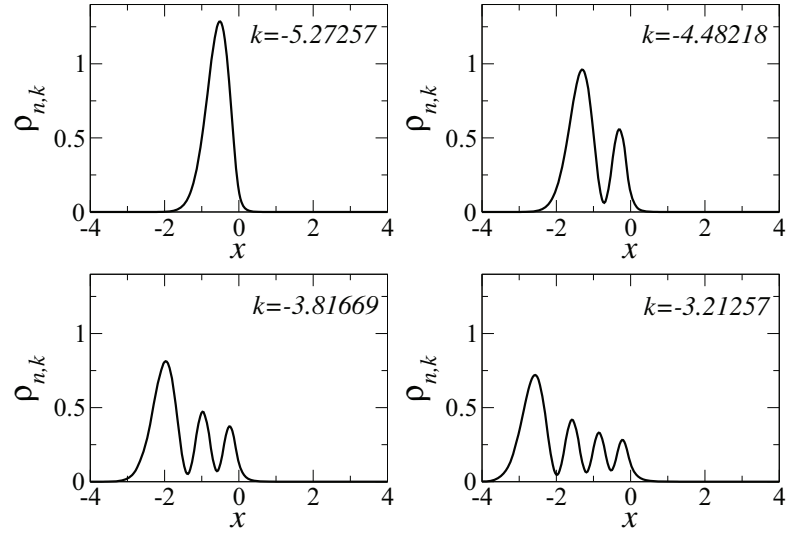
Figure 4.6: Probability density ρ_n, k depending on the position x for states taken at energy $E = 2$ and a potential strength of $V_0 = 2.4$ represented by green arrows in figure 4.2 (c). Different panels correspond to different wavenumbers k (given in the panel) and corresponding band indices. [132]

would be expected to be found on the other side with respect to the junction and also much further from it. Nevertheless, the shape of the probability density curves is very similar to that of Landau levels, to be more specific the state in panel 1 (2, 3, 4) corresponding to a wavenumber $k \simeq -5.27 (-4.48, -3.82, -3.21)$ resembles a Landau level with index $n = 0$ (1, 2, 3). A look at the spectrum in figure 4.2 (c) verifies that these states evolve to exactly the bulk Landau levels with the named band indices n when following the respective line through $n + 1$ avoided crossings to the limit $k \to -\infty$. To see this, one has to stick to one state/curve and not switch them according to the evolution of the chiral interface states. Thus, for example, the central chiral interface state (red dashed curve) that passes through $E = k = 0$ and there, of course, has a band index $n = 0$, corresponds for the here considered energy $E = 2$ to a band with index $n = 2$.

In the next picture, some of the $2N - 1 = 11$ modes crossing $E = 0$ for $V_0 = 2.4$ have been more closely considered. Obviously, these probability densities look different than the ones shown before: First of all, they have more peaks, which are less distinguishable, and, more importantly, they are not centred on only one side of the junction but have a finite probability on both sides which is even symmetric for $k = 0$ and becomes more asymmetric for larger values of k. Remembering that we consider a *p-n* junction at the position $x = 0$ this means that these states are carried by electrons (for $x < 0$) and holes (for $x > 0$) both. For the symmetric case for $k = 0$ the motion must consist of the same number of half circles on both sides (in the semi-classical picture) like it would be the case for a pure snaking state while for the other more asymmetrical situations the state behaves like an edge state consisting mostly of skipping orbits. These states shown in figure 4.7 represent special features of the Dirac fermions in graphene which will be
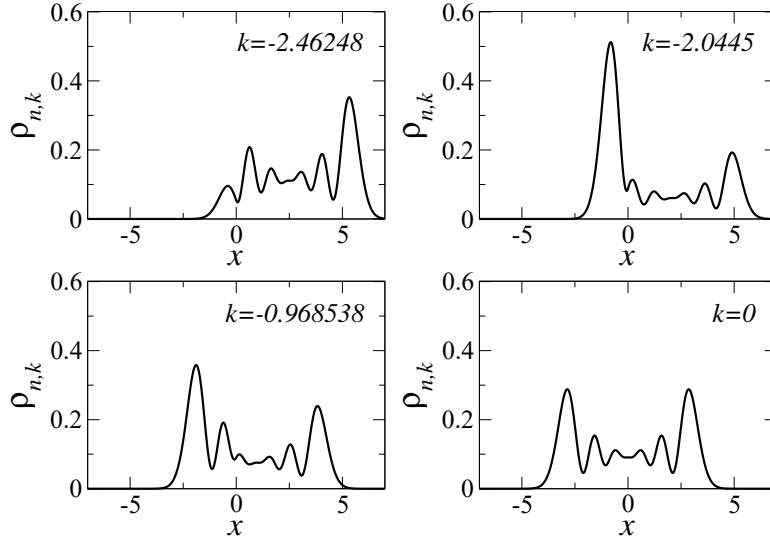
Figure 4.7: The same quantities as in figure 4.6 are depicted but here the eigenstates are taken at energy $E = 0$ and are indicated by the orange arrows in figure 4.2 (c). [132]

highlighted by contrasting this version with the analogous problem of Schrödinger fermions as they would be present for example in a conventional two-dimensional electron gas [133].

4.1.5 COMPARISON WITH 2DEG

Also for this setup, a straight *p-n* junction at the position $x = 0$ is inflicted, i.e. the potential is again given as $V(x) = V_0 \mathrm{sgn}(x)$ and using the Landau gauge leads to $(A_x, A_y) = (0, Bx)$ as before. With the translational invariance in y-direction, the wave functions can be factorized as above as $\Psi_k(x, y) = e^{iky}\psi_k(x)$ where $\psi_k(x)$ now is a one-dimensional scalar wave function. With $q = \sqrt{2}(x + k)$ and the ladder operators $a = \partial_q + q/2$ and $a^\dagger = -\partial_q + q/2$ defined as before, the Schrödinger equation takes the form

$$\left[a^\dagger a - \left(E - V(x) - \frac{1}{2} \right) \right] \psi_k(x) = 0. \tag{4.23}$$

Energies are now measured in terms of the cyclotron energy defined as $\omega_c = eB/(mc)$ and lengths as before in units of the magnetic length l_B. Considering the two regions with constant potential $V(x) = V = \pm V_0$ on both sides of the interface, the solutions to this equation are given by parabolic cylinder functions $D_p(\pm q)$ with the index $p = E - V - 1/2$ and in general the eigenstates follow as linear combinations of the wave functions $\psi_{k,V}^{(1,2)}(x) = D_p(\pm\sqrt{2}(x + k))$. For a uniform potential without the here considered step, the requirement of normalizability would imply integer values of the index p according to $p = N = 0, 1, 2, ...$ resulting in standard
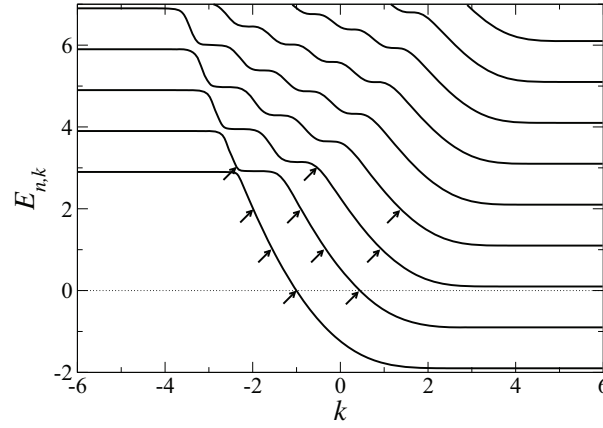
Figure 4.8: Energy spectrum $E_{n,k}$ (in units of the cyclotron energy ω_c) depending on the wavenumber k (in l_B^{-1}) for Schrödinger fermions in a straight *p-n* junction for a potential strength $V_0/\omega_c = 2.4$. Black arrows point out states for which density profiles are shown in figure 4.9. [132]
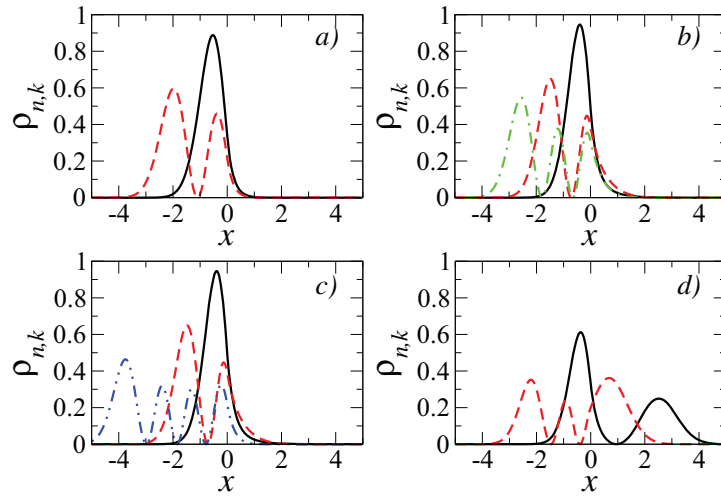
Figure 4.9: Probability densities $\rho_{n,k}$ vs position x for the Schrödinger version of a *p-n* junction with strength $V_0/\omega_c = 2.4$. Each panel illustrates profiles for states with different values of k at the same energy $E_{n,k}$ as indicated by arrows in figure 4.8, in detail: a) Energy $E_{n,k} = 0$ with $k = -1.00205$ (black solid) and $k = 0.445883$ (red dashed), b) $E_{n,k} = 1$ with $k = -1.54421$ (black solid), $k = -0.322044$ (red dashed), and $k = 0.953544$ (green dot-dashed), c) $E_{n,k} = 2$ with $k = -1.99022$ (black solid), $k = -0.899269$ (red dashed), and $k = 1.37079$ (blue dot-dashed), and d) $E_{n,k} = 3$ with $k = -2.35387$ (black solid) and $k = -0.519357$ (red dashed). [132]

Landau energy levels $E = N + 1/2 + V$ shifted by V. Whereas for the situation considered for the junction, the normalizable eigenstates can be written as

$$\psi_k(x) = \begin{cases} c_< \psi^{(2)}_{k,-V_0}(x), & x < 0, \\ c_> \psi^{(1)}_{k,+V_0}(x), & x > 0 \end{cases} \tag{4.24}$$

with coefficients $c_{</>} = \mathcal{N} D_{E_{n,k} \mp V_0 - 1/2}(\pm\sqrt{2}k)$ including a general normalization constant $\mathcal{N}$.

At the interface at $x = 0$, both the wave function $\psi_k(x)$ itself and its spatial derivative $\psi_k'(x)$ have to be continuous and thus the matching condition reads

$$\Delta^{(S)}_k(E) = \det \begin{bmatrix} \psi^{(2)}_{k,-V_0}(0) & -\psi^{(1)}_{k,V_0}(0) \\ \psi^{(2)}_{k,-V_0-1}(0) & \psi^{(1)}_{k,V_0-1}(0) \end{bmatrix} = 0 \tag{4.25}$$

using the recurrence relations of the parabolic cylinder functions [102]. The numerically determined solutions of this condition yield the spectrum $E_{n,k}$ that is shown in figure 4.8 for $V_0 = 2.4$ (in the here used energy unit ω_c). This spectrum does not exhibit the same anti-symmetry as the one for the Dirac case but it also reveals the flat regions towards large $|k|$ values that represent the bulk Landau levels. In addition, one also observes avoided crossings and regions of linear dispersion that can be interpreted as chiral interface states.

Figure 4.9 shows the probability density profiles $\rho_{n,k}$ for the states indicated by arrows in figure 4.8 which have an approximately constant slope. All of the densities in panels a)-c) are non-zero only on one side of the junction (also those taken at energy $E_{n,k} = 0$ in contrast to the Dirac version) and display on the other side only a weight which is exponentially small. Only for the states in panel d), there are parts of the probability density on both sides. This corresponds to the observation from the spectrum that these states are in the vicinity of regions with a flat dispersion and hence can be interpreted as Landau like states coexisting with chiral interface states while the states considered in the other three panels are taken from places with mostly linear dispersion and hence can be thought of as the skipping orbit edge state-type of a chiral interface state interpreting the interface as a boundary. Nevertheless, there are no states like the one in the Dirac picture which crosses the $E = k = 0$ point with linear dispersion and equal weight of the probability density on both sides of the junction.

4.1.6 CURRENT DENSITY

Returning to the Dirac fermionic case of graphene and a quantity which has already been mentioned but not yet treated, namely the particle current density $J_{n,k}(x)$, this quantity is depicted in figure 4.10 for a potential strength $V_0 = 0.6$ (compare figure 4.2 (a)), displaying only the $n = 0$ states for different values of the wavenumber k. For $k = 0$, the curve shows a
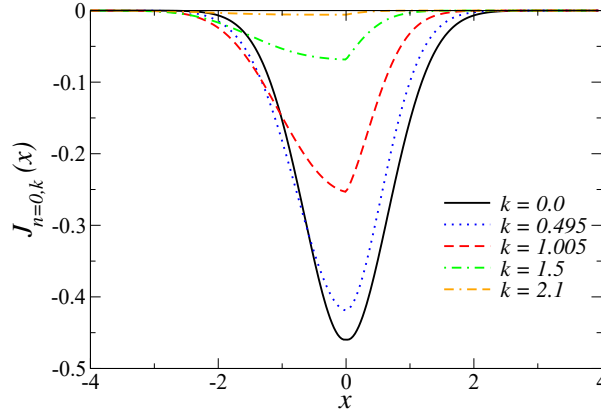
Figure 4.10: Profile of the particle current density $J_{n,k}(x)$ plotted against the position x for the eigenstates of the band with index $n = 0$ and several values of k as indicated in the legend. The potential strength of the straight *p-n* junction is given as $V_0 = 0.6$. [132]

symmetric behaviour with the maximum absolute value at $x = 0$, i.e. it satisfies the symmetry relation $J_{0,0}(x) = J_{0,0}(-x)$. Furthermore, one can inspect the current belonging to a certain eigenstate which can be obtained by integrating over the transverse direction x and reads [63]

$$I_{n,k} = \int_{-\infty}^{\infty} dx J_{n,k}(x) = v_{n,k}. \tag{4.26}$$

Here, one can see that the current $I_{0,0}$ for the state in band $n = 0$ with $k = 0$ is proportional to the velocity v_s defined before. Also in figure 4.10 the maximum value for the current $|I_{0,k}|$ is reached for $k = 0$. If one increases the wavenumber, this absolute value of the current decreases until it reaches the limit $|k| \gg V_0$ where the bulk Landau levels occur and it becomes exponentially small. Furthermore, during this process the profile becomes more and more asymmetric although it keeps its peak around the position of the interface, i.e. in the vicinity of the position $x = 0$. Nevertheless, the corresponding probability density $\rho_{0,k}(x)$ moves further away from the interface with increasing $|k|$. The entire current for a certain chemical potential is obtained by summing and integrating the current for each state as $\sum_n \int dk \, I_{n,k} f(E_{n,k} - \mu)$ where $f(E)$ is the Fermi function.

4.2 CIRCULAR *P-N* JUNCTION

For the circularly symmetric case schematically shown in figure 4.1 (b) where R is the disc radius, it is helpful to employ polar coordinates (r, φ) with the radial distance given as $r = \sqrt{x^2 + y^2}$ and the angle φ in x-y-plane. Experimentally this geometry has received a lot of

interest and such settings have already been realised creating the circular potential using various methods such as gating with top and bottom electrodes that can be put on different potentials [40, 46], by utilizing scanning tunneling microscopy tips which themselves alter the potential already in a circularly geometric fashion [37], or via local manipulating defect charges within the underlying substrate beneath the sample [42].

4.2.1 Model

The step-like potential

$$V(x, y) = V_0 \mathrm{sgn}(r - R) \tag{4.27}$$

is considered and the magnetic field will again be encoded in the vector potential (A_r, A_φ). In order to sustain the rotational symmetry, the symmetric gauge is chosen, namely $(A_r, A_\varphi) = (0, Br/2)$. Only small changes would be necessary to adjust this description to handle the pseudo-magnetic fields that arise in graphene due to strain also in this case. With these ingredients, the Hamiltonian from equation (4.1) is set up and the Dirac equation will be solved by spinor eigenstates of the form [80, 134]

$$\Psi_{n,j}(\xi, \varphi) = \frac{\xi^{|j+\frac{1}{2}|/2} e^{-\xi/2}}{\sqrt{2\pi}} \begin{pmatrix} e^{i(j-\frac{1}{2})\varphi} \phi_{n,j}(\xi) \\ i e^{i(j+\frac{1}{2})\varphi} \chi_{n,j}(\xi) \end{pmatrix} \tag{4.28}$$

where $\xi = r^2/2$ (or $\xi_0 = R^2/2$ for the position of the interface, respectively) is used instead of the normal radial component r for convenience. The solutions are labelled using the indices n, j with the integer band index n which simply counts the different solutions to a given value of the conserved and half-integer valued angular momentum j. The angular momenta of the two spinor components differ by one as a result of the factorized phase φ and contain the radial functions $\phi_{n,j}(\xi)$ and $\chi_{n,j}(\xi)$. They fulfil the normalization condition

$$\int_0^\infty d\xi \, \xi^{|j+\frac{1}{2}|} e^{-\xi} \left(|\phi_{n,j}|^2 + |\chi_{n,j}|^2 \right) = 1. \tag{4.29}$$

and their explicit form is given in terms of different types of the confluent hypergeometric function, namely $\Phi(\alpha, \gamma; \xi)$ and $\Psi(\alpha, \gamma; \xi)$ [102] for regions of constant V. Here,

$$\Psi(\alpha, \gamma; \xi) = \frac{\Gamma(1-\gamma)}{\Gamma(\alpha-\gamma+1)} \Phi(\alpha, \gamma; \xi) + \frac{\Gamma(\gamma-1)}{\Gamma(\alpha)} \xi^{1-\gamma} \Phi(\alpha-\gamma+1, 2-\gamma; \xi) \tag{4.30}$$

is a linear combination of the two solutions

$$\Phi(\alpha, \gamma; \xi) \text{ and } \xi^{1-\gamma} \Phi(\alpha-\gamma+1, 2-\gamma; \xi) \tag{4.31}$$

which solve the differential equation of the form

$$\left[\xi \frac{d^2}{d\xi^2} + \frac{d}{d\xi} + \left(\beta - \frac{m^2}{4\xi} - \frac{\xi}{4} \right) \right] \phi_j = 0 \tag{4.32}$$

that follows from the Dirac equation with $m = |j| + 1/2$. The variables α, β, γ are functions of the different parameters. Explicitly, the wave functions follow as [80, 134]

$$\begin{pmatrix} \phi_j \\ \chi_j \end{pmatrix} = c_< \Theta(\xi_0 - \xi) \begin{pmatrix} \frac{m}{\sqrt{\xi}} \Phi \left(m - (E + V_0)^2, m; \xi \right) \\ (E + V_0) \Phi \left(m - (E + V_0)^2, 1 + m; \xi \right) \end{pmatrix}$$
$$+ c_> \Theta(\xi - \xi_0) \begin{pmatrix} \frac{E - V_0}{\sqrt{\xi}} \Psi \left(m - (E - V_0)^2, m; \xi \right) \\ \Psi \left(m - (E - V_0)^2, 1 + m; \xi \right) \end{pmatrix}. \tag{4.33}$$

for positive angular momenta, i.e. $j > 0$ with the Heaviside step function $\Theta(x)$ and the complex coefficients $c_{</>}$ whereas they read

$$\begin{pmatrix} \phi_j \\ \chi_j \end{pmatrix} = c_< \Theta(\xi_0 - \xi) \begin{pmatrix} \sqrt{\xi}(E + V_0) \Phi \left(1 - (E + V_0)^2, 1 + m; \xi \right) \\ -m \Phi \left(-(E + V_0)^2, m; \xi \right) \end{pmatrix} \tag{4.34}$$
$$+ c_> \Theta(\xi - \xi_0) \begin{pmatrix} \sqrt{\xi}(E - V_0) \Psi \left(1 - (E - V_0)^2, 1 + m; \xi \right) \\ \Psi \left(-(E - V_0)^2, m; \xi \right) \end{pmatrix}.$$

for $j < 0$. For these states, the solution $\Psi(\alpha, \gamma; \xi)$ has been discarded in the inner region of the disc, i.e. for $\xi < \xi_0$ since it is not regular at the origin $\xi = 0$, while for the outer region the requirement of normalizability forbids the solution $\Phi(\alpha, \gamma; \xi)$ since for large ξ

$$\Phi(\alpha, \gamma; \xi) = 1 + \frac{\alpha}{\gamma} \frac{\xi}{1!} + \frac{\alpha(\alpha + 1)}{\gamma(\gamma + 1)} \frac{\xi^2}{2!} + \frac{\alpha(\alpha + 1)(\alpha + 2)}{\gamma(\gamma + 1)(\gamma + 2)} \frac{\xi^3}{3!} + \dots \tag{4.35}$$

behaves like $\Phi \sim e^\xi$.

Exploiting again the continuity of the wavefunction at the interface, i.e. for $\xi = \xi_0$, delivers another matching and hence an energy quantization condition which reads

$$(E - V_0) \left[1 - \frac{d}{d\xi} \ln \Phi \left(m - (E + V_0)^2, m; \xi \right) \Big|_{\xi = \xi_0} \right]$$
$$= (E + V_0) \left[1 - \frac{d}{d\xi} \ln \Psi \left(m - (E - V_0)^2, m; \xi \right) \Big|_{\xi = \xi_0} \right], \tag{4.36}$$

for positive j and

$$(E - V_0) \frac{d}{d\xi} \ln \Phi \left(-(E + V_0)^2, m; \xi \right) \Big|_{\xi = \xi_0} = (E + V_0) \frac{d}{d\xi} \ln \Psi \left(-(E - V_0)^2, m; \xi \right) \Big|_{\xi = \xi_0}. \tag{4.37}$$

for $j < 0$.

4.2.2 ENERGY SPECTRUM

𝔚ith the help of these equations the energy spectrum can be determined numerically and an example is shown in figure 4.11. Without a potential, i.e. for $V_0 = 0$, there is an analytical way to determine this spectrum: For this case, only the solution proportional to $\Phi(\alpha, \gamma; \xi)$ can be kept (again due to the fact that $\Psi(\alpha, \gamma; \xi)$ is not regular at the origin) and since normalizability is still required, the behaviour of Φ for large ξ leads to a constraint regarding the parameter α, namely that it has to equal a negative integer, $\alpha = -n$ with $n = 0, 1, 2, \dots$. With this, the spectrum follows as

$$E_{n,j}^{(0)} = \text{sgn}(n)\sqrt{|n|}, \quad |n| = n_r + (j + 1/2)\Theta(j), \tag{4.38}$$

with $n_r \geq 0$ being the radial quantum number. This corresponds to a spectrum with flat Landau levels for negative values of j, which is effectively independent of j, while the region with positive j exhibits a square root-shaped dispersion according to $E_{n,j>0}^{(0)} \sim \sqrt{j}$ for a fixed n_r.

On the other hand, for finite V_0, as shown in figure 4.11 for $V_0 = 0.6$ in the main panel and $V_0 = 1.2$ in the inset, the shape of the curve for $j > 0$ doesn't change much except for the fact that it experiences a global energy shift of potential strength V_0 that follows from the positive potential outside the disk (i.e. for $r > R$), resulting in $E_{n,j \gg 1} \approx V_0 + E_{n,j}^{(0)}$. At the same time, there is a substantial change for the energies with negative j: The formerly flat Landau levels don't stay dispersionless any longer and especially the $n = 0$ level develops a pronounced dependence on the angular momentum j. One can determine the maximum value of the negative slope for the different potential strengths considered here which is situated at $j = -11/2$ for $V_0 = 0.6$
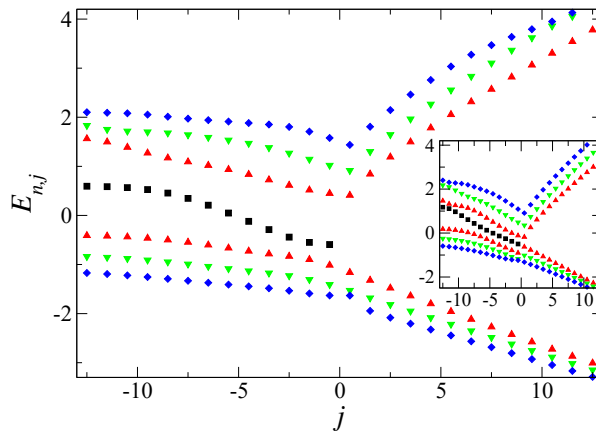
Figure 4.11: Dependence of the energy spectra $E_{n,j}$ on the angular momentum j for a circularly shaped *p-n* junction with radius $R = 3.3$. The different colours and symbols stand for the different (integer) values of the radial quantum number $n_r = |n| - (j+1/2)\Theta(j) = 0, 1, 2, 3$. The potential strength is given by $V_0 = 0.6$ in the main panel and $V_0 = 1.2$ in the inset. [132]

and at $j = -17/2$ for $V_0 = 1.2$. This result has a direct connection to the ring current which will flow unidirectionally around the *p-n* disk.

4.2.3 RING CURRENTS

The current density of this current is given by

$$J_{n,j}^{(\varphi)}(r) = v_F \Psi_{n,j}^\dagger \begin{pmatrix} 0 & -ie^{-i\varphi} \\ ie^{i\varphi} & 0 \end{pmatrix} \Psi_{n,j} \tag{4.39}$$

belonging to a certain eigenstate $\Psi_{n,j}(r,\varphi)$ which carries the current, runs in the azimuthal direction while the radial component of the current density vanishes. The $n = 0$ eigenstates $\Psi_{0,j<0}$ exhibit a maximum in the corresponding probability density $\rho_{0,j}(r)$ for potential strengths below unity ($V_0 \simeq 1$) for the values $r = R$ and the half-integer valued $j = j_0 \approx -R^2/2$. If V_0 becomes larger, there are oscillations around the position of the disk radius for both the probability density and the current density. For some (negative) values of the angular momentum j of the $n = 0$ states, figure 4.12 shows the dependence of the current density on the radial coordinate r. The circulating current follows as

$$I_{n,j} = \int_0^\infty dr\, J_{n,j}^{(\varphi)}(r). \tag{4.40}$$
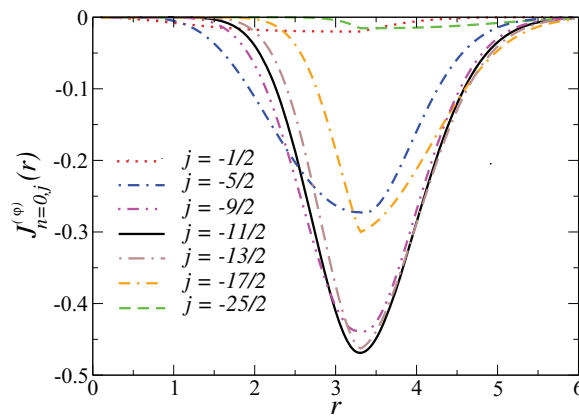
Figure 4.12: Dependence of the azimuthal current density $J_{n,j}^{(\varphi)}(r)$ for the $n = 0$ states on the radial distance r from the center of the circular *p-n* junction in units of l_B. Results are shown for a radius of $R = 3.3$, a potential strength of $V_0 = 0.6$ and several values of $j < 0$. [132]

There is also a second way to express the current which is by exploiting its connection to the dispersion relation – analogously as to the case of the straight junction, again it can be written as derivative, this time with respect to the angular momentum for a fixed value of n_r and it reads

$$I_{n,j} = \frac{\sqrt{2}}{2\pi} \partial_j E_{n,j}.$$

(4.41)

From this equation that directly relates the resulting current carried by an eigenstate to the dependence of the respective eigenenergy on the angular momentum, it is obvious that for $n = 0$ the magnitude of the current will be maximal for the already discussed state with $j = j_0 < 0$ with the steepest slope $\partial_j E_{0,j}$. Hence, it should lead to maximally enhanced ring currents caused by chiral interface states if there is an alignment of the Fermi energy with this respective energy E_{0,j_0}. For the flat bands of the dispersion, for negative j and a vanishing potential $V_0 = 0$, this current is obviously given as $I_{0,j<0}^{V_0=0} = 0$ (explanation as in the previous chapter 3) whereas for small but finite V_0 the current is obtained as

$$I_{0,j<0} = \frac{v_F V_0}{l_B E_B} C_{0,j}(\xi_0) + \mathcal{O}(V_0^2).$$

(4.42)

The coefficients $C_{0,j}$ are dimensionless and can be obtained via perturbation theory while the prefactor results from restoring the different units (namely length l_B and energy E_B) in order to clarify that the strength B of the magnetic field enters the ring current solely due to the coefficients depending on the magnetic flux $\xi_0 = 1/2(R/l_B)^2$ through the n-doped region. There are two ways that yield these coefficients: Either they can be calculated analytically using perturbation theory as shown in the next paragraph, or numerically from (4.41). They show a peak for the special value of the angular momentum $j = j_0$ with a maximum value of $|C_{0,j_0}| \approx 0.25/\sqrt{2\xi_0} = 0.25 l_B/R$ and they are negative.

For small potential strengths, the potential can be written as $V(r) = V_0 + V^{\text{pert}}(r)$ where $V^{\text{pert}}(r) = -2V_0\Theta(R - r)$ is considered as a small perturbation which does not couple states that possess different angular momenta. Thus, the Landau levels with $n = 0 = n_r$ and $j < 0$ experience the correction

$$\begin{pmatrix} \phi_{0,j}^{\text{pert}}(\xi) \\ \chi_{0,j}^{\text{pert}}(\xi) \end{pmatrix} = \frac{\sqrt{2}}{N_{0,j}} \begin{pmatrix} 0 \\ 1 \end{pmatrix} + \sum_{n\neq 0} \frac{\langle n,j|V^{\text{pert}}|0,j\rangle}{-\text{sgn}(n)\sqrt{|n|}N_{n,j}}$$
$$\times \begin{pmatrix} \frac{-\text{sgn}(n)\sqrt{|n|}\xi}{m}\Phi(-|n|+1, m+1; \xi) \\ \Phi(-|n|, m; \xi) \end{pmatrix}$$

(4.43)

of first order in V^{pert} with $N_{n,j}^2 = 4\pi|n|![(m-1)!]^2/[(m+|n|-1)!]$ including $m = |j| + 1/2$, and $\xi = r^2/2$. Expressing the matrix elements of the perturbation via the basis of the unperturbed Landau levels using the notation $\{|n,j\rangle\}$ yields

$$\langle n,j|V^{\text{pert}}|0,j\rangle = -V_0 \frac{4\sqrt{2}\,\pi}{N_{0,j}N_{n,j}} \frac{\xi_0^m}{m} \Phi(|n|+m, m+1; -\xi_0).$$

(4.44)
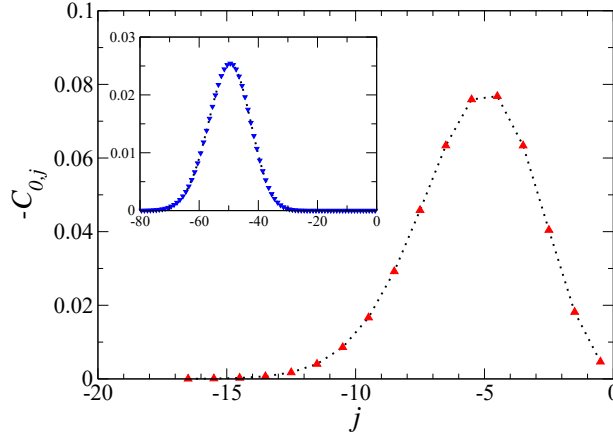
Figure 4.13: Dependence of the dimensionless coefficients $-C_{n=0,j<0}$ on the angular momentum j from perturbation theory up to first order. The disk radius of the circular *p-n* junction is $R = 3.3$ in the main panel and $R = 10$ in the inset. Dotted black lines are merely meant to be guides to the eye. [132]

Using the physical units instead of dimensionless ones, the integrated current to lowest order reads

$$
\begin{aligned}
I_{0,j<0} &= v_F \int_0^\infty dr\ \Psi_{0,j}^{\text{pert}\dagger} \begin{pmatrix} 0 & -ie^{-i\varphi} \\ ie^{i\varphi} & 0 \end{pmatrix} \Psi_{0,j}^{\text{pert}} \\
&= \frac{v_F V_0}{l_B E_B} C_{0,j} + \mathcal{O}(V_0^2),
\end{aligned}
\tag{4.45}
$$

and performing the integral over the radial coordinate yields the coefficients

$$
C_{0,j}(\xi_0) = -\frac{\sqrt{2}}{\pi} \frac{\xi_0^m}{\Gamma(m+1)} \sum_{n=1}^\infty \frac{\Phi(n+m, m+1, -\xi_0)}{n}.
\tag{4.46}
$$

These are shown in figure 4.13. Obviously, the curves shown for different values of the disk radius R reveal maxima for half-integer values around the predicted value $j = j_0 \approx -R^2/2 \approx -5.5$ for $R = 3.3$ and -50 for $R = 10$.

The quantum-mechanical persistent current which flows though a ring of the radius R in equilibrium in the presence of a magnetic flux presents a good measure with which the current resulting from the present setup can be compared. Such a mesoscopic persistent current exhibits a maximum value of $I^{(pc)} = v_F/(2\pi R)$ and depends in an oscillatory manner on the strength of the magnetic field [135–138]. In contrast, the maximum current for the present situation is reached for $j = j_0$ and with the respective value for the coefficient, the estimate results in

$$
\frac{|I_{0,j_0}|}{I^{(pc)}} \approx \frac{\pi}{2} \frac{V_0}{E_B}.
\tag{4.47}
$$

These ring currents I_{0,j_0} and the thereby generated magnetic moments caused by chiral interface states will be experimentally measurable for not too small values of the ratio V_0/E_B. In the case of the persistent current, SQUID techniques (compare [139] and section 2.8.11) have been used. For the *p-n* disk considered here, current density profiles like those depicted in figure 4.12 could be experimentally measured using the techniques explained in [49, 140] if the energy $E_{n,j}$ is aligned with the Fermi energy. Induced by the chiral interface states which circulate around the disk, these densities show maxima around the radial position $r = R$. Nevertheless, this feature is only clearly visible for a not overly large potential strength since for $V_0 \gtrsim 1$, there are oscillations to be observed rather than clear peaks. By integrating one of these curves of the current density, the entire current $I_{0,j}$ can be obtained. By means of measuring the resulting ring currents for different values assigned to the Fermi energy, it might be possible to distinguish between different quantum states labelled by the angular momentum j.

4.3   Conclusions

Summarizing the findings of this chapter, two different geometries for *p-n* junctions in graphene, namely a straight and a circularly shaped potential step have been analysed and the resulting interface states in a perpendicular magnetic field have been studied.

For the straight junction with a height of the potential step of $2V_0$, there is always at least one interface state which crosses – for the symmetric situation considered – the point $E = k = 0$ and whose group velocity is given by the $E \times B$ drift velocity for small potential strengths. However, for larger values of V_0 this velocity oscillates as a function of V_0 and finally approaches the semiclassical velocity $2v_F/\pi$ of a snaking state. Furthermore, when the bulk Landau levels cross from positive to negative energies or vice versa due to the shift caused by V_0, always a pair of interface states at finite k is added, resulting in an odd number of these modes. A comparison of the Dirac case in graphene to a Schrödinger version as it would be present in a 2DEG has revealed that modes of edge-state type which move via skipping orbits can be found in both situations while modes with also snaking behaviour exist only in the case of Dirac fermions.

Also for the circular case, there are chiral interface states which depend on the potential strength V_0 and also the disk radius R which determines the angular momentum j_0 for which the circular current is maximal. The current is also localized close to the *p-n* interface. In the $n = 0$ Landau level, a finite potential can cause a chiral interface mode which induces a measurable magnetic moment whose value could even be larger than the one for a persistent current within a similarly sized quantum ring.

Graphene with proximity-induced pairing

Another promising experimental setup is to combine graphene with a layer of a superconducting material thus creating an external proximity-induced pairing gap Δ. One may expect that such a gap cannot coexist with a magnetic field B, which in this setup is assumed to be homogeneous and perpendicular to the plane of the graphene sheet, since these effects tend to annihilate each other. Here, however, a material is considered which has a sufficiently high critical field allowing for a coexistence of both phenomena. Furthermore, the geometry is important: Whereas in a three-dimensional bulk BCS superconductor the Meissner effect discussed in chapter 2.8.3 will push out a magnetic field, the usage of a thin superconducting layer should make the observation of the interesting regime where both effects occur, possible. It has been demonstrated for graphene [52–54] (and other two-dimensional electron gases [141]) that especially superconductivity that is induced due to the proximity effect[1] is able to coexist with magnetic fields of a magnitude high enough that Landau quantization is achieved. The results following in this chapter are mainly presented in [144].

---

[1]This is necessary since intrinsic superconductivity predicted in [142, 143] was not found experimentally for graphene.

5.1 SETUP

There are several possibilities to realize a situation of a graphene sample with both a superconducting gap and a magnetic field. One alternative is the setting of a lateral interface between graphene and the superconductor, which allows for specular Andreev reflection where an electron is reflected as a hole under an inverted reflection angle and has been discussed in detail [5, 145–147]. The presented proposal for a hybrid structure, which is shown in figure 5.1, is started with a substrate of standard hexagonal boron nitride (h-BN) of a thickness of about $20\,\text{nm}$, then a thin layer of two to four monolayers of the superconducting material $NbSe_2$ is added. This is a two-dimensional so-called van der Waals superconductor which is appropriate to induce superconductivity in graphene [148] and able to develop interfaces of high quality with this material [50]. Furthermore, it has a high critical magnetic field with values of $B_c \approx 5T$ at temperatures of $T = 1K$ and keeps its superconducting properties even when reduced to a thickness of only a few monolayers. If tuning via gates is desirable, it is possible to add another monolayer of h-BN at the expense of reducing the proximity effect. On top of this stack, the graphene flake is positioned and in this case the option to add another layer of h-BN closing the structure was not taken to allow for probing for example via scanning tunnelling microscopy as indicated or utilizing a graphite finger tip as demonstrated in [57]. Further opportunities to measure the different properties of this setup are given by transport experiments and the technique of locally manipulating the defect charges present in the substrate [42].
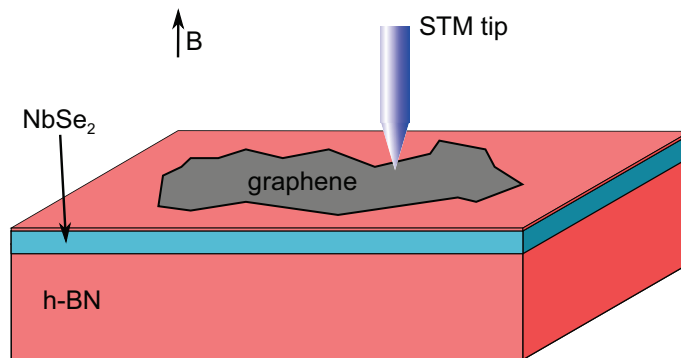
Figure 5.1: Schematic drawing of a vertical hybrid structure consisting of an h-BN substrate, a thin layer of $NbSe_2$ and another monolayer of h-BN which allows for gating the device. The graphene flake is deposited on top of this stack and can be probed using for example an STM tip. The entire structure is subject to a perpendicular magnetic field B. [144]

5.2   EXACT SOLUTION FOR V=0

Neglecting spin[2], the Bogoliubov-de Gennes Hamiltonian for the above described system can be written as [5, 145]

$$H = \begin{pmatrix} v_F \left(\hat{\boldsymbol{p}} + \frac{e}{c}\boldsymbol{A} \right) \cdot \boldsymbol{\sigma} + V & \Delta \\ \Delta^* & -v_F \left(\hat{\boldsymbol{p}} - \frac{e}{c}\boldsymbol{A} \right) \cdot \boldsymbol{\sigma} - V \end{pmatrix}, \tag{5.1}$$

where the Fermi energy E_F or chemical potential μ, respectively, is absorbed into the potential V as $V - \mu \to V$. The Pauli matrices $\sigma_{x,y}$ refer to the sublattice space and the explicitly shown matrix acts in Nambu (particle-hole) space defined by the Nambu spinors $\Psi(\boldsymbol{r}) = (u, v)^T$ with the spin-up electron-like wave function u close to the K valley and the spin-down hole-like v near K'. The spinors $u(\boldsymbol{r}) = e^{iky}(u_1(x), u_2(x))^T$ and $v(\boldsymbol{r}) = e^{iky}(v_1(x), v_2(x))^T$ are again given in sublattice space and depend on the position $\boldsymbol{r} = (x, y)$. The y-dependence can once more be expressed in terms of plane waves as a result of the homogeneity along this direction.

The magnetic field is encoded in the vector potential as $\boldsymbol{A} = (0, Bx)$ using the convenient Landau gauge[3] and neglecting Zeeman splitting, and Δ is the proximity-induced pairing gap, which is assumed to be real valued. However, the magnetic field reduces the superconducting gap and also the magnetic field is screened in the graphene layer but B and Δ are already assumed to be the effective parameters after renormalization[4]

Inserting all the above and expressing lengths in units of the magnetic length $l_B = \sqrt{\hbar c/eB}$, wave numbers k in $1/l_B$ and energies in the cyclotron energy $E_B = \hbar v_F/l_B$, the Hamiltonian can be written as

$$H = \begin{pmatrix} V & -i\partial_x - i(k+x) & \Delta & 0 \\ -i\partial_x + i(k+x) & V & 0 & \Delta \\ \Delta & 0 & -V & i\partial_x + i(k-x) \\ 0 & \Delta & i\partial_x - i(k-x) & -V \end{pmatrix}. \tag{5.2}$$

From this two different sets of ladder operators can be defined according to

$$\begin{aligned} a &= a(k) = (-i\partial_x - i(x+k))/\sqrt{2} \\ a^\dagger &= a^\dagger(k) = (-i\partial_x + i(x+k))/\sqrt{2} \end{aligned} \tag{5.3}$$

---

[2]This would only result in an identical and decoupled copy of the Hamiltonian with the opposite spin and can hence without loss of generality be ignored.

[3]It can be shown that changing the gauge for example to the symmetric gauge $\boldsymbol{A} = B/2(-y, x)$ does not change the resulting energy eigenvalues.

[4]In general, it is possible to obtain these renormalized values from self-consistency equations, compare [149, 150].

and

$$\begin{aligned}
\tilde{a} &= a(-k) = (-i\partial_x - i(x-k))/\sqrt{2} \\
\tilde{a}^\dagger &= a^\dagger(-k) = (-i\partial_x + i(x-k))/\sqrt{2}
\end{aligned} \tag{5.4}$$

which define the commutator algebra according to $[a, a] = [a^\dagger, a^\dagger] = [\tilde{a}, \tilde{a}] = [\tilde{a}^\dagger, \tilde{a}^\dagger] = [a, \tilde{a}] = [a^\dagger, \tilde{a}^\dagger] = 0$ and $[a, a^\dagger] = [\tilde{a}, \tilde{a}^\dagger] = [a\cdot\tilde{a}^\dagger] = [\tilde{a}, a^\dagger] = 1$ - as (absorbing also the factor of $\sqrt{2}$ in the ladder operators, i.e. $\sqrt{2}a \to a$)

$$H = \begin{pmatrix} V & a & \Delta & 0 \\ a^\dagger & V & 0 & \Delta \\ \Delta & 0 & -V & -\tilde{a}^\dagger \\ 0 & \Delta & -\tilde{a} & -V \end{pmatrix}. \tag{5.5}$$

Inserting this in the Bogoliobov-de Gennes equation $H\Psi = E\Psi$ yields a system of linear equations

$$\begin{aligned}
V u_1 + a u_2 + \Delta v_1 &= E u_1 \\
a^\dagger u_1 + V u_2 + \Delta v_2 &= E u_2 \\
\Delta u_1 - V v_1 - \tilde{a}^\dagger v_2 &= E v_1 \\
\Delta u_2 - \tilde{a} v_1 - V v_2 &= E v_2
\end{aligned} \tag{5.6}$$

which can be simplified drastically for the special case $V = E = 0$ to the system

$$\begin{aligned}
a u_2 + \Delta v_1 &= 0 \\
a^\dagger u_1 + \Delta v_2 &= 0 \\
\Delta u_1 - \tilde{a}^\dagger v_2 &= 0 \\
\Delta u_2 - \tilde{a} v_1 &= 0
\end{aligned} \tag{5.7}$$

where only two components are coupled. Therefore, it is possible to obtain two second order differential equations for two components, e.g. u_1 and u_2

$$\begin{aligned}
\left[\partial_x^2 + 2x\partial_x + x^2 - (k^2 - 1 + \Delta^2)\right] u_2 &= 0 \\
\left[\partial_x^2 - 2x\partial_x + x^2 - (k^2 + 1 + \Delta^2)\right] u_1 &= 0
\end{aligned} \tag{5.8}$$

and in addition the relations connecting them to the remaining components, i.e. v_1 and v_2,

$$\begin{aligned}
v_1 &= -\frac{1}{\Delta} a u_2 \\
v_2 &= -\frac{1}{\Delta} a^\dagger u_1.
\end{aligned} \tag{5.9}$$

The differential equations (5.8) for u_1 and u_2 can be solved with

$$
\begin{aligned}
u_1 &= b_1 e^{\frac{1}{2}(x+x_0)^2} + b_2 e^{\frac{1}{2}(x-x_0)^2} \\
u_2 &= b_3 e^{-\frac{1}{2}(x+x_0)^2} + b_4 e^{-\frac{1}{2}(x-x_0)^2}
\end{aligned}
\tag{5.10}
$$

and result in a wave function of the form[5]

$$
\Psi(\boldsymbol{r}) = e^{iky} \left\{ b_1 e^{\frac{1}{2}(x+x_0)^2} \begin{pmatrix} 1 \\ 0 \\ 0 \\ -\frac{i}{\Delta}(k-x_0) \end{pmatrix} + b_2 e^{\frac{1}{2}(x-x_0)^2} \begin{pmatrix} 1 \\ 0 \\ 0 \\ -\frac{i}{\Delta}(k+x_0) \end{pmatrix} \right.
$$
$$
\left. + b_3 e^{-\frac{1}{2}(x+x_0)^2} \begin{pmatrix} 0 \\ 1 \\ \frac{i}{\Delta}(k-x_0) \\ 0 \end{pmatrix} + b_4 e^{-\frac{1}{2}(x-x_0)^2} \begin{pmatrix} 0 \\ 1 \\ \frac{i}{\Delta}(k+x_0) \\ 0 \end{pmatrix} \right\}
\tag{5.11}
$$

where the Gaussian exponential functions are shifted by the quantity $x_0 = \sqrt{k^2 + \Delta^2}$. Starting from this result, a basis transformation is executed from the functions u_1, u_2, v_1 and v_2 to new x-dependent functions f_1, f_2, g_1 and g_2 using the ansatz

$$
\begin{aligned}
u_1(x) &= f_1(x) + f_2(x) \\
u_2(x) &= g_1(x) + g_2(x) \\
v_1(x) &= \frac{i}{\Delta}(k-x_0)g_1(x) + \frac{i}{\Delta}(k+x_0)g_2(x) \\
v_2(x) &= -\frac{i}{\Delta}(k-x_0)f_1(x) - \frac{i}{\Delta}(k+x_0)f_2(x).
\end{aligned}
\tag{5.12}
$$

Inserting this into the system of linear equations displayed in equation (5.6), relations for the new functions according to

$$
\begin{aligned}
V_- f_1 + V_- f_2 + (a + ik_-)g_1 + (a + ik_+)g_2 &= 0 \\
(a^\dagger - ik_-)f_1 + (a^\dagger - ik_+)f_2 + V_- g_1 + V_- g_2 &= 0 \\
(ik_- \tilde{a}^\dagger + \Delta^2)f_1 + (ik_+ \tilde{a}^\dagger + \Delta^2)f_2 - iV_+ k_- g_1 - iV_+ k_+ g_2 &= 0 \\
iV_+ k_- f_1 + iV_+ k_+ f_2 + (-ik_- \tilde{a} + \Delta^2)g_1 + (-ik_+ \tilde{a} + \Delta^2)g_2 &= 0
\end{aligned}
\tag{5.13}
$$

exploiting a condensed notation with $V_\pm = V \pm E$ and $k_\pm = k \pm x_0$ are obtained. Rearranging these equations employing another set of operators defined as $c_\pm = \partial_x + (x \pm x_0)$, $c_\pm^\dagger = \partial_x - (x \pm x_0)$ (which are thought of only as a short hand notation and not really used as creation

---

[5]Normally, the solution proportional to $e^{(x+x_0)^2/2}$ would be neglected since it diverges for $x \to \pm\infty$ but here it is kept intentionally since it is necessary to perform the following basis transformation.

and annihilation operators, also they lack factors of i and $\sqrt{2}$ in order to fulfil the necessary commutation algebra of second quantized ladder operators) leads to

$$
\begin{aligned}
c_+ g_1 + c_- g_2 &= -iV_-(f_1 + f_2) \\
c_+^\dagger f_1 + c_-^\dagger f_2 &= -iV_-(g_1 + g_2) \\
k_- c_+^\dagger f_1 + k_+ c_-^\dagger f_2 &= iV_+(k_- g_1 + k_+ g_2) \\
k_- c_+ g_1 + k_+ c_- g_2 &= iV_+(k_- f_1 + k_+ f_2)
\end{aligned}
\tag{5.14}
$$

Inserting the first into the fourth and the second into the third equation yields

$$
\begin{aligned}
c_+^\dagger f_1 &= -i\left[\left(\frac{k}{x_0}V - E\right)g_1 + \left(\frac{k}{x_0}V + V\right)g_2\right] \\
c_-^\dagger f_2 &= i\left[\left(\frac{k}{x_0}V - V\right)g_1 + \left(\frac{k}{x_0}V + E\right)g_2\right] \\
c_+ g_1 &= -i\left[\left(\frac{k}{x_0}V - E\right)f_1 + \left(\frac{k}{x_0}V + V\right)f_2\right] \\
c_- g_2 &= i\left[\left(\frac{k}{x_0}V - V\right)f_1 + \left(\frac{k}{x_0}V + E\right)f_2\right].
\end{aligned}
\tag{5.15}
$$

It is obvious that for $V = 0$ and $E = 0$ the above case of Gaussian functions shifted by $\pm x_0$ is retrieved but already for $V = 0$ and arbitrary E the equations decouple and only two functions are connected

$$
\begin{aligned}
c_+^\dagger f_1 &= iE g_1 \\
c_-^\dagger f_2 &= iE g_2 \\
c_+ g_1 &= iE f_1 \\
c_- g_2 &= iE f_2.
\end{aligned}
\tag{5.16}
$$

Inserting the first equation of (5.16) into the third, a differential equation of second order for $f_1(x)$ is obtained as

$$
\frac{1}{iE} c_+ c_+^\dagger f_1 = iE f_1
\tag{5.17}
$$

which results in

$$
[\partial_x^2 - (x + x_0)^2 + E^2 - 1] f_1 = 0
\tag{5.18}
$$

and can be rewritten using the quantities $q = \sqrt{2}(x + x_0)$ and $p = E^2/2 - 1$ as

$$
\left[\frac{d^2}{dq^2} - \frac{q^2}{4} + p + \frac{1}{2}\right] f_1 = 0.
\tag{5.19}
$$

The solution to this special differential equation is known and given by parabolic cylinder functions (compare [101]) from which the two linearly independent variants $D_p(q)$ and $D_p(-q)$ are chosen and hence the solution for f_1 reads

$$f_1(x) = c_1 D_{\frac{E^2}{2}-1}(\sqrt{2}(x+x_0)) + c_2 D_{\frac{E^2}{2}-1}(-\sqrt{2}(x+x_0)). \tag{5.20}$$

From the recursion formula

$$\frac{d}{dq}D_p(q) - \frac{1}{2}qD_p(q) + D_{p+1}(q) = 0 \tag{5.21}$$

from [101] also g_1 follows as

$$g_1(x) = \frac{\sqrt{2}}{iE}(-c_1 D_{\frac{E^2}{2}}(\sqrt{2}(x+x_0)) + c_2 D_{\frac{E^2}{2}}(-\sqrt{2}(x+x_0)). \tag{5.22}$$

An analogous calculation yields the missing functions f_2 and g_2

$$f_2(x) = c_3 D_{\frac{E^2}{2}-1}(\sqrt{2}(x-x_0)) + c_4 D_{\frac{E^2}{2}-1}(-\sqrt{2}(x-x_0))$$

$$g_2(x) = \frac{\sqrt{2}}{iE}(-c_3 D_{\frac{E^2}{2}}(\sqrt{2}(x-x_0)) + c_4 D_{\frac{E^2}{2}}(-\sqrt{2}(x-x_0)) \tag{5.23}$$

and the entire wavefunction can be expressed using the relations (5.12) as

$$
\Psi = e^{iky}\left\{ c_1 \begin{pmatrix} D_{\frac{E^2}{2}-1}(\sqrt{2}(x+x_0)) \\ -\frac{\sqrt{2}}{iE}D_{\frac{E^2}{2}}(\sqrt{2}(x+x_0)) \\ -\frac{\sqrt{2}(k-x_0)}{E\Delta}D_{\frac{E^2}{2}}(\sqrt{2}(x+x_0)) \\ -\frac{i(k-x_0)}{\Delta}D_{\frac{E^2}{2}-1}(\sqrt{2}(x+x_0)) \end{pmatrix} + c_2 \begin{pmatrix} D_{\frac{E^2}{2}-1}(-\sqrt{2}(x+x_0)) \\ \frac{\sqrt{2}}{iE}D_{\frac{E^2}{2}}(-\sqrt{2}(x+x_0)) \\ \frac{\sqrt{2}(k-x_0)}{E\Delta}D_{\frac{E^2}{2}}(-\sqrt{2}(x+x_0)) \\ -\frac{i(k-x_0)}{\Delta}D_{\frac{E^2}{2}-1}(-\sqrt{2}(x+x_0)) \end{pmatrix} \right.
$$

$$
\left. + c_3 \begin{pmatrix} D_{\frac{E^2}{2}-1}(\sqrt{2}(x-x_0)) \\ -\frac{\sqrt{2}}{iE}D_{\frac{E^2}{2}}(\sqrt{2}(x-x_0)) \\ -\frac{\sqrt{2}(k+x_0)}{E\Delta}D_{\frac{E^2}{2}}(\sqrt{2}(x-x_0)) \\ -\frac{i(k+x_0)}{\Delta}D_{\frac{E^2}{2}-1}(\sqrt{2}(x-x_0)) \end{pmatrix} + c_4 \begin{pmatrix} D_{\frac{E^2}{2}-1}(-\sqrt{2}(x-x_0)) \\ \frac{\sqrt{2}}{iE}D_{\frac{E^2}{2}}(-\sqrt{2}(x-x_0)) \\ \frac{\sqrt{2}(k+x_0)}{E\Delta}D_{\frac{E^2}{2}}(-\sqrt{2}(x-x_0)) \\ -\frac{i(k+x_0)}{\Delta}D_{\frac{E^2}{2}-1}(-\sqrt{2}(x-x_0)) \end{pmatrix} \right\}
$$

with constants c_i. Normalizability requires p to be an integer and thus one obtains quantization conditions for the energy, namely the Landau levels $E = \pm\sqrt{2(n+1)}$ for $p = E^2/2 - 1$ and $E = \pm\sqrt{2n}$ for $p = E^2/2$ with n being an integer.

This result stands in marked contrast to the situation when a strain-induced pseudo-magnetic field is considered where the magnetic field has a different sign in both Dirac points and thus is proportional to the τ_z Pauli matrix acting in electron-hole space instead of $\tau_0 = \mathbb{1}$ as the real magnetic field is implemented here. In this case, the spectrum depends on Δ [151, 152].

Although this simple outcome is not intuitive and was not expected from the outset, it can be understood easily enough when the notation is changed.

5.3 CHIRAL FOUR-DIMENSIONAL REPRESENTATION

ewriting the Bogoliubov-de Gennes Hamiltonian as indicated before using σ_i (with $i = 1, 2, 3$ corresponding to x, y, z respectively, and $i = 0$ denoting the unity matrix) Pauli matrices for sublattice and τ_i Pauli matrices for Nambu space yields

$$H = [\sigma_x(-i\partial_x) + \sigma_y(-i\partial_y + x\tau_z) + V]\tau_z + \Delta\tau_x. \tag{5.24}$$

From this formulation it is more obvious than before that it could be useful to implement a four-dimensional formalism. The 4×4 Dirac matrices in the chiral representation are given by

$$\beta = \begin{pmatrix} 0 & -\sigma_0 \\ -\sigma_0 & 0 \end{pmatrix}, \quad \alpha^i = \begin{pmatrix} \sigma_i & 0 \\ 0 & -\sigma_i \end{pmatrix}, \tag{5.25}$$

and the gamma matrices follow as

$$\gamma^0 = \beta = \begin{pmatrix} 0 & -\sigma_0 \\ -\sigma_0 & 0 \end{pmatrix}, \quad \gamma^i = \beta\alpha^i = \begin{pmatrix} 0 & \sigma_i \\ -\sigma_i & 0 \end{pmatrix}, \quad \gamma^5 = \begin{pmatrix} \sigma_0 & 0 \\ 0 & -\sigma_0 \end{pmatrix}. \tag{5.26}$$

These matrices possess the usual properties

$$(\gamma^0)^2 = 1, \quad (\gamma^i)^2 = -1, \quad (\gamma^5)^2 = 1 \tag{5.27}$$

and obey the anticommutation relations

$$\{\gamma^\mu, \gamma^\nu\} = 2g^{\mu\nu}, \quad \{\gamma^\mu, \gamma^5\} = 0. \tag{5.28}$$

With these matrices, the Hamiltonian from above can be expressed as

$$\begin{aligned} H &= \alpha^1\hat{p}_x + \alpha^2(\hat{p}_y + x\gamma^5) + \gamma^5 V - \beta\Delta \\ &= \gamma^0\gamma^1\hat{p}_x + \gamma^0\gamma^2(\hat{p}_y + x\gamma^5) + \gamma^5 V - \gamma^0\Delta. \end{aligned} \tag{5.29}$$

Rephrased that way, the Hamiltonian formally gives a description of Dirac fermions of mass $-\Delta$ in the presence of a pseudo-scalar potential V and a pseudo-vector potential $\boldsymbol{A}$ since these terms are proportional to γ^5.

If $\Psi_E = (u_E, v_E)^T$ is an eigenstate of the Hamiltonian related to an energy $E \geq 0$, it is now easy to find the particle-hole transformation

$$\Psi_{-E}(\boldsymbol{r}) = -\gamma^2\Psi_E^*(\boldsymbol{r}) = \begin{pmatrix} -\sigma_y v_E^*(\boldsymbol{r}) \\ \sigma_y u_E^*(\boldsymbol{r}) \end{pmatrix} \tag{5.30}$$

which yields the corresponding eigenstate with energy $-E$ rendering it unnecessary to find energy solutions for both signs and furthermore presenting a self-conjugative relation for the zero energy states.

Analogously to the coefficients of BCS theory, two quantities

$$a_\pm(k) = a(\pm k) = \sqrt{\frac{1}{2}\left(1 \pm \frac{k}{x_0}\right)}, \quad x_0 = \sqrt{\Delta^2 + k^2} \tag{5.31}$$

can be defined and with them a transformation matrix

$$M = a_+(k) - a_-(k)\gamma^2 \tag{5.32}$$

$$= \begin{pmatrix} a_+ & -a_-\sigma_y \\ a_-\sigma_y & a_+ \end{pmatrix} \tag{5.33}$$

connecting two states via $\psi = M\phi$ where ψ is the x-dependent part of the wave function $\Psi(\boldsymbol{r}) = e^{iky}\psi(x)$. With M a transformed Hamiltonian is obtained as

$$\tilde{H} = M_k^{-1}H_kM_k = \alpha^1\hat{p}_x + \alpha^2\left(X_k + x\gamma^5\right) + \frac{k + \gamma^2\Delta}{X_k}\gamma^5 V(x), \tag{5.34}$$

and fulfils the Bogoliubov-de Gennes equation $\tilde{H}\phi(x) = E\phi(x)$.

5.3.1 ZERO MAGNETIC FIELD, CONSTANT POTENTIAL

For $B = 0$, the Hamiltonian reduces to

$$\tilde{H} = \gamma^0\gamma^1 k_x + \gamma^0\gamma^2 x_0 \tag{5.35}$$

$$= \begin{pmatrix} \sigma_x k_x + \sigma_y x_0 & 0 \\ 0 & -[\sigma_x k_x + \sigma_y x_0] \end{pmatrix}, \tag{5.36}$$

and as solutions plane waves can be chosen. The resulting eigenvalues

$$E_\pm(k_x, k) = \pm E(k_x, k) = \pm\sqrt{k_x^2 + x_0^2} = \pm\sqrt{k_x^2 + k^2 + \Delta^2}, \tag{5.37}$$

[145] are doubly degenerate and depend on Δ. The density of states for positive V and E can be calculated from

$$\rho(\omega; \mathbf{r}) = 2\sum_{s=\pm}\int\frac{d^2k}{(2\pi)^2}|u_s(\mathbf{k})|^2\delta(\omega - E_s(\mathbf{k})) + 2\sum_{s=\pm}\int\frac{d^2k}{(2\pi)^2}|v_s(\mathbf{k})|^2\delta(\omega + E_s(\mathbf{k})), \tag{5.38}$$

and follows as

$$\rho(E) = \frac{1}{\pi(\hbar v_F)^2} \times \begin{cases} 0, & E < \Delta, \\ \frac{EV - (E^2 - \Delta^2)}{\sqrt{E^2 - \Delta^2}}, & \Delta < E < \sqrt{V^2 + \Delta^2}, \\ E - V, & E > \sqrt{V^2 + \Delta^2}. \end{cases} \tag{5.39}$$

Remarkably, there is no BCS square-root singularity for $V = 0$ but instead a finite jump at the position $E = \Delta$ with a linear behaviour of $\rho(E)$ for larger energies.

5.3.2 ZERO POTENTIAL, FINITE MAGNETIC FIELD

$\mathcal{S}$etting $V = 0$ leads to a simplified expression for the Hamiltonian

$$\tilde{H} = \gamma^0 \gamma^1 \hat{p}_x + \gamma^0 \gamma^2 (x_0 + x \gamma^5). \tag{5.40}$$

The main effect of the transformation consists of the momentum k being replaced by x_0. As mentioned before, there is a difference between a pseudo- and a real magnetic field, which becomes obvious in this notation since a pseudo-vector potential is invariant under transformation with M due to $M^{-1} \gamma^0 \gamma^2 \gamma^5 M = \gamma^0 \gamma^2 \gamma^5$ while a normal vector potential is not.

Considering this Hamiltonian, it is obvious that it can be obtained from the original Hamiltonian H by setting $\Delta \to 0$ and $\hat{p}_y \to x_0$. Consequently, the energy spectrum complies with the relativistic Landau levels $E_{k,n,s} = E_n = \sqrt{2n} E_B$ with $n = 0, 1, 2, \ldots$ [6] and thus does not depend on k or Δ. Hence, for all k the energies are the same but there is also a supplementary degeneracy denoted by $s = \pm$.

The corresponding eigenstates can be obtained from the relativistic Landau states via the transformation matrix M and read

$$\phi_{k,n,+}(x) = (\mathcal{F}_n(x + X_k), 0)^T, \quad \phi_{k,n,-}(x) = (0, \sigma_y \mathcal{F}_n(x - x_0))^T \tag{5.41}$$

with the sublattice spinors

$$\mathcal{F}_n(x) = (\frac{1}{\sqrt{2}})^{1 - \delta_{n,0}} \left(\text{sgn}(n) \varphi_{|n|-1}, i \varphi_{|n|} \right)^T \tag{5.42}$$

and normalized oscillator eigenfunctions

$$\varphi_n(x) = (\sqrt{\pi} 2^n n!)^{-1/2} e^{-x^2/2} H_n(x) \tag{5.43}$$

with the Hermite polynomials H_n. With this, the eigenstates are given as

$$\Psi_{k,n,s=\pm}(\boldsymbol{r}) = e^{iky} \begin{pmatrix} \pm a_{k,\pm} \mathcal{F}_n(x \pm x_0) \\ a_{k,\mp} \sigma_y \mathcal{F}_n(x \pm x_0) \end{pmatrix}. \tag{5.44}$$

These eigenstates are, in contrast to the eigenenergies, influenced by the superconducting gap Δ since their center of mass coordinate, which for normal Landau states is given by k, is replaced by $\pm x_0$ in the electron and hole spinor components, respectively.

Due to the relation (5.30), which for the given states and energies reads

$$\Psi_{-k,-n,\pm}(\boldsymbol{r}) = \pm\gamma^2 \Psi^*_{k,n,\pm}(\boldsymbol{r}), \tag{5.45}$$

a state with $E = -E_n$ can be constructed from a given eigenstate $\Psi_{k,n,s}$. Regarding the special case of $n = 0$, this relation links states with $+k$ and $-k$ and it is thus possible to construct two 1D zero-energy Majorana fields labelled by $s = \pm$.

5.4   DENSITY OF STATES

At the Dirac point, the exact eigenstates from equation (5.44) can be used to calculate the local density of states (DOS).

$$
\begin{aligned}
\rho(E) &= \sum_{s=\pm} \int \frac{dk}{2\pi} |\psi_{sx_0,0}(x)|^2 \,\delta(E) + +2 \sum_{s=\pm,n>0} \int \frac{dk}{2\pi} |a_s(k)\psi_{sx_0,n}(x)|^2 \,\delta(E - E_n) \\
&\quad + \int \frac{dk}{2\pi} |a_{\bar{s}}(k)\psi_{sx_0,n}(x)|^2 \,\delta(E + E_n) \\
&= 2g_0\delta(E) + \sum_{n>0}(g_{n-1} + g_n)\delta\left(|E| - \sqrt{2n}E_B\right),
\end{aligned}
\tag{5.46}
$$

where a factor of 2 results from the sum over $s = \pm$. With the dimensionless quantity $a = \Delta/E_B$, the functions g_n follow as

$$g_n = \int \frac{dk}{2\pi} \varphi_n^2\left(\sqrt{(kl_B)^2 + a^2}\right) = \frac{1}{2\pi l_B^2} I_n(a) \tag{5.47}$$

with the integrals

$$I_n(a) = \frac{1}{\sqrt{\pi}2^n n!} \int_{a^2}^{\infty} \frac{du}{\sqrt{u - a^2}} H_n^2\left(\sqrt{u}\right) e^{-u}. \tag{5.48}$$

The $H_n(x)$ are again the Hermite polynomials. Setting $\Delta = 0$ results in integrals of unity, $I_n(0) = 1$, and therefore all weights g_n have the same value positioned at the energies of the Landau levels, thus reproducing the Landau comb. Furthermore, evaluating $I_0(a)$ leads to the prefactor of $\delta(E)$, namely $2g_0 = e^{-a^2}/\pi l_B^2$. Hence, it is sufficient to evaluate the finite energy expressions in the following.

Introducing an effective parameter D, which undertakes the part of a high-energy bandwidth

and eventually has to be sent to infinity, the expression of the local DOS can be reformulated and yields

$$
\begin{aligned}
\rho(E) &= \frac{1}{2\pi l_B^2} \sum_{n>0} e^{-2n(E_B/D)^2} \left[I_{n-1}(a) + I_n(a)\right] \delta\left(|E| - \sqrt{2n}E_B\right) \\
&= \frac{|E|}{\pi l_B^2} \sum_{n>0} (I_{n-1} + I_n) e^{-2n(E_B/D)^2} \int_{-\infty}^{+\infty} \frac{d\lambda}{2\pi} e^{i\lambda(E^2 - 2nE_B^2)}
\end{aligned}
\tag{5.49}
$$

where the δ-function $\delta(E^2 - 2nE_B^2) = (2|E|)^{-1}\delta(|E| - \sqrt{2n}E_B)$ is replaced by an alternative integral representation. Without loss of generality, the sum over n and the integral over λ can be exchanged. Moreover, the integral parameter λ is rescaled as $\lambda \to \lambda/\Delta^2$, also energies E are measured in units of the proximity-induced pairing gap Δ and $\tilde{D} = D/\Delta$. Hence, it follows that

$$
\rho(E) = \frac{\Delta|E|}{\pi(\hbar v_F)^2} e^{-(E/\tilde{D})^2} \int_{-\infty}^{+\infty} \frac{d\lambda}{2\pi a^2} e^{i\tilde{\lambda}E^2} \left(e^{-2i\tilde{\lambda}} + 1\right) \mathcal{G}_a(\tilde{\lambda}),
$$

with the functions

$$
\mathcal{G}_a(\tilde{\lambda}) = \sum_{n\geq 0} I_n(a) e^{-2i\tilde{\lambda}n}, \qquad \tilde{\lambda} = \frac{1}{a^2}\left(\lambda - \frac{i}{\tilde{D}^2}\right).
\tag{5.50}
$$

Since $\left|e^{-2i\tilde{\lambda}}\right| < 1$ and with the Poisson kernel [102], this series can be summed up according to

$$
\begin{aligned}
\mathcal{G}_a(\tilde{\lambda}) &= \sum_{n\geq 0} \frac{1}{\sqrt{\pi}} \int_{a^2}^{\infty} \frac{du}{\sqrt{u-a^2}} \frac{H_n^2(\sqrt{u})}{2^n n!} e^{-u} e^{-2i\tilde{\lambda}n} \\
&= \frac{1}{\sqrt{\pi}} \int_{a^2}^{\infty} \frac{du}{\sqrt{u-a^2}} \frac{\exp\left(u\frac{2e^{-2i\tilde{\lambda}}}{1+e^{-2i\tilde{\lambda}}}\right)}{(1 - e^{-4i\tilde{\lambda}})^{1/2}} e^{-u} \\
&= \frac{1}{1 - e^{-2i\tilde{\lambda}}} \exp\left(-\frac{1 - e^{-2i\tilde{\lambda}}}{1 + e^{-2i\tilde{\lambda}}} a^2\right).
\end{aligned}
\tag{5.51}
$$

As next step, equation (5.51) is inserted into the expression (5.50) and

$$
\rho(E) = \frac{\Delta|E|}{\pi(\hbar v_F)^2} e^{-(E/\tilde{D})^2} \int_{-\infty-i/\tilde{D}^2}^{+\infty-i/\tilde{D}^2} \frac{d\lambda}{2\pi i} \frac{e^{i\lambda E^2 - a^2\tan(\lambda/a^2)}}{a^2\tan(\lambda/a^2)}
\tag{5.52}
$$

is obtained. Taking the limit $D \to \infty$, adding the primarily neglected peak for $E = 0$, and restoring the units that were rescaled, the final exact integral representation of the DOS is achieved and reads

$$
\rho(E) = \frac{e^{-(\Delta/E_B)^2}}{\pi l_B^2} \delta(E) + \frac{|E|}{\pi(\hbar v_F)^2} \int_{-\infty-i0^+}^{+\infty-i0^+} \frac{d\lambda}{2\pi i} e^{i(E^2\lambda - \Delta^2\tan\lambda)/E_B^2} \cot\lambda.
\tag{5.53}
$$
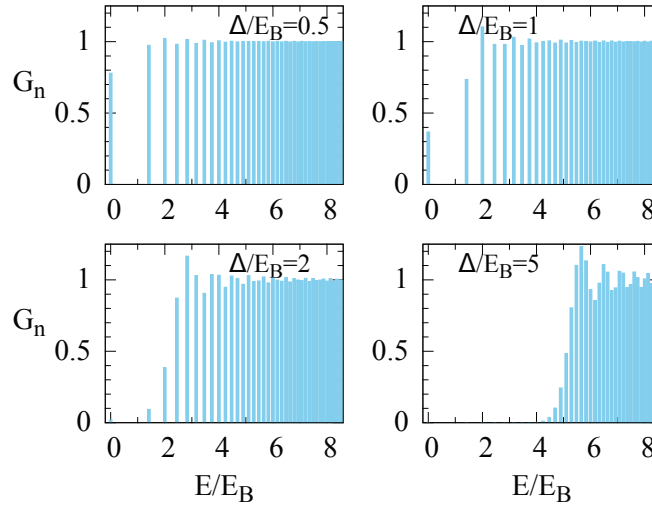
Figure 5.2: DOS weights G_n vs Landau energy E_n for different values of Δ/E_B as bar plot.
[144]

The DOS can also be characterized using the dimensionless weights

$$G_n = \pi l_B^2 \int_{E_n-0^+}^{E_n+0^+} dE \rho(E) \tag{5.54}$$

that define the height of the peaks at the positions of the Landau energies $E_n = \sqrt{2n}E_B$ as well
as their degeneracy and are depicted in figure 5.2 for different values of Δ.

For small Δ as in the upper left figure, the situation is close to that of the Landau comb obtained
for $\Delta = 0$, the heights of all bars are nearly identical. With increasing Δ this gradually changes
until for large $\Delta \to \infty$ – which in these units since Δ is measured in $E_B \sim \sqrt{B}$ equals the
limit $B \to \infty$ – the picture painted in equation (5.39) is reached. Here, the levels with energies
$E < \Delta$ are depleted, followed by a jump to finite height at Δ. Another feature of these pictures is
given by the oscillations depending on the energy. This quantity should be possible to investigate
experimentally via tunneling experiments.

5.5 EDGE STATES

Rather than considering an infinitely extended graphene sheet as before, now an edge
along the line where $x = 0$ is implemented assuming boundary conditions [5, 6] and the semi-
infinite graphene sheet to be spread in the negative half-plane, i.e. for $x < 0$.

5.5.1 WITHOUT PAIRING

Without pairing, the system reduces to the well-known problem of electrons in graphene under the influence of a perpendicular magnetic field in the presence of an edge which has already been discussed in the literature [153]. However, it is nice to have a result to compare to. The wave functions for this situation reduce to

$$\psi(\mathbf{r}) = c_1 e^{iky}\psi_{k,E}(x), \qquad \psi'(\mathbf{r}) = c_2 e^{iky}\sigma_y \psi_{k,E}(x), \tag{5.55}$$

$$\psi_{k,E}(x) = \begin{pmatrix} -\frac{E}{\sqrt{2}}D_{p-1}(-q) \\ iD_p(-q) \end{pmatrix}, \qquad \sigma_y \psi_{k,E}(x) = \begin{pmatrix} D_p(-q) \\ -i\frac{E}{\sqrt{2}}D_{p-1}(-q) \end{pmatrix} \tag{5.56}$$

with $p = E^2/2$ and $q = \sqrt{2}(x+k)$. The armchair boundary condition is given by

$$\psi_A(0,y) + \psi'_A(0,y) = 0, \tag{5.57}$$

$$\psi_B(0,y) + \psi'_B(0,y) = 0 \tag{5.58}$$

with A and B denoting the respective trigonal sublattice. Therefore inserting the wave functions yields the following set of equations translated in matrix formulation as

$$\begin{pmatrix} -\frac{E}{\sqrt{2}}D_{p-1}(-q) & D_p(-q) \\ D_p(-q) & -\frac{E}{\sqrt{2}}D_{p-1}(-q) \end{pmatrix} \begin{pmatrix} c_1 \\ c_2 \end{pmatrix} = 0, \tag{5.59}$$

where now $q = \sqrt{2}k$ since the conditions are taken at the edge, i.e. for $x = 0$, and the dispersion is thus obtained from the secular equation

$$\frac{E^2}{2}D_{p-1}^2(-\sqrt{2}k) - D_p^2(-\sqrt{2}k) = 0. \tag{5.60}$$

5.5.2 WITH PAIRING

For a finite value of Δ, the wave functions take on a more complicated form and read

$$\Psi_{k,E}(\mathbf{r}) = c_1 e^{iky}\begin{pmatrix} a_+\psi_{x_0,E}(x) \\ a_-\sigma_y\psi_{x_0,E}(x) \end{pmatrix} + c_2 e^{iky}\begin{pmatrix} -a_-\psi_{-x_0,E}(x) \\ a_+\sigma_y\psi_{-x_0,E}(x) \end{pmatrix} \tag{5.61}$$

where the $\psi_{\pm x_0,E}$ are essentially given by equation (5.56) except for the fact that q has to be replaced by $q_\pm = \sqrt{2}(x \pm x_0)$. The solutions depending on $+q_\pm$ have already been discarded because they diverge for $x \to -\infty$ and thus wouldn't fulfil the requirement of normalizability. Since these are solutions of the Bogoliubov-de Gennes equation, the upper spinor corresponds to the wave function of an electron in the valley K, which possesses a wave vector k and and

energy E while the lower spinor on the other hand is equivalent to the complex conjugate of the wave function of an electron in the other valley K' with a wave vector $-k$ and opposite energy $-E$. Thus,

$$\begin{pmatrix} \psi_{k,E,A}(\mathbf{r}) \\ \psi_{k,E,B}(\mathbf{r}) \end{pmatrix} = e^{iky} \left(c_1 a_+ \psi_{x_0,E}(x) - c_2 a_- \psi_{-x_0,E}(x) \right), \tag{5.62}$$

$$\begin{pmatrix} \psi'_{-k,-E,A}(\mathbf{r}) \\ \psi'_{-k,-E,B}(\mathbf{r}) \end{pmatrix} = e^{-iky} \left(-c_1^* a_- \sigma_y \psi^*_{x_0,E}(x) - c_2^* a_+ \sigma_y \psi^*_{-x_0,E}(x) \right), \tag{5.63}$$

where the $'$ indicates the spinor at valley K', and the armchair boundary conditions at $x = 0$, which have to be satisfied for all y, follow as

$$\psi_A(0,y) + \psi'_A(0,y) = 0 \tag{5.64}$$

$$\psi_B(0,y) + \psi'_B(0,y) = 0. \tag{5.65}$$

In order to meet these conditions, it is necessary to formulate another set of wave functions that have the same energies but opposite wave vector:

$$\begin{pmatrix} \psi_{-k,E,A}(\mathbf{r}) \\ \psi_{-k,E,B}(\mathbf{r}) \end{pmatrix} = e^{-iky} \left(d_1 a_- \psi_{x_0,E}(x) - d_2 a_+ \psi_{-x_0,E}(x) \right), \tag{5.66}$$

$$\begin{pmatrix} \psi'_{k,-E,A}(\mathbf{r}) \\ \psi'_{k,-E,B}(\mathbf{r}) \end{pmatrix} = e^{iky} \left(-d_1^* a_+ \sigma_y \psi^*_{x_0,E}(x) - d_2^* a_- \sigma_y \psi^*_{-x_0,E}(x) \right). \tag{5.67}$$

With these, the set of equations from the boundary condition reads

$$[c_1 a_+ \psi_{x_0,E}(0) - c_2 a_- \psi_{-x_0,E}(0)] + [d_1^* a_+ \sigma_y \psi_{x_0,E}(0) + d_2^* a_- \sigma_y \psi_{-x_0,E}(0)] = 0 \tag{5.68}$$

$$[c_1 a_- \sigma_y \psi_{x_0,-E}(0) + c_2 a_+ \sigma_y \psi_{-x_0,-E}(0)] + [-d_1^* a_- \psi_{x_0,-E}(0) + d_2^* a_+ \psi_{-x_0,-E}(0)] = 0.$$

Spelled out, this linear system of equations includes four equations in four unknowns and the problem reduces to finding the energies where the determinant $\det[\boldsymbol{W}(E)] = 0$ of the matrix

$$\boldsymbol{W}(E) = \begin{pmatrix} -a_+ \epsilon \tilde{D}^{(-)}_{\epsilon^2-1} & a_+ \tilde{D}^{(-)}_{\epsilon^2} & a_- \epsilon \tilde{D}^{(+)}_{\epsilon^2-1} & a_- \tilde{D}^{(+)}_{\epsilon^2} \\ a_+ \tilde{D}^{(-)}_{\epsilon^2} & -a_+ \epsilon \tilde{D}^{(-)}_{\epsilon^2-1} & -a_- \tilde{D}^{(+)}_{\epsilon^2} & -a_- \epsilon \tilde{D}^{(+)}_{\epsilon^2-1} \\ a_- \tilde{D}^{(-)}_{\epsilon^2} & -a_- \epsilon \tilde{D}^{(-)}_{\epsilon^2-1} & a_+ \tilde{D}^{(+)}_{\epsilon^2} & a_+ \epsilon \tilde{D}^{(+)}_{\epsilon^2-1} \\ a_- \epsilon \tilde{D}^{(-)}_{\epsilon^2-1} & -a_- \tilde{D}^{(-)}_{\epsilon^2} & a_+ \epsilon \tilde{D}^{(+)}_{\epsilon^2-1} & a_+ \tilde{D}^{(+)}_{\epsilon^2} \end{pmatrix} \tag{5.69}$$

vanishes with $\epsilon = E/\sqrt{2}$ and the short hand notation $\tilde{D}^{(\pm)}_p = D_p(\pm\sqrt{2}x_0)$. The determinant was expanded with respect to the first row using Laplace's formula

$$\det W = \sum_{j=1}^{N} (-1)^{i+j} w_{ij} \det W_{ij} \tag{5.70}$$
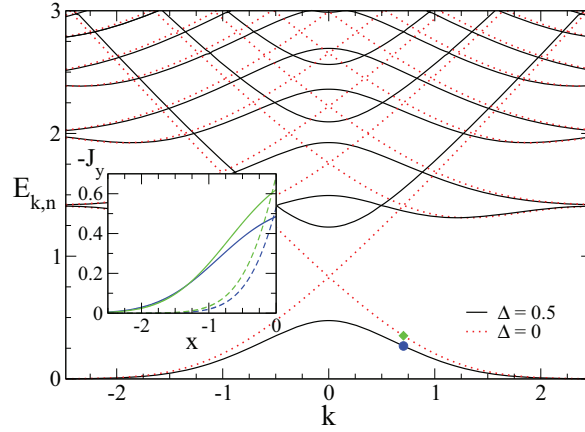
Figure 5.3: Main panel: Edge state spectrum depending on k for $\Delta = 0.5E_B$ (black solid line) and for $\Delta = 0$ (red dotted) obtained for $V = 0$ using armchair conditions at $x = 0$. Inset: Current density $J_y(x)$ measured in units of $-ev_F$ depending on the position x in l_B, for $kl_B = 0.705$. As indicated by the blue circle and green diamond in the main panel, the curves are displayed for $\Delta/E_B = 0.5$ [$\Delta = 0$] at $E_{k,n,s}/E_B \simeq 0.2683$ (blue) [$\simeq 0.3520$ (green)]. Solid and dashed curves correspond to the two degenerate eigenstate solutions labelled with $s = \pm$, respectively. [144]

where w_{ij} is the matrix element in the ith row and the jth column and W_{ij} denotes the submatrix of W that is given when row number i and column j are deleted and afterwards evaluated using numerical root finding methods as described in the previous chapters. The resulting spectrum is shown in the main panel of figure 5.3.

For $\Delta \to 0$, the result from equation (5.60) and [153–155] showing chiral edge states is reproduced while for finite Δ the dispersion develops gaps at $k = 0$ that result from mixing of states identified with electron- and hole-like edge states.

Another important quantity is the charge current density, denoted as $\boldsymbol{J} = (J_x, J_y)^T$ which for a given eigenstate labelled by λ is given as

$$\boldsymbol{J}_\lambda(\boldsymbol{r}) = -ev_F \left(u_\lambda^\dagger \boldsymbol{\sigma} u_\lambda + v_\lambda^\dagger \boldsymbol{\sigma} v_\lambda \right). \tag{5.71}$$

The x-component vanishes, i.e. $J_x = 0$, whereas the y-component follows from the edge solution

$$u_\lambda = [c_1 a_+ \psi_{x_0,E} - c_2 a_- \psi_{-x_0,E}], \tag{5.72}$$

$$v_\lambda = \sigma_y [c_1 a_- \psi_{x_0,E} + c_2 a_+ \psi_{-x_0,E}], \tag{5.73}$$

where c_1 and c_2 are obtained from the solution of the boundary conditions, as

$$J_{y,\lambda} = u_\lambda^\dagger \sigma_y u_\lambda + v_\lambda^\dagger \sigma_y v_\lambda = |c_1|^2 \psi_{x_0,E}^\dagger \sigma_y \psi_{x_0,E} + |c_2|^2 \psi_{-x_0,E}^\dagger \sigma_y \psi_{-x_0,E}$$
$$= |c_1|^2 \left(-\sqrt{2} E D_{p-1}(-q_+) D_p(-q_+) \right) + |c_2|^2 \left(-\sqrt{2} E D_{p-1}(-q_-) D_p(-q_-) \right). \tag{5.74}$$

The result is depicted in the inset of figure 5.3 for the two degenerate states labelled with $s = \pm$ taken at $k = 0.705$ and the lowest energy level for both $\Delta = 0$ and $\Delta = 0.5$. As expected, the picture can be interpreted as unidirectional states travelling along the edge at $x = 0$. In comparison to the case for vanishing Δ, the magnitude of the current is decreased for finite Δ as it happens also for snake states, see below.

5.6 FINITE POTENTIAL

Until now, all results only visualize the physics at the Dirac point where $V = E_F = 0$. As described there are only flat Landau levels for the bulk situation and dispersion can only be achieved by changing this, for example by employing an edge as done in the previous chapter. Yet, the underlying system changes once a finite potential $V \neq 0$ is applied. Again, the infinitely extended graphene sheet is considered. Here, it is possible to expand the Nambu spinors as

$$u(x) = \sum_n u_n(k)\psi_{k,n}(x), \qquad v(x) = \sum_n v_n(k)\sigma_y\psi_{-k,n}(x), \tag{5.75}$$

in terms of the eigenstates of the usual graphene Landau levels

$$\psi_{k,n}(x) = \frac{1}{\sqrt{2^{1-\delta_{n,0}}\sqrt{\pi}|n|!}} \begin{pmatrix} \mathrm{sgn}(n)\sqrt{|n|}D_{|n|-1}(\sqrt{2}(x+k)) \\ iD_{|n|}(\sqrt{2}(x+k)) \end{pmatrix}$$

$$= \frac{1}{\sqrt{2^{1-\delta_{n,0}}}} \begin{pmatrix} \mathrm{sgn}(n)\phi_{|n|-1}(x+k) \\ i\phi_{|n|}(x+k) \end{pmatrix}$$

$$\sigma_y\psi_{-k,n}(x) = \frac{1}{\sqrt{2^{1-\delta_{n,0}}\sqrt{\pi}|n|!}} \begin{pmatrix} D_{|n|}(\sqrt{2}(x-k)) \\ i\,\mathrm{sgn}(n)\sqrt{|n|}D_{|n|-1}(\sqrt{2}(x-k)) \end{pmatrix}$$

$$= \frac{1}{\sqrt{2^{1-\delta_{n,0}}}} \begin{pmatrix} \phi_{|n|}(x-k) \\ i\,\mathrm{sgn}(n)\phi_{|n|-1}(x-k) \end{pmatrix}. \tag{5.76}$$

The matrix $B_{mn}(k)$ defines the overlaps of the respective wave functions according to

$$B_{mn}(k) = \int dx\, \psi^\dagger_{-k,m}(x)\sigma_y\psi_{k,n}(x) \tag{5.77}$$

$$= \frac{1}{2^{1-(\delta_{n,0}+\delta_{m,0})/2}} \left(\mathrm{sgn}(n)A_{|m|,|n|-1}(k) + \mathrm{sgn}(m)A_{|m|-1,|n|}(k)\right). \tag{5.78}$$

with the functions

$$A_{mn}(k) = \int dx\phi_m(x-k)\phi_n(x+k) = A_{mn}(-k) = (-1)^{m+n}A_{mn}(-k)$$

$$= e^{-k^2}\left(\frac{2^n m!}{2^m n!}\right)^{\varepsilon_{nm}/2} (\varepsilon_{nm}k)^{|n-m|}L^{|n-m|}_{(m+n)/2+\varepsilon_{nm}(m-n)/2}(2k^2) \tag{5.79}$$
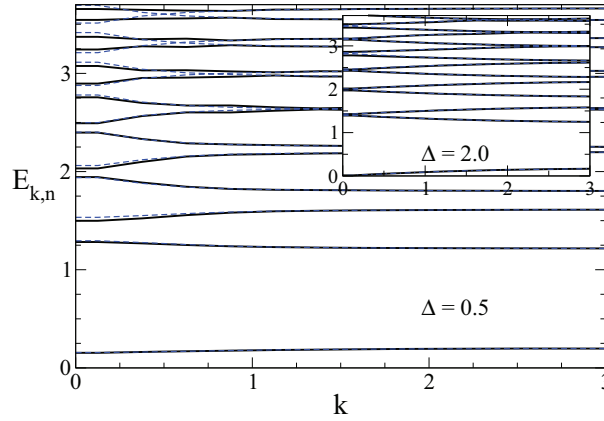
Figure 5.4: Main panel: Dispersion relation with potential $V = 0.2E_B$ for $\Delta = 0.5E_B$. Inset: Spectrum for the same potential and $\Delta = 2E_B$. Only the regime with $k \geq 0$, $E \geq 0$ is shown since the spectrum is symmetric for $k \to -k$ and $E \to -E$. Solid black lines correspond to the result of numerical diagonalization of equation (5.80) while dashed blue curves refer to the perturbative results from the energies modified by equation (5.81), respectively. [144]

where $\phi_n(x)$ are the ordinary normalized Landau orbitals in Landau gauge, $\varepsilon_{nm} = \text{sgn}(n-m+0.5)$ and $L_p^q(x)$ denotes the Laguerre polynomials. Hence, the problem can be written as $H(k)Z(k) = EZ(k)$, where $Z(k)$ is the infinite dimensional vector

$$Z^T(k) = (\dots, u_{-2}(k), v_{-2}(k), u_{-1}(k), v_{-1}(k), u_0(k), v_0(k), u_1(k), v_1(k), u_2(k), v_2(k), \dots)$$

and $H(k)$ is the infinite matrix

$H(k) =$

$$\begin{pmatrix}
 & \vdots & \vdots & \vdots & \vdots & \vdots & \vdots & \\
\dots & \xi_{-1} & 0 & 0 & \Delta B_{-1,0}(-k) & 0 & \Delta B_{-1,1}(-k) & \dots \\
\dots & 0 & -\xi_1 & \Delta^* B_{-1,0}(k) & 0 & \Delta^* B_{-1,1}(k) & 0 & \dots \\
\dots & 0 & \Delta B_{0,-1}(-k) & \xi_0 & 0 & 0 & \Delta B_{0,1}(-k) & \dots \\
\dots & \Delta^* B_{0,-1}(k) & 0 & 0 & -\xi_0 & \Delta^* B_{0,1}(k) & 0 & \dots \\
\dots & 0 & \Delta B_{1,-1}(-k) & 0 & \Delta B_{1,0}(-k) & \xi_1 & 0 & \dots \\
\dots & \Delta^* B_{1,-1}(k) & 0 & \Delta^* B_{1,0}(k) & 0 & 0 & -\xi_{-1} & \dots \\
 & \vdots & \vdots & \vdots & \vdots & \vdots & \vdots &
\end{pmatrix}$$

$$(5.80)$$

with $\xi_n = \text{sgn}(n)\sqrt{2|n|} - E_F$ where it was taken into account that B_{mn} obeys the symmetry relation $B_{nn}(k) = 0$. For finite maximum values of n and m, the problem can be solved numerically and the spectrum follows from the condition $\det(H(k)) = 0$. It is shown in figure 5.4. For large values of $|k|$ the standard relativistic Landau levels are again recovered, this time shifted by

the potential while there are deviations around $k = 0$. Thus, dispersion is caused by applying a potential, or, as V includes also μ, shifting the chemical potential of the system.

In order to test these results, it is useful to execute also a perturbative calculation. To achieve this, the $V = 0$ solution given in equation (5.44) can be used to expand around it, utilising the term in equation (5.34), which is $\sim V$, as small perturbation. Thus, expressing the energies as $E_{k,n,s} = E_n + \delta E_{k,n,s}$ and executing the calculations of the first-order degenerate perturbation theory, the correction is given by

$$\delta E_{k,n,\pm} = \pm \frac{|V|}{X_k} \sqrt{k^2 + \Delta^2 S_{k,n}^2}. \tag{5.81}$$

$S_{k,n}$ includes the overlap between Landau states $\mathcal{F}_n$ centered at $+x_0$ and $-x_0$ and can be expressed as $S_{k,0} = e^{-X_k^2}$ and $S_{k,n>0} = \frac{1}{2}e^{-X_k^2}[L_{n-1}(2X_k^2) + L_n(2X_k^2)]$ with the Laguerre polynomials L_n [102]. The results are also shown in figure 5.4. For $|k| \gg \Delta$, i.e. in the outer regions of the figure, the correction (5.81) results in a uniform shift of magnitude $\pm|V|$ of all Landau energies, whereas for $k = 0$, it is reduced to $\pm|V S_{0,n}|$. The function $S_{0,n}$ oscillates when changing n leading to the features depicted.

5.7 PERPENDICULAR ELECTRIC AND MAGNETIC FIELD

Instead of considering a constant potential as in the previous section, now a uniform electric field $\mathcal{E}$ is applied causing the linear electrostatic potential $V = e\mathcal{E}x$. The Hamiltonian for this system in the four-dimensional representation reads

$$\mathcal{H}_{DBdG}(k) = v_F \left[\alpha^1 \hat{p}_x + \alpha^2 (\hbar k + \frac{eB}{c} x \gamma^5) \right] + e\mathcal{E}x\gamma^5 - \Delta\gamma^0, \tag{5.82}$$

and the Bogoliubov-de Gennes equation follows as

$$\left[\gamma^0(-i\partial_t + \epsilon x \gamma^5) + \gamma^1 \hat{p}_x + \gamma^2(k + x\gamma^5) - \Delta \right] \Psi = 0 \tag{5.83}$$

with $\epsilon = c\mathcal{E}/v_F B$ assumed to be in the regime where $|\epsilon| < 1$. Following the steps of [156] where the analogous problem for $\Delta = 0$ was solved, it is possible to apply an appropriate Lorentz boost in y-direction into the reference frame where the electric field vanishes and the exact solution is known. With this trick, it is possible to obtain an exact result for a linear potential although the same was not realizable for the supposedly simpler case of a constant potential.

Moving to the time-independent problem, i.e. replacing $i\partial_t \to E$ yields

$$\left[\gamma^0(-E + \beta x \gamma^5) + \gamma^1 \hat{p}_x + \gamma^2(k + x\gamma^5) - \Delta \right] \Psi = 0. \tag{5.84}$$

Next, a transformation according to

$$\Psi = S\tilde{\Psi} = \left(\cosh\left(\frac{\eta}{2}\right) - \sinh\left(\frac{\eta}{2}\right)\gamma^0\gamma^2\right)\tilde{\Psi} \tag{5.85}$$

can be done with the Lorentz angle $\eta = \tanh^{-1}\epsilon$ defining the reference frame with $\mathcal{E}' = 0$. In the next step, it is necessary to rescale a number of variables using the rescaling parameter $\zeta \equiv (1 - \epsilon^2)^{1/4}$, namely

$$x' = \zeta x, \quad k' = (k + \epsilon E)/\zeta^3, \quad E' = (E + \epsilon k)/\zeta^3, \quad \Delta' = \Delta/\zeta \tag{5.86}$$

where rescaled parameters can be identified by the tick. With $x_0' = \sqrt{k'^2 + \Delta'^2}$, the transform yields the situation as considered in section 5.2 and a back-transformation from equation (5.44) produces the spectrum and eigenstates for the linear potential. With restored units the dispersion that again does not depend on Δ is given by

$$E_{k,n,s} = -\hbar\epsilon v_F k + \text{sgn}(n)\sqrt{2|n|}\zeta^3 E_B, \tag{5.87}$$

where $n \in \mathbb{Z}$ and k is only allowed to take on values for which $E_{k,n,s} \geq 0$. All levels have a two-fold degeneracy according to $s = \pm$. The respective eigenstates to these energies follow as

$$\begin{aligned}
\Psi_{k,n,\pm}(\boldsymbol{r}) &= e^{iky}\zeta^{3/2}\left[\cosh(\eta/2)\begin{pmatrix} \pm a_{k',\pm}\mathcal{F}_n(x' \pm x_0') \\ a_{k',\mp}\sigma_y\mathcal{F}_n(x' \pm x_0') \end{pmatrix}\right.\\
&+ \left.\sinh(\eta/2)\begin{pmatrix} \mp a_{k',\pm}\sigma_y\mathcal{F}_n(x' \pm x_0') \\ a_{k',\mp}\mathcal{F}_n(x' \pm x_0') \end{pmatrix}\right],
\end{aligned} \tag{5.88}$$

whereas states with negative energy can be calculated from the relation (5.30). Setting $\epsilon = 0$ leads from equation (5.88) to the original solution (5.44) in the reference frame.

The line along which the potential changes sign, i.e. from $V < 0$ to $V > 0$, can be interpreted as *p-n* junction (compare chapter 2.5). In absence of proximity induced pairing $\Delta = 0$, it was shown that snake states propagating along the interface exist not only for step-like but also for smeared out potential changes. For the present setup, they would travel in y-direction with a rescaled Fermi velocity $\epsilon v_F = c\mathcal{E}/B$. For finite $\Delta > 0$, however, the spectrum described by equation (5.87) which defines states with linear dispersion in k defined by the negative slope $-\hbar\varepsilon$ and the spacing of the relativistic Landau levels rescaled due to ζ, indicates that the snake states survive in the superconducting case and keep the same snake velocity. The lowest level $n = 0$ especially is localized close to the interface at $x = 0$.

Furthermore, it is possible to calculate the total charge current $I = \int dx J_y(x)$, which is carried by a certain state travelling in y-direction along the interface. Combining the equations (5.71) and (5.88) yields the relation

$$\frac{I(\Delta)}{I(0)} = \frac{1}{\sqrt{1 + \left(\frac{\Delta'}{k'}\right)^2}}. \tag{5.89}$$

As for the current by edge states discussed in section 5.5, also in this situation the current is maximal for $\Delta = 0$ and is reduced for the superconducting case, decreasing gradually with increasing Δ.

5.8 COMPARISON WITH 2DEG

$\mathcal{C}$ontrasting the results obtained in the infinite bulk case (i.e. without an edge) for the Dirac fermions in graphene with the case of electrons in a 2DEG which are described via the Schrödinger equation, reveals some differences[6].

The spectrum can be obtained in a similar manner as for the graphene case, namely by expanding in the Landau level basis according to

$$u_\lambda(x, y) = \frac{e^{iky}}{L} \sum_n u_n^{(\lambda)}(k)\phi_n(x + k)$$

$$v_\lambda(x, y) = \frac{e^{iky}}{L} \sum_n v_n^{(\lambda)}(k)\phi_n(x - k) \tag{5.90}$$

with the normalized Landau orbitals in the Landau gauge

$$\phi_n(x) = \left(\frac{1}{\sqrt{\pi}2^n n!}\right)^{\frac{1}{2}} H_n(x)e^{-\frac{x^2}{2}} \tag{5.91}$$

and the Hermite polynomials $H_n(x)$. The index $n = 0, 1, 2, \ldots$ only runs over positive integers since we are concerned with the 2DEG Landau levels. With energy eigenvalues $\xi_n = n + 1/2 + V - E_F$ of the original Hamiltonian of the system and the funtcions A_{mn}, which express the overlap between the Landau levels and have been defined in equation (5.79), the infinite matrix $H(k)$ to the eigenvalue equation $H(k)Z(k) = EZ(k)$ reads

$H(k) =$

$$\begin{pmatrix} \xi_0 & \Delta A_{00}(-k) & 0 & \Delta A_{01}(-k) & 0 & \Delta A_{02}(-k) & 0 & \ldots \\ \Delta^* A_{00}(k) & -\xi_0 & \Delta^* A_{01}(k) & 0 & \Delta^* A_{02}(k) & 0 & \Delta^* A_{03}(k) & \ldots \\ 0 & \Delta A_{10}(-k) & \xi_1 & \Delta A_{11}(-k) & 0 & \Delta A_{12}(-k) & 0 & \ldots \\ \Delta^* A_{10}(k) & 0 & \Delta^* A_{11}(k) & -\xi_1 & \Delta^* A_{12}(k) & 0 & \Delta^* A_{13}(k) & \ldots \\ \vdots & \vdots & \vdots & \vdots & \vdots & \vdots & \vdots & \ddots \end{pmatrix}$$

$$\tag{5.92}$$

and numerical diagonalization yields the spectrum in figure 5.5. The most obvious difference to the graphene case for the spectrum given by the black solid lines, which is obtained for $V = E_F = 0$, is given by the height of the Landau levels for large k since here, there are the equidistantly

---

[6]These results are not contained in [144].
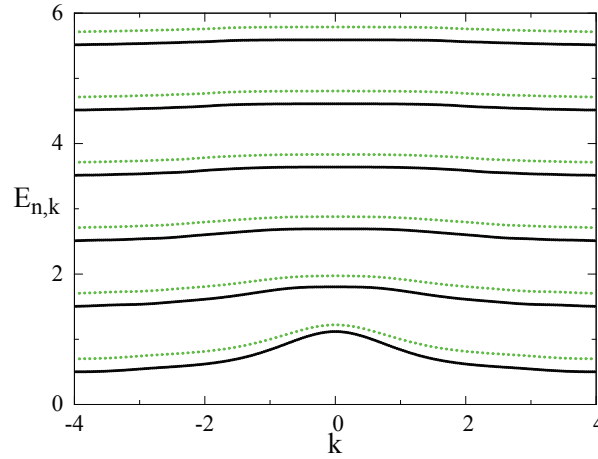
Figure 5.5: Dispersion relation for Schrödinger fermions in the presence of a superconducting gap $\Delta = 1$ at the Dirac point (black solid), i.e. $V = E_F = 0$, and for a finite potential $V = 0.2$ (green dotted).

spaced standard Landau levels positioned at $E_n = n + 1/2$. On the second glance, it becomes obvious that in the 2DEG case, there is already dispersion simply caused by a finite Δ without adding a potential. This occurs due to the fact that there is no such symmetry as in the graphene case which leads to the transformation described in section 5.3 and the unperturbed spectrum. For finite V again these levels are shifted according to V (dotted green spectrum) but otherwise there are no obvious changes. Perturbative results also mirror the main features in this case.

The local density of states can also be computed. Here, a small broadening of the δ-peaks according the Lorentzian distribution

$$f(E) = \frac{1}{\pi} \frac{s}{s^2 + (E - E_n)^2} \tag{5.93}$$

was used where the influence of the Landau level at Landau energy E_n on the particle with energy E due to the broadening s of the peak is calculated for all energies. The result, weighted by the wave functions as $|\psi_{n,k}(x = 0)|^2$, is presented in figure 5.6 and shows that for small values of Δ, all levels are visible since they don't deviate a lot from their normal equally spaced positions while for large Δ the gap around $k = 0$ increases and the levels get pushed together at $E = \Delta$, leading to a depletion of the lower energy states and a large peak in the local DOS at Δ. In contrast to the Dirac case, here the square root singularity of BCS theory is present.

5.9   CONCLUSIONS

In this chapter a theoretical analysis of the combined effects of an orbital magnetic field and proximity-induced pairing in a graphene monolayer for an experimentally realizable setup has been presented. Surprisingly, at the Dirac point, i.e. for $E_F = V = 0$, the exact solution yields an energy spectrum consisting of the relativistic Landau levels independent of Δ which
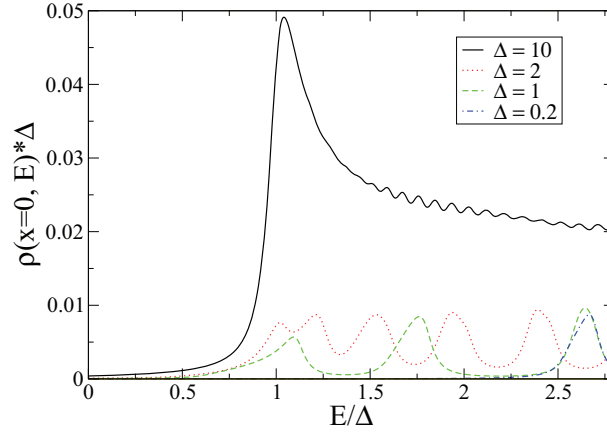
Figure 5.6: Local density of states vs energy for different values of the proximity-induced gap Δ and a finite broadening of the levels at $E_F = 0$.

is different to other known systems, as was emphasized when opposing to the 2DEG situation. Nevertheless, the eigenstates exhibit a dependence on the superconducting gap Δ and therefore also observables are expected to reveal pairing effects. A displayed example of this was given by the density of states, which depicts the entire crossover from the zero magnetic field BCS-type density of states to the Landau comb expected for a magnetic field but no pairing.

Moving away from the Dirac point by applying a constant potential, the counter-intuitive result of an independent spectrum vanishes, as well as for the case where an edge restricts the graphene sheet. Furthermore, the situation of crossed electric and magnetic fields has been discussed, which can be mapped to the problem at the Dirac point in the absence of an electric field. The solution obtained by back transformation reveals snake states which continue to propagate with the same velocity in the presence of pairing. Both in the case of edge states and the snake states in the crossed fields, the resulting current is reduced with increasing Δ.

Summary and Outlook

Within the scope of this thesis, the impact of a variety of influences on different inherent properties of a single graphene sheet was theoretically analysed.

The first setting was concerned with a clean graphene monolayer in the presence of an inhomogeneous magnetic field profile consisting of a central region with negative magnetic field surrounded by parts with positive magnetic field. The field strength was chosen high enough such that Landau quantization takes place. Thus, in a semi-classical picture there are Landau orbits in the areas with a constant field and snake states along the lines of a field change, effectively creating a waveguide, i.e. a one-dimensional quantum wire. In this chapter the emphasis was based on the zero-energy sector where the single-particle dispersion relation exhibits a Landau-like flat band only and therefore all current matrix elements vanish. As a consequence the conductance has to remain zero unless virtual transitions to bands with a finite energy are taken into account, which can be caused by Coulomb interactions. Whereas the zero-mode sector was treated using the Hartree-Fock theory leading to a dispersing energy spectrum but no conductance yet, taking into account also the finite energy band transitions was implemented making use of the Kubo formula evaluated with the Keldysh Green's function technique. The resulting conductance was calculated and is found not to be quantized as for the non-zero energy bands but to depend characteristically on the filling factor of the zero-mode. Therefore, a non-zero conductance is achieved only if interactions are present and hence this setting presents a novel opportunity to test for the presence of electron-electron interactions in a sample using transport experiments only. Moreover, the state of this conductor induced from a zero-mode cannot be captured using the standard picture for one-dimensional solids including interactions, namely the Tomonaga-Luttinger liquid theory. Another possibility to obtain snake states in graphene is not to use inhomogeneous magnetic field but to utilize the special dispersion relation around the Dirac points to fabricate a *p-n* junction. This can be achieved merely by applying gates with different electrostatic potential causing the Fermi level to lie in the conduction and valence band of the continuously adjustable Dirac cone on both sides of the interface. As a result of the Klein phenomenon, an electron can thus

tunnel through the potential barrier as a hole with finite probability or be reflected leading to a combined snaking-skipping state propagating unidirectionally along the interface due to the homogeneous underlying magnetic field. The first geometry considered was that of a straight *p-n* junction where always a chiral interface state can be found close to the Dirac point whose group velocity was found to illustrate the crossover between the classical drift velocity in crossed electric and magnetic fields and the semi-classical value predicted for a motion entirely determined as caused by a pure snake state. Interface states away from the Dirac point, on the other hand, yield skipping motions only. The latter are the only states also found for the Schrödinger fermions in a two-dimensional electron gas. These features and the behaviour of the states close to the avoided crossings in the spectra was observed using the probability density and also the current density was calculated. The second considered geometry is given by a circular *p-n* junction since both of these geometries are easily realizable and have already been investigated also experimentally. Here, the chiral interface state induces sizeable equilibrium ring currents of the magnitude of the highest possible persistent current in a comparatively sized quantum ring, which are close to the interface and cause a magnetic moment.

The third influence that was investigated, is the effect summarized in the superconducting gap which can be proximity-induced by contacting a graphene sheet with a s-wave superconductor. In recent works [52–54] it was demonstrated that this effect can coexist with comparatively high magnetic fields sufficient for Landau-quantization although this is usually prevented by the Meissner effect. For a chemical potential directly at the Dirac point, an exact analytical solution of the Bogoliubov-de Gennes equation has revealed the counter-intuitive result of a unperturbed and independent relativistic Landau levels. The observables, however, are changed by the pairing since the eigenstates are found to depend on the superconducting gap. As an example, the local density of states was computed for different values of this gap and the transition from the Landau comb for vanishing superconductivity to the situation for vanishing magnetic field was presented where the proximity-induced gap results in a gapped spectrum and thus the levels with a smaller energy are depleted. Furthermore, the situation with an edge was considered where a dispersion and edge state currents occur. In addition, starting again from the infinitely expanded graphene sheet, a constant potential was assumed and revealed to also cause dispersion. For a linear potential, on the other hand, it is possible to find a transformation coupling these solutions to the exact result obtained at the Dirac point via a Lorentz boost and thus the spectrum is given by flat bands tilted by an angle leading to linear slopes.

Possible further ideas could be to regard other geometries both for the inhomogeneous magnetic field and the potential, or to consider two coupled *p-n* junctions forming a *p-n-p* junction since there is also a lot of research in this field. Besides, the combination of a proximity-induced gap and a *p-n* junction in a magnetic field could be investigated as well as different models to include edges. Also, it would be very desirable that the predictions presented could be put to experimental tests because the evaluated observables were chosen such that they are experimentally accessible.

Appendices

LIST OF PUBLICATIONS

In this appendix, the publications will be included as full reference and also a description of the own contributions will be given.

INTERACTION-INDUCED CONDUCTANCE FROM ZERO MODES IN A CLEAN MAGNETIC GRAPHENE WAVEGUIDE, PUBLISHED 20 AUGUST 2015 IN PHYSICAL REVIEW B

In this paper, my part consists of the single particle description including the numerical and analytical calculation of wave functions, current- and interaction matrix elements, the numerical root finding evaluation to find the dispersion and its dependence on the waveguide width d (see also Appendix A in the paper). I was also involved in the Hartree-Fock theory although the code yielding the final results was not written by me but I extracted the values of the Fermi velocity and momentum given in figure 5. Finally, the numerical evaluation of the results for the conductance that were analytically obtained via the Kubo formula due to the Keldysh technique was realized by me.

Reference: L. Cohnitz, W. Häusler, A. Zazunov and R. Egger, *Interaction-induced conductance from zero modes in a clean magnetic graphene waveguide*, Phys. Rev. B **92**, 085422 (2015)

CHIRAL INTERFACE STATES IN GRAPHENE $p-n$ JUNCTIONS, PUBLISHED 25 OCTOBER 2016 IN PHYSICAL REVIEW B

The analytical solution for the wave functions, as well as the numerical evaluation of the conditions and therefore the spectra including the chiral edge state were done by me in the case of the straight junction. I also found an approximative expression for the velocity v_s. I found the analytical wave function solutions for the circular junction and helped in the numerical analysis

of the spectra. Also the numerical root finding for the spectrum in the Schrödinger case presented in the appendix was carried out by me.

Reference: Laura Cohnitz, Alessandro De Martino, Wolfgang Häusler, and Reinhold Egger, *Chiral interface states in graphene p-n junctions*, Phys. Rev. B **94**, 165443 (2016)

Proximity-induced superconductivity in Landau-quantized graphene monolayers, submitted to Physical Review Letters, 9 August 2017

In this project, I found the surprising exact solution of the unaltered spectrum at the Dirac point and the influenced eigenstates which the main emphasis of the paper is on, although originally carried out in a different notation. Moreover, I was involved in the calculation of the edge states and did the numerical evaluation on which the spectra of both the edge state and the bulk for finite potential are based, as well as the numerical implementation of the analytically obtained formulas for the density of states and the perturbative results. In addition, the calculation and numerical implementation of the current density in figure 3 were carried out by me.

Reference: L. Cohnitz, A. De Martino, W. Häusler, R. Egger, *Proximity-induced superconductivity in Landau-quantized graphene monolayers*, preprint arXiv:1708.02892 (2017)

Bibliography

[1] O. Klein, *Die Reflexion von Elektronen an einem Potentialsprung nach der relativistischen Dynamik von Dirac*, Zeitschrift für Physik **53** (3–4): 157 (1929).

[2] M.I. Katsnelson, K. S. Novoselov, and A. K. Geim, *Chiral tunneling and the Klein paradox in graphene*, Nat. Phys. 2, 620 (2006).

[3] K.S. Novoselov, A.K. Geim, S.V. Morozov, D. Jiang, Y. Zhang, S.V. Dubonos, I.V. Grigorieva, and A.A. Firsov, *Electric Field Effect in Atomically Thin Carbon Films*, Science **306**, 666 (2004).

[4] K.S. Novoselov, A.K. Geim, S.V. Morozov, *Two-dimensional gas of massless Dirac fermions in graphene* et al., Nature 438, 197-200 (2005)

[5] C.W.J. Beenakker, *Colloquium: Andreev reflection and Klein tunneling in graphene*, Rev. Mod. Phys. **80**, 1337 (2008).

[6] A.H. Castro Neto, F. Guinea, N.M.R. Peres, K.S. Novoselov, and A. Geim, *The electronic properties of graphene*, Rev. Mod. Phys. **81**, 109 (2009).

[7] M.O. Goerbig, *Electronic properties of graphene in a strong magnetic field*, Rev. Mod. Phys. **83**, 1193 (2011).

[8] E.Y. Andrei, G. Li, and X. Du, *Electronic properties of graphene: a perspective from scanning tunneling microscopy and magneto-transport*, Rep. Prog. Phys. **75**, 056501 (2012).

[9] V.M. Miransky and I.A. Shovkovy, *Quantum field theory in a magnetic field: From quantum chromodynamics to graphene and Dirac semimetals*, Phys. Rep. **576**, 1 (2015).

[10] A.F. Young and P. Kim, *Electronic Transport in Graphene Heterostructures*, Annu. Rev. Condens. Matter Phys. **2**, 101 (2011).

[11] C.R. Dean, A.F. Young, I. Meric, C. Lee, L. Wang, S. Sorgenfrei, K. Watanabe, T. Taniguchi, P. Kim, K.L. Shepard, and J. Hone, *Boron nitride substrates for high-quality graphene electronics*, Nature Nanotech. **5**, 722 (2010).

[12] E.J. Bergholtz and Z. Liu, *Topological flat band models and fractional Chern insulators*, Int. J. Mod. Phys. B **27**, 1330017 (2013).

[13] S.A. Parameswaran, R. Roy, and S.L. Sondhi, *Fractional quantum Hall physics in topological flat bands*, C. R. Phys. **14**, 816 (2013).

[14] L. Zheng, L. Feng, and W. Yong-Shi, *Exotic electronic states in the world of flat bands: From theory to material*, Chin. Phys. B **23**, 077308 (2014).

[15] E. Tang, J.W. Mei, and X.G. Wen, *High-Temperature Fractional Quantum Hall States*, Phys. Rev. Lett. **106**, 236802 (2011).

[16] K. Sun, Z. Gu, H. Katsura, and S. Das Sarma, *Nearly Flatbands with Nontrivial Topology*, Phys. Rev. Lett. **106**, 236803 (2011).

[17] T. Neupert, L. Santos, C. Chamon, and C. Mudry, *Fractional Quantum Hall States at Zero Magnetic Field*, Phys. Rev. Lett. **106**, 236804 (2011).

[18] W. Häusler, *Flat-band conductivity properties at long-range Coulomb interactions*, Phys. Rev. B **91**, 041102(R) (2015).

[19] J. Vidal, B. Douçot, R. Mosseri, and P. Butaud, *Interaction Induced Delocalization for Two Particles in a Periodic Potential*, Phys. Rev. Lett. **85**, 3906 (2000).

[20] J. Vidal, P. Butaud, B. Douçot, and R. Mosseri, *Disorder and interactions in Aharonov-Bohm cages*, Phys. Rev. B **64**, 155306 (2001).

[21] K. Kazymyrenko, S. Dusuel, and B. Douçot, *Quantum wire networks with local $\mathbb{Z}_2$ symmetry*, Phys. Rev. B **72**, 235114 (2005).

[22] J.L. Movilla and J. Planelles, *Quantum level engineering for Aharonov-Bohm caging in the presence of electron-electron interactions*, Phys. Rev. B **84**, 195110 (2011).

[23] A.A. Lopes and R.G. Dias, *Interacting spinless fermions in a diamond chain*, Phys. Rev. B **84**, 085124 (2011).

[24] A.A. Lopes, B.A.Z. António, and R.G. Dias, *Conductance through geometrically frustrated itinerant electronic systems*, Phys. Rev. B **89**, 235418 (2014).

[25] S. Takayoshi, H. Katsura, N. Watanabe, and H. Aoki, *Phase diagram and pair Tomonaga-Luttinger liquid in a Bose-Hubbard model with flat bands*, Phys. Rev. A **88**, 063613 (2013).

[26] M. Tovmasyan, E.P.L. van Nieuwenburg, and S.D. Huber, *Geometry-induced pair condensation*, Phys. Rev. B **88**, 220510 (2013).

[27] F. Lin, C. Zhang, and V.W. Scarola, *Emergent Kinetics and Fractionalized Charge in 1D Spin-Orbit Coupled Flatband Optical Lattices*, Phys. Rev. Lett. **112**, 110404 (2014).

[28] J.R. Williams, L. DiCarlo, and C.M. Marcus, *Quantum Hall effect in a gate-controlled p-n junction of graphene*, Science **317**, 638 (2007).

[29] B. Huard, J.A. Sulpizio, N. Stander, K. Todd, B. Yang, and D. Goldhaber-Gordon, *Transport Measurements Across a Tunable Potential Barrier in Graphene*, Phys. Rev. Lett. **98**, 236803 (2007).

[30] B. Özyilmaz, P. Jarillo-Herrero, D. Efetov, D.A. Abanin, L.S. Levitov, and P. Kim, *Electronic Transport and Quantum Hall Effect in Bipolar Graphene p-n-p Junctions*, Phys. Rev. Lett. **99**, 166804 (2007).

[31] A.F. Young and P. Kim, *Quantum interference and Klein tunnelling in graphene heterojunctions*, Nature Phys. **5**, 222 (2009).

[32] J.R. Williams, T. Low, M.S. Lundstom, and C.M. Marcus, *Gate-controlled guiding of electrons in graphene*, Nature Nanotech. **6**, 222 (2011).

[33] H. Schmidt, J.C. Rode, C. Belke, D. Smirnov, and R.J. Haug, *Mixing of edge states at a bipolar graphene junction*, Phys. Rev. B **88**, 075418 (2013).

[34] F. Amet, J.R. Williams, K. Watanabe, T. Taniguchi, and D. Goldhaber-Gordon, *Selective equilibration of spin-polarized quantum Hall edge states in graphene*, Phys. Rev. Lett. **112**, 196601 (2014).

[35] N.N. Klimov, S.T. Le, J. Yan, P. Agnihotri, E. Comfort, J.U. Lee, D.B. Newell, and C.A. Richter, *Edge-state transport in graphene p-n junctions in the quantum Hall regime*, Phys. Rev. B **92**, 241301(R) (2015).

[36] P. Rickhaus, M.H. Liu, P. Makk, R. Maurand, S. Hess, S. Zihlmann, M. Weiss, K. Richter, and C. Schönenberger, *Guiding of Electrons in a Few-Mode Ballistic Graphene Channel*, Nano Lett. **15**, 5819 (2015).

[37] Y. Zhao, J. Wyrick, F.D. Natterer, J.F. Rodriguez-Nieva, C. Lewandowski, K. Watanabe, T. Taniguchi, L.S. Levitov, N.B. Zhitenev, and J.A. Stroscio, *Creating and probing electron whispering-gallery modes in graphene*, Science **348**, 672 (2015).

[38] S. Matsuo, S. Takeshita, T. Tanaka, S. Nakaharai, K. Tsukagoshi, T. Moriyama, T. Ono, and K. Kobayashi, *Edge mixing dynamics in graphene p–n junctions in the quantum Hall regime*, Nature Comm. **6**, 8066 (2015).

[39] N. Kumada, F.D. Parmentier, H. Hibino, D.C. Glattli, and P. Roulleau, *Shot noise generated by graphene p–n junctions in the quantum Hall effect regime*, Nature Comm. **6**, 8068 (2015).

[40] E. Tóvari, P. Makk, P. Rickhaus, C. Schönenberger, and S. Csonka, *Signatures of single quantum dots in graphene nanoribbons within the quantum Hall regime*, Nanoscale **8**, 11480 (2016).

[41] S. Chen, Z. Han, M.M. Elahi, K.M.M. Habib, L. Wang, B. Wen, Y. Gao, T. Taniguchi, K. Watanabe, J. Hone, A.W. Ghosh, and C.R. Dean, *Electron optics with p-n junctions in ballistic graphene*, Science **353** (6307), 1522 (2016)

[42] J. Lee, D. Wong, J. Velasco Jr., J.F. Rodriguez-Nieva, S. Kahn, H.-Z. Tsai, T. Taniguchi, K. Watanabe, A. Zettl, F. Wang, L.S. Levitov, and M.F. Crommie, *Imaging electrostatically confined Dirac fermions in graphene quantum dots*, Nat. Phys. **12**, 1032 (2016).

[43] J.R. Williams and C.M. Marcus, *Snake States along Graphene Junctions*, Phys. Rev. Lett. **107**, 046602 (2011).

[44] T. Taychatanapat, J.Y. Tan, Y. Yeo, K. Watanabe, T. Taniguchi, and B. Özyilmaz, *Conductance oscillations induced by ballistic snake states in a graphene heterojunction*, Nature Comm. **6**, 6093 (2015).

[45] P. Rickhaus, P. Makk, M.H. Liu, E. Tóvári, M. Weiss, R. Maurand, K. Richter, and C. Schönenberger, *Snake trajectories in ultraclean graphene p-n junctions*, Nature Comm. **6**, 6470 (2015).

[46] E. Tóvari, P. Makk, M.H. Liu, P. Rickhaus, Z. Kovács-Krausz, K. Richter, C. Schönenberger, and S. Csonka, *Gate-controlled conductance enhancement from quantum Hall channels along graphene p–n junctions*, Nanoscale **8**, 19910 (2016).

[47] V.E. Calado, S. Goswami, G. Nanda, M. Diez, A.R. Akhmerov, K. Watanabe, T. Taniguchi, T.M. Klapwijk, and L.M.K. Vandersnypen, *Ballistic Josephson junctions in edge-contacted graphene*, Nat. Nanotech. **10**, 761 (2015).

[48] G.H. Lee, S. Kim, S.H. Jhi, and H.J. Lee, *Ultimately short ballistic vertical graphene Josephson junctions*, Nat. Commun. **6**, 6181 (2015).

[49] M.T. Allen, O. Shtanko, I.C. Fulga, A.R. Akhmerov, K. Watanabe, T. Taniguchi, P. Jarillo-Herrero, L.S. Levitov, and A. Yacoby, *Spatially resolved edge currents and guided-wave electronic states in graphene*, Nature Phys. **12**, 128 (2016).

[50] D.K. Efetov, L. Wang, C. Handschin, K.B. Efetov, J. Shuang, R. Cava, T. Taniguchi, K. Watanabe, J. Hone, C.R. Dean, and P. Kim, *Specular interband Andreev reflections at van der Waals interfaces between graphene and NbSe_2*, Nat. Phys. **12**, 328 (2016).

[51] I.V. Borzenets, F. Amet, C.T. Ke, A.W. Draelos, M.T. Wei, A. Seredinski, K. Watanabe, T. Taniguchi, Y. Bomze, M. Yamamoto, S. Tarucha, and G. Finkelstein, *Ballistic Graphene Josephson Junctions from the Short to the Long Junction Regimes*, Phys. Rev. Lett. **117**, 237002 (2016).

[52] M. Ben Shalom, M.J. Zhu, V.I. Fal'ko, A. Mishchenko, A.V. Kretinin, K.S. Novoselov, C.R. Woods, K. Watanabe, T. Taniguchi, A.K. Geim, and J.R. Prance, *Quantum oscillations of the critical current and high-field superconducting proximity in ballistic graphene*, Nat. Phys. **12**, 318 (2016).

[53] F. Amet, C.T. Ke, I.V. Borzenets, J. Wang, K. Watanabe, T. Taniguchi, R.S. Deacon, M. Yamamoto, Y. Bomze, S. Tarucha, and G. Finkelstein, *Supercurrent in the quantum Hall regime*, Science **352**, 966 (2016).

[54] G.H. Lee, K.F. Huang, D.K. Efetov, D.S. Wei, S. Hart, T. Taniguchi, K. Watanabe, A. Yacoby, and P. Kim, *Inducing superconducting correlation in quantum Hall edge states*, Nat. Phys. **13**, 693 (2017).

[55] M.J. Zhu, A.V. Kretinin, M.D. Thomas, D.A. Bandurin, S. Hu, G.L. Yu, J. Birkbeck, A. Mishchenko, I.J. Vera-Marun, K. Watanabe, T. Taniguchi, M. Polini, J.R. Prance, K.S. Novoselov, A.K. Geim, and M. Ben Shalom, *Edge currents shunt the insulating bulk in gapped graphene*, Nat. Commun. **8**, 14552 (2017).

[56] G. Nanda, J.L. Aguilera-Servin, P. Rakyta, A. Kormányos, R. Kleiner, D. Koelle, K. Watanabe, T. Taniguchi, L.M.K. Vandersypen, and S. Goswami, *Current-Phase Relation of Ballistic Graphene Josephson Junctions*, Nano Lett. **17**, 3396 (2017).

[57] L. Bretheau, J.I. Wang, R. Pisoni, K. Watanabe, T. Taniguchi, and P. Jarillo-Herrero, *Tunnelling spectroscopy of Andreev states in graphene*, Nat. Phys. **13**, 756 (2017).

[58] P. R. Wallace, *The Band Theory of Graphite* Phys. Rev. 71, 622 (1947)

[59] N. Stander, B. Huard, and D. Goldhaber-Gordon, *Evidence for Klein Tunneling in Graphene p-n Junctions*, Phys. Rev. Lett. **102**, 026807 (2009)

[60] C.W.J. Beenakker, A.R. Akhmerov, P. Recher, and J.Tworzydlo, *Correspondence between Andreev reflection and Klein tunneling in bipolar graphene*, Phys. Rev. B **77**, 075409 (2008)

[61] H. Bruus, K. Flensberg, *Many-Body Quantum Theory in Condensed Matter Physics - An Introduction*, Oxford University Press (2004).

[62] R. Egger, lecture notes *Theoretische Festkörperphysik*, Heinrich-Heine-Universität Düsseldorf, summer term 2013.

[63] T.K. Ghosh, A. De Martino, W. Häusler, L. Dell'Anna, and R. Egger, *Conductance quantization and snake states in graphene magnetic waveguides*, Phys. Rev. B **77**, 081404(R) (2008).

[64] D.A. Abanin and L.S. Levitov, *Quantized Transport in Graphene p-n Junctions in a Magnetic Field*, Science **317**, 641 (2007).

[65] C. Fräßdorf, L. Trifunovic, N. Bogdanoff, and P.W. Brouwer, *Graphene pn junction in a quantizing magnetic field: Conductance at intermediate disorder strength*, Phys. Rev. B **94**, 195439 (2016).

[66] L.D. Landau, *The Theory of a Fermi Liquid*, Sov. Phys. JETP **3**, 920 (1957).

[67] L.D. Landau *Oscillations in a Fermi Liquid* Sov. Phys. JETP **5**, 101 (1957).

[68] H.J. Schulz, G.Cuniberti and P. Pieri, *Fermi Liquids and Luttinger Liquids* in *Field Theories for Low-Dimensional Condensed Matter Systems*, Eds. Springer (2000), ISBN: 3540671773.

[69] J. Voit, *One-dimensional Fermi liquids*, Rep. Prog. Phys **58**, 977 (1995).

[70] R.G. Sharma, *A Review of Theories of Superconductivity; Superconductivity: Basics and Applications to Magnets*, Springer International Publishing (2015), ISBN 978-3-319-13713-1.

[71] W. Meissner, R. Ochsenfeld, *Ein neuer Effekt bei Eintritt der Supraleitfähigkeit*, Die Naturwissenschaften **21**, 44, 787 (1933)

[72] E. Pavarini, E. Koch, and U. Schollwöck,*Emergent Phenomena in Correlated Matter, Modeling and Simulation Vol. 3*, Forschungszentrum Jülich (2013), ISBN 978-3-89336-884-6, http://www.cond-mat.de/events/correl13

[73] Y. Nambu, *Quasi-Particles and Gauge Invariance in the Theory of Superconductivity*, Phys. Rev. **117**, 648 (1960)

[74] F. von Oppen, Y. Peng, F. Pientka, *Topological Aspects of Condensed Matter Physics: Topological superconducting phases in one dimension*, Oxford University Press (2014), ISBN-13: 9780198785781

[75] T. Kato, *Perturbation Theory for Linear Operators*, Springer (1995), ISBN 978-3-642-66282-9

[76] A.P. Jauho, *Introduction to the keldysh nonequilibrium green function technique*, Lect. notes 17 (2006).

[77] L. Cohnitz, W. Häusler, A. Zazunov and R. Egger, *Interaction-induced conductance from zero modes in a clean magnetic graphene waveguide*, Phys. Rev. B **92**, 085422 (2015).

[78] V.P. Gusynin and S.G. Sharapov, *Unconventional Integer Quantum Hall Effect in Graphene*, Phys. Rev. Lett. **95**, 146801 (2005).

[79] V.P. Gusynin and S.G. Sharapov, *Transport of Dirac quasiparticles in graphene: Hall and optical conductivities*, Phys. Rev. B **73**, 245411 (2006).

[80] A. De Martino, L. Dell'Anna, and R. Egger, *Magnetic Confinement of Massless Dirac Fermions in Graphene*, Phys. Rev. Lett. **98**, 066802 (2007).

[81] A. De Martino, L. Dell'Anna, and R. Egger, *Magnetic barriers and confinement of Dirac-Weyl quasiparticles in graphene*, Solid State Comm. **144**, 547 (2007).

[82] S. Ghosh and M. Sharma, *Electron optics with magnetic vector potential barriers in graphene*, J. Phys. Cond. Matt. **21**, 292204 (2009).

[83] S. Kuru, J. Negro, and L.M. Nieto, *Exact analytic solutions for a Dirac electron moving in graphene under magnetic fields*, J. Phys. Cond. Matt. **21**, 455305 (2009).

[84] T.K. Ghosh, *Exact solutions for a Dirac electron in an exponentially decaying magnetic field*, J. Phys.: Cond. Matt. **21**, 045505 (2009).

[85] P. Roy, T.K. Ghosh, and K. Bhattacharya, *Localization of Dirac-like excitations in graphene in the presence of smooth inhomogeneous magnetic fields*, J. Phys.: Cond. Matt. **24**, 055301 (2012).

[86] M.R. Masir, P. Vasilopoulos, A. Matulis, and F. Peeters, *Direction-dependent tunneling through nanostructured magnetic barriers in graphene*, Phys. Rev. B **77**, 235443 (2008).

[87] A. Zazunov, A. Kundu, A. Hütten, and R. Egger, *Magnetic scattering of Dirac fermions in topological insulators and graphene*, Phys. Rev. B **82**, 155431 (2010).

[88] L. Oroszlany, P. Rakyta, A. Kormanyos, C.J. Lambert, and J. Cserti, *Theory of snake states in graphene*, Phys. Rev. B **77**, 081403(R) (2008).

[89] W. Häusler, A. De Martino, T.K. Ghosh, and R. Egger, *Tomonaga-Luttinger liquid parameters of magnetic waveguides in graphene*, Phys. Rev. B **78**, 165402 (2008).

[90] Y.P. Bliokh, V. Freilikher, and F. Nori, *Tunable electronic transport and unidirectional quantum wires in graphene subjected to electric and magnetic fields*, Phys. Rev. B **81**, 075410 (2010).

[91] E. Prada, P. San-Jose, and L. Brey, *Zero Landau Level in Folded Graphene Nanoribbons*, Phys. Rev. Lett. **105**, 106802 (2010).

[92] S. Park and H.-S. Sim, *Magnetic edge states in graphene in nonuniform magnetic fields*, Phys. Rev. B **77**, 075433 (2008).

[93] A. De Martino, A. Hütten, and R. Egger, *Landau levels, edge states, and strained magnetic waveguides in graphene monolayers with enhanced spin-orbit interaction*, Phys. Rev. B **84**, 155420 (2011).

[94] Kh. Shakouri, S.M. Badalyan, and F.M. Peeters, *Helical liquid of snake states*, Phys. Rev. B **88**, 195404 (2013).

[95] M.A.H. Vozmediano, M.I. Katsnelson, and F. Guinea, *Gauge fields in graphene*, Phys. Rep. **496**, 109 (2010).

[96] Y. Chang, T. Albash, and S. Haas, *Quantum Hall states in graphene from strain-induced nonuniform magnetic fields*, Phys. Rev. B **86**, 125402 (2012).

[97] M.Z. Hasan and C.L. Kane, *Topological Insulators*, Rev. Mod. Phys. **82**, 3045 (2010).

[98] M. Sitte, A. Rosch, and L. Fritz, *Interaction effects in almost flat surface bands in topological insulators*, Phys. Rev. B **88**, 205107 (2013).

[99] V.N. Kotov, B. Uchoa, V.M. Pereira, A.H. Castro Neto, and F. Guinea, *Electron-Electron Interactions in Graphene: Current Status and Perspectives*, Rev. Mod. Phys. **84**, 1067 (2012).

[100] L. Cohnitz, *Flat bands in graphene nanostructures*, Masterarbeit, Heinrich-Heine-Universität Düsseldorf (2014).

[101] I.S. Gradshteyn and I.M. Ryzhik, *Table of Integrals, Series, and Products* (Academic Press, Elsevier, 2007).

[102] M. Abramowitz and I.A. Stegun (eds.), *Handbook of Mathematical Functions* (Dover, New York, 1965). F.W.J. Oliver, D. W. Lozier, R. F. Boisvert, and C.W. Clark, editors, *NIST Handbook of Mathematical Functions*, (Cambridge University Press, New York, NY, 2010).

[103] G. Lehmann, *Numerical Simulations I*, lecture script, Heinrich-Heine-Universität Düsseldorf (2012)

[104] G.F. Giuliani and G. Vignale, *Quantum Theory of the Electron Liquid* (Cambridge University Press, Cambridge UK, 2008).

[105] K. Nomura and A.H. MacDonald, *Quantum Hall ferromagnetism in graphene*, Phys. Rev. Lett. **96**, 256602 (2006).

[106] M.O. Goerbig, R. Moessner, and B. Douçot, *Electron interactions in graphene in a strong magnetic field*, Phys. Rev. B **74**, 161407(R) (2006).

[107] C.H. Zhang and Y.N. Joglekar, *Wigner crystal and bubble phases in graphene in the quantum Hall regime*, Phys. Rev. B **75**, 245414 (2007).

[108] R. Côté, J.F. Jobidon, and H.A. Fertig, *Skyrme and Wigner crystals in graphene*, Phys. Rev. B **78**, 085309 (2008).

[109] O. Poplavskyy, M.O. Goerbig, and C. Morais Smith, *Local density of states of electron-crystal phases in graphene in the quantum Hall regime*, Phys. Rev. B **80**, 195414 (2009).

[110] C. Faugeras *et al.*, *Landau Level Spectroscopy of Electron-Electron Interactions in Graphene*, Phys. Rev. Lett. **114**, 126804 (2015).

[111] A. Altland and B.D. Simons, *Condensed Matter Field Theory*, 2nd edition (Cambridge University Press, Cambridge, England, 2010).

[112] B.L. Altshuler and A.G. Aronov, *Zero-bias anomaly in tunnel resistance and electron-electron interaction*, Solid State Comm. **30**, 115 (1979).

[113] G. Zala, B.N. Narozhny, and I.L. Aleiner, *Interaction corrections at intermediate temperatures: Longitudinal conductivity and kinetic equation*, Phys. Rev. B **64**, 214204 (2001).

[114] P.W. Brouwer and J.N. Kupferschmidt, *Interaction Correction to the Conductance of a Ballistic Conductor*, Phys. Rev. Lett. **100**, 246805 (2008).

[115] S.C. Kim, S.-E. Yang, and A. MacDonald, *Impurity cyclotron resonance of anomalous Dirac electrons in graphene*, J. Phys.: Cond. Matt. **26**, 325302 (2014).

[116] F.D.M. Haldane, *Luttinger Liquid Theory of One-dimensional Quantum Fluids .1. Properties of the Luttinger Model and their Extension to the General 1D Interacting Spinless Fermi Gas*, J. Phys. C **14**, 2585 (1981).

[117] T. Giamarchi, *Quantum Physics in One Dimension* (Oxford University Press, 2004).

[118] W. Apel and T.M. Rice, *Combined effect of disorder and interactions on the conductance of a one-dimensional fermion system*, Phys. Rev. B **26**, 7063(R) (1982).

[119] W. Häusler, L. Kecke, and A.H. MacDonald, *Tomonaga-Luttinger parameters for quantum wires*, Phys. Rev. B **65**, 085104 (2002).

[120] A.O. Gogolin, A.A. Nersesyan, and A.M. Tsvelik, *Bosonization and Strongly Correlated Systems* (Cambridge University Press, Cambridge, UK, 1998).

[121] H.-W. Lee and D.S. Novikov, *Supersymmetry in carbon nanotubes in a transverse magnetic field*, Phys. Rev. B **68**, 155402 (2003).

[122] C.H. Liu, P.H. Wang, T.P. Woo, F.Y. Shih, S.C. Liou, P.H. Ho, C.W. Chen, C.T. Liang, W.H. Wang, *Observation of quantum Hall plateau-plateau transition and scaling behavior of the zeroth Landau level in graphene p-n-p junctions*, Phys. Rev. B **93**, 041421(R) (2016).

[123] P. Carmier, C. Lewenkopf, and D. Ullmo, *Graphene n-p junction in a strong magnetic field: A semiclassical study*, Phys. Rev. B **81**, 241406(R) (2010).

[124] P. Carmier, C. Lewenkopf, and D. Ullmo, *Semiclassical magnetotransport in graphene n-p junctions*, Phys. Rev. B **84**, 195428 (2011).

[125] A.A. Patel, N. Davies, V. Cheianov, and V.I. Fal'ko, *Classical and quantum magneto-oscillations of current flow near a p-n junction in graphene*, Phys. Rev. B **86**, 081413 (2012).

[126] M. Zarenia, J.M. Pereira, Jr., F. M. Peeters, and G.A. Farias, *Snake states in graphene quantum dots in the presence of a p-n junction*, Phys. Rev. B **87**, 035426 (2013).

[127] A. Mrenca-Kolasinska, S. Heun, and B. Szafran, *Aharonov-Bohm interferometer based on n-p junctions in graphene nanoribbons*, Phys. Rev. B **93**, 125411 (2016).

[128] J. Wang, X. Chen, B.F. Zhu, and S.C. Zhang, Phys. Rev. B **85**, 235131 (2012).

[129] Y. Liu, R.P. Tiwari, M. Brada, C. Bruder, F.V. Kusmartsev, and E.J. Mele, *Snake states and their symmetries in graphene*, Phys. Rev. B **92**, 235438 (2015).

[130] R. Ilan, F. de Juan, and J.E. Moore, *Spin-Based Mach-Zehnder Interferometry in Topological Insulator p-n Junctions*, Phys. Rev. Lett. **115**, 096802 (2015).

[131] S. Acero, L. Brey, W.J. Herrera, and A.L. Yeyati, *Transport in selectively magnetically doped topological insulator wires*, Phys. Rev. B **92**, 235445 (2015).

[132] Laura Cohnitz, Alessandro De Martino, Wolfgang Häusler, and Reinhold Egger, *Chiral interface states in graphene p-n junctions*, Phys. Rev. B **94**, 165443 (2016).

[133] I. Bartoš and B. Rosenstein, *Edge states in a strong magnetic field*, J. Phys. A: Math. Gen. **27**, L53 (1994).

[134] A. De Martino and R. Egger, *On the spectrum of a magnetic quantum dot in graphene*, Semicond. Sci. Technol. **25**, 034006 (2010).

[135] F. Hund, *Rechnungen über das magnetische Verhalten von kleinen Metallstücken bei tiefen Temperaturen*, Ann. Phys. **32**, 102 (1938)

[136] N. Byers and C.N. Yang, *Theoretical Considerations Concerning Quantized Magnetic Flux in Superconducting Cylinders*, Phys. Rev. Lett. **46**, 7 (1961).

[137] F. Bloch, *Off-Diagonal Long-Range Order and Persistent Currents in a Hollow Cylinder*, Phys. Rev. **137**, A787 (1965).

[138] H.F. Cheung, Y. Gefen, E.K. Riedel, and W.H. Shih, *Persistent currents in small one-dimensional metal rings*, Phys. Rev. B **37**, 6050 (1988).

[139] D. Mailly, C. Chapelier, and A. Benoit, *Experimental observation of persistent currents in GaAs-AlGaAs single loop*, Phys. Rev. Lett. **70**, 2020 (1993).

[140] J. Kirtley *et al.*, *Scanning SQUID susceptometers with sub-micron spatial resolution*, Rev. Scient. Inst. 87, 093702 (2016)

[141] F. Nichele, A.C.C. Drachmann, A.M. Whiticar, E. C.T. O'Farrell, H.J. Suominen, A. Fornieri, T. Wang, G.C. Gardner, C. Thomas, A.T. Hatke, P. Krogstrup, M.J. Manfra, K. Flensberg, and C.M. Marcus, *Scaling of Majorana Zero-Bias Conductance Peaks*, preprint arXiv:1706.07033.

[142] B. Uchoa and A.H. Castro Neto, *Superconducting States of Pure and Doped Graphene*, Phys. Rev. Lett. **98**, 146801 (2007).

[143] N.B. Kopnin and E.B. Sonin, *BCS Superconductivity of Dirac Electrons in Graphene Layers*, Phys. Rev. Lett. **100**, 246808 (2008).

[144] L. Cohnitz, A. De Martino, W. Häusler, R. Egger, *Proximity-induced superconductivity in Landau-quantized graphene monolayers*, arXiv:1708.02892 (2017)

[145] C.W.J. Beenakker, *Specular Andreev Reflection in Graphene*, Phys. Rev. Lett. **97**, 067007 (2006).

[146] M. Titov and C.W.J. Beenakker, *Josephson effect in ballistic graphene*, Phys. Rev. B **74**, 041401(R) (2006).

[147] A. Ossipov, M. Titov, and C.W.J. Beenakker, *Reentrance effect in a graphene n-p-n junction coupled to a superconductor*, Phys. Rev. B **75**, 241401(R) (2007).

[148] C. Schönenberger, private communication.

[149] M. Rasolt and Z. Tesanovic, *Theoretical aspects of superconductivity in very high magnetic fields*, Rev. Mod. Phys. **64**, 709 (1992).

[150] A.H. MacDonald, H. Akera, and M.R. Norman, *Quantum Mechanics and Superconductivity in a Magnetic Field*, Aust. J. Phys. **46**, 333 (1993).

[151] B. Uchoa and Y. Barlas, *Superconducting States in Pseudo-Landau-Levels of Strained Graphene*, Phys. Rev. Lett. **111**, 046604 (2013).

[152] S.P. Lee, D. Nandi, F. Marsiglio, and J. Maciejko, *Fractional Josephson effect in nonuniformly strained graphene*, Phys. Rev. B **95**, 174517 (2017).

[153] L. Brey and H.A. Fertig, *Edge states and the quantized Hall effect in graphene*, Phys. Rev. B **73**, 195408 (2006).

[154] D.A. Abanin, P.A. Lee, and L.S. Levitov, *Charge and spin transport at the quantum Hall edge of graphene*, Solid State Commun. **143**, 77 (2007).

[155] P. Delplace and G. Montambaux, *WKB analysis of edge states in graphene in a strong magnetic field*, Phys. Rev. B **82**, 205412 (2010).

[156] V. Lukose, R. Shankar, and G. Baskaran, *Novel Electric Field Effects on Landau Levels in Graphene*, Phys. Rev. Lett. **98**, 116802 (2007).

Acknowledgements

The first person I would like to thank is my supervisor Prof. Dr. Reinhold Egger, who has always been reachable for answering questions within minutes via emails from most diverse places all over the world, as well as precious council, help and of course for giving me the chance to do my PhD with him. Secondly, I appreciate deeply Prof. Dr. Dr. Müller's consent to become the second referent for my thesis. Also, I wish to thankfully mention PD Dr. Hermann Kampermann who already was a mentor to me before officially being assigned to that task - I will miss our little talks in the morning, before most of the other people show up.

Furthermore, my deep gratitude goes to all of my co-workers PD Dr. Wolfgang Häusler, Dr. Alex Zazunov for working with me on our projects, not to mention blue editions, hand-written notes without page 13, and especially Senior Lecturer Dr. Alessandro De Martino for multilingual exchange and brooding together over calculations on various blackboards, as well as always being supportive and quick to extend a helping hand. Moreover, there are a lot of people in this university some of whom belong(ed) to our institute and some who didn't, who contributed a lot to render the days in my office enjoyable and to whom I will always be obliged. Not only inside the walls of this institution but also in the „other life", there are plenty of friends whose amity I appreciate and whose presence in my life I wouldn't want to miss - thank you for standing with me. Thanks goes also to my parents, for telling me, I could be anything and being proud of me for both the big and the tiniest things for as long as I can remember. And last but very definitely not least, a thousand thanks and love to Bastian Hagmeister for always having my back, standing by me, and making me laugh even when I'm about to cry - I wouldn't have been able to do this without YOU!

135

Selbstständigkeitserklärung

Ich versichere an Eides Statt, dass die Dissertation von mir selbständig und ohne unzulässige fremde Hilfe unter Beachtung der „Grundsätze zur Sicherung guter wissenschaftlicher Praxis an der Heinrich-Heine-Universität Düsseldorf" erstellt worden ist.

Ich habe keine anderen als die im Literaturverzeichnis angegebenen Quellen genutzt; wörtliche oder sinngemäße Inhalte anderer Werke oder Quellen sind als solche kenntlich gemacht.

Weiterhin erkläre ich, dass die vorliegende Arbeit zuvor weder von mir, noch - soweit mir bekannt - von anderen Personen an dieser oder an einer anderen Hochschule eingereicht wurde und ich bisher weder erfolglose noch erfolgreiche Promotionsversuche unternommen habe.

Darüber hinaus ist mir bekannt, dass jedweder Betrugsversuch zum Nichtbestehen oder zur Aberkennung der Prüfungsleistung führen kann.

Düsseldorf, September 4, 2017 _____